1-1-2001

2MASS view of the LMC : structure, populations, kinematics.

Sergei, Nikolaev
University of Massachusetts Amherst

2MASS VIEW OF THE LMC: STRUCTURE, POPULATIONS, KINEMATICS

A Dissertation Presented

by

SERGEI NIKOLAEV

Submitted to the Graduate School of the
University of Massachusetts Amherst in partial fulfillment
of the requirements for the degree of

DOCTOR OF PHILOSOPHY

May 2001

Department of Astronomy

2MASS VIEW OF THE LMC:
STRUCTURE, POPULATIONS, KINEMATICS

A Dissertation Presented

by

SERGEI NIKOLAEV

Approved as to style and content by:

Martin D. Weinberg, Chair

Michael F. Skrutskie, Member

Stephen E. Schneider, Member

John P. Buonaccorsi, Member

Ronald L. Snell, Department Head
Department of Astronomy

To my parents

ACKNOWLEDGEMENTS

My deepest debt of gratitude goes to my advisor, Prof. Martin Weinberg, who has always supported me, both morally and financially, during the seven years that I spent here. He has allowed me enough freedom to do things that I liked and to study things that I wanted, yet he has always been there to discuss my progress and, if necessary, point me in the right direction. He has always encouraged me to do a little more and pushed me a little harder in order to become a better student. Even though sometimes it felt like I was Cmdr. LaForge needing to find the problem in the bypass circuits of the warp field coils in a very limited amount of time, it still was a great experience that taught me what it means to be a scientist.

I would also like to thank my dissertation committee members, Profs. Steve Schneider, Mike Skrutskie, and John Buonaccorsi, for their constant support during my tenure as a graduate student and for numerous suggestions that helped to shape this document. I am grateful to all faculty members of the Astronomy Department, and especially to Bill Irwine and David van Blerkom, who helped to arrange my visit to the US seven years ago, and to Shashi Kanbur for his friendship and continuous interest in my work.

It is a pleasure to thank the secretarial staff of our department, and especially Denise Sallee and Terri Grzybowski, for their helpful assistance and attention to the needs of graduate students.

I want to thank my fellow graduate students and postdocs, who made these seven years a pleasant journey: Russ Makidon, Jessica Rosenberg, John Gizis and many others. I am grateful to my russian fellow students, Alexei Petrov and Alexei Koloydenko, with whom we shared many great discussions and had a lot of fun outside

the Lederle tower. And, of course, my thanks goes to all members of russian-latvian "gang", for their friendship and support. And, Sasha, yes, there *was* a Big Bang.

This publication makes use of data products from the Two Micron All Sky Survey, which is a joint project of the University of Massachusetts and the Infrared Processing and Analysis Center, funded by the National Aeronautics and Space Administration and the National Science Foundation.

ABSTRACT

2MASS VIEW OF THE LMC:
STRUCTURE, POPULATIONS, KINEMATICS

MAY 2001

SERGEI NIKOLAEV, B.S., ST. PETERSBURG UNIVERSITY

Ph.D., UNIVERSITY OF MASSACHUSETTS AMHERST

Directed by: Professor Martin D. Weinberg

The results of a study of the Large Magellanic Cloud based on near-infrared 2MASS photometry are presented. From near-infrared color-magnitude diagram, stellar populations of the LMC are identified and characterized, and their spatial distributions are studied. The luminosity functions are presented for LMC bar and disk fields. Isochrone analysis is performed and estimates of age and metallicity of bar and disk populations are obtained. Geometrical structure of the LMC is studied and its distance modulus is estimated from AGB tip magnitude. Inferences about the spatial structure of the LMC are obtained by standard candle analysis based on carbon-rich long-period variables. The evidence is presented for material out of plane of the main LMC disk. Based on a maximum-likelihood analysis of 2MASS photometry and stellar kinematics available in the literature, the conclusion is derived that a secondary stellar component is present at roughly ~ 5 kpc behind the main LMC disk. This material has lower systemic velocity than the disk of the LMC and is shown to be able to enhance the microlensing optical depth and bring it to agreement with MACHO observations.

TABLE OF CONTENTS

APPENDICES

LIST OF TABLES

LIST OF FIGURES

CHAPTER 1

INTRODUCTION AND OUTLINE

Large and homogeneous data sets of near-infrared photometry for the entire LMC, a by-product of large-scale infrared sky surveys such as 2MASS (Skrutskie et al. 1997) and DENIS (Epchtein et al. 1997), have become available to astronomical community only recently. Here, we present the results of the study of the Large Magellanic Cloud (LMC) based on 2MASS data.

1.1 Motivation and Research Goals

Our closest galactic neighbor, the Large Magellanic Cloud, provides an opportunity to study stellar populations and star formation in an environment other than our own Galaxy. Because of its proximity, approximately 50 kpc, and high galactic latitude the LMC is a reasonably well-studied object. Previous work on the morphology of the LMC based on wide-angle photographs characterized LMC as an ellipse approximately $16^\circ \times 14^\circ$ in size ($1^\circ = 0.87$ kpc; de Vaucouleurs & Freeman 1973), with the position angle of its semimajor axis $\Theta \sim 130^\circ - 180^\circ$ (see, e.g. Schmidt-Kaler & Gochermann 1992 and references therein). Recently, Irwin (1991) estimated a size of $23^\circ \times 17^\circ$ from star counts, and Nikolaev & Weinberg (1998) have estimated the LMC tidal radius (~ 11 kpc) based on USNO-A starcounts and on 2MASS prototype starcounts. The estimates of the inclination of the Cloud to the line of sight range from 25° to 45° (Schmidt-Kaler & Gochermann 1992). The direction of the tilt of the LMC can be determined by considering magnitudes of Cepheids on the opposite sides of the galaxy: results indicate that NE part of the LMC is nearer the Sun (de Vau-

couleurs 1955, Gascoigne & Shobbrook 1978, Laney & Stobie 1986). However, from reviewing distance moduli of 170 supergiants of the LMC Isserstedt (1975) derived that the closest to the Sun is the Western part of the galaxy. The central region of the LMC is occupied by a bar, $3.5° \times 1°$ in size, with position angle of its major axis at 120°. The spiral structure of the LMC is described, e.g., by de Vaucouleurs & Freeman (1973) or Schmidt-Kaler (1977).

Despite the apparently complex morphology of the LMC, the kinematical studies of populations such as H I gas, H II regions, supergiants and planetary nebulae (reviewed in de Vaucouleurs & Freeman 1973, Feitzinger 1980) indicate that the kinematics of the Cloud is rather simple and is dominated by a disk. Later studies of kinematics of H I, CO clouds, CH stars, clusters and long-period variables (LPV), carried out by Hughes et al. (1991) and of planetary nebulae (Meatheringham et al. 1988) also imply that LMC dynamics are dominated by a single rotating disk potential. Even though recent analysis of old LPVs of the LMC (Hughes et al. 1991) gave first indications to the existence of a spheroid population, these results must be taken cautiously (Olszewski et al. 1996).

Despite the progress in our understanding of the LMC, many problems still remain. Some of the most important issues still waiting to be resolved are the following:

- What is the three-dimensional structure of the LMC?
- What are the age and metallicity distributions of LMC populations?
- What is the history of star formation in the Magellanic Clouds and when did the major episodes of star formation in the LMC take place?
- Is there a halo component and does it contribute significantly to microlensing statistics?
- What is the dust distribution within the LMC?

A number of research projects are currently addressing these issues. For example, a digital photometric survey of the LMC in UBVI (Zaritsky et al. 1997) has already produced a detailed map of the internal extinction of the LMC. The data indicate patchy dust distribution in the Cloud (Harris et al. 1997). MACHO group is monitoring several million LMC stars (Alcock et al. 1997); the data can be used to effectively select and study variable stars in the LMC (e.g., Cepheids, AGBs, etc). Such a database could be quite useful in establishing the three-dimensional structure of the LMC, because most variable stars obey a Period–Luminosity relation, which provides an estimate of the distance. While improving our understanding, these optical studies are hampered by interstellar dust (both foreground and internal to the LMC). The dust extinction limits our ability to resolve the structure of the Cloud along the line of sight due to severe undersampling problems. To make things even worse, modeling of dust distribution inside the Cloud is difficult due to its clumpiness (Harris et al. 1997). On the other hand, a large-scale near-infrared (NIR) survey, such as 2MASS, is relatively unaffected by dust extinction, since the extinction in K band is an order of magnitude less than in the optical. Specifically, using 2MASS high-quality NIR data to study the large scale structure of the LMC has the following advantages:

- *Globality.* 2MASS provides a truly global view of the LMC, as opposed to most previous studies which concentrated on relatively small regions in the Cloud;

- *Homogeneity.* Because of the complete coverage by 2MASS, we have in our possession a large homogeneous data set ($\sim 10^7$ sources), which can be used to study the LMC in its entirety;

- *Near-infrared survey.* 2MASS provides a view of the LMC in *near-infrared* (J, H, and K) bands, which results in very low galactic foreground extinction and offers a possibility to study remote parts of the LMC. For example, a study of a sample of AGB stars observed by 2MASS would be spatially complete, as these

stars are bright in the NIR ($K_s < -6^m$) and hence can be identified, based on their colors, in the most distant regions of the LMC;

- *High-quality photometry.* Most importantly, the high quality of the NIR photometry by 2MASS ($\sigma \sim 0.03^m$) makes inference about LMC structure, populations and evolution meaningful, as the accuracy of the data is sufficient to support a detailed study.

To summarize, 2MASS survey is ideal for studies of spatial structure of the LMC, its populations, history and evolution.

1.2 Outline of Presentation

This work consists of three major parts, concerning the stellar populations of the Large Magellanic Cloud (Chapter 2), the structure of the LMC (Chapter 3) and its kinematics (Chapter 4).

Our primary tool for identifying and studying stellar populations of the LMC (Chapter 2) is NIR color-magnitude diagram (CMD) and isochrone analysis. Based on feature-rich CMD of the LMC from 2MASS data, we identify and characterize stellar populations in the LMC and by matching theoretical stellar evolution models we are able to draw conclusions about ages and masses of stars represented in the CMD. Isochrone fitting also gives the average metallicity of the LMC, and the average age of its stellar populations.

To characterize the spatial structure of the LMC and its components, one needs high-precision astrometric data (to study the structure in the plane of the sky), and high photometric accuracy (to resolve the structure along the line of sight). In addition, one needs a complete sample of standard candles, i.e. stars, whose luminosity is quantifiable. In Chapter 3, we use carbon-rich long-period variable stars identified from CMD as our standard candles. Studying their distribution and their apparent

luminosity function provides hints that LMC may be more complicated than a single disk.

Finally, in Chapter 4, we combine both photometric data from 2MASS and kinematic data available in the literature to model the LMC. The data are combined in the framework of maximum likelihood method, which is readily expandable to the case of additional photometric bands, etc. Adding kinematic data improves the inferential power of the method and confirms the existence of a photometrically distinct stellar population in the LMC, which is interpreted as the material out of the disk plane. This *stellar* material is spatially coincident with kinematically distinct gas, found in several previous studies (e.g., Luks & Rohlfs 1992, Kim et al. 1998). Not truly a 'conventional' halo, this material still acts to enhance the microlensing statistics toward the LMC. We demonstrate that even a small amount of material out of the disk plane can bring the optical depth toward the Cloud in agreement with observations.

CHAPTER 2

STELLAR POPULATIONS IN THE LMC

2.1 Data

The 2MASS has observed the entirety of the Large Magellanic Cloud and much of these data are included in the recent second incremental data release. Empirically, the photometry has signal-to-noise (SNR) ratio 10 at J, H, K_s magnitudes of 16.3, 15.3, 14.7, respectively, slightly better than the nominal survey limit. At these limits, we can observe all of the thermally-pulsing asymptotic giant branch (AGB) populations and part way down the red giant branch (RGB). The red clump, representing helium burning giants, lies ~ 2 mag below the sensitivity limit of these data. The extinction in near-infrared (NIR) is small throughout the LMC and negligible on average everywhere but the inner degree of arc. Together with the high quality of 2MASS photometry ($\sigma_m \sim 0.03^m$), overall zero-point stability (better than 0.01^m) and with reliable identification of LMC populations, the survey is ideal for studies of spatial structure of the LMC or its evolution.

Our LMC field is ≈ 250 sq. degrees and covers the range from 4^h00^m to 6^h56^m in right ascension and from $-77°$ to $-61°$ in declination (coordinates in J2000.0). The initial sample of 7,092,894 sources is drawn from the Working Survey Data Base and includes possible artifacts, such as filter glints and diffraction spikes from nearby bright stars, source confusion, and detection upper-limits. The known contaminants and flux statistics are well-characterized and identified during processing (Cutri et al. 1999). Eliminating artifacts and requiring detections at all bands with $\sigma_m le 0.11^m$ (SNR ≥ 10) leaves 1,246,304 stars. Unlike the released catalog, these data

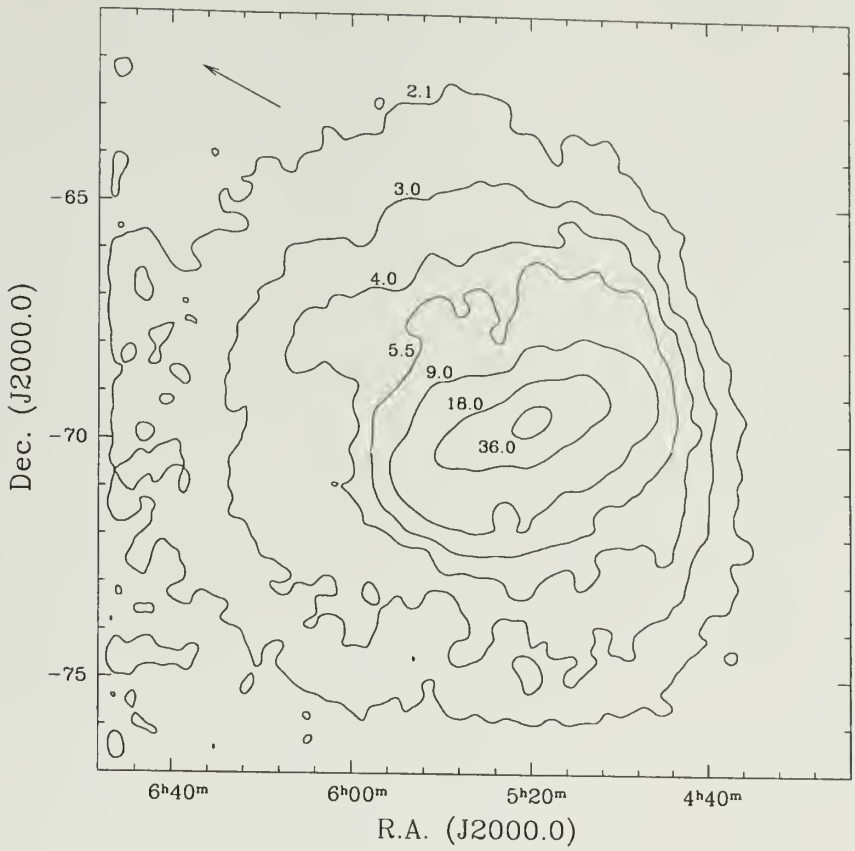

Figure 2.1. Distribution of 2MASS sources in the LMC field. Contour levels are labeled in units of 10^3 deg^{-2}. Arrow points in the direction to Galactic center.

contain multiple apparitions sources because of scan overlaps. We identify the multiple entries based on 1) spatial proximity ($|\Delta r| \leq 2''$), and 2) matching K_s-photometry ($|\Delta r| \leq 5\sigma$). Note that this procedure differs from that of the 2MASS catalog release (see Cutri et al. 1999). Our final sample contains 823,037 sources.

The spatial distribution of these stars is shown in Figure 2.1. The figure shows major structural components of the LMC, the bar and disk, immersed in the field of Galactic foreground. The gradient of the foreground sources (the direction to the Galactic center is indicated by an arrow) distorts the isopleths of the outer LMC disk. The source density near the optical center of the bar (at $\alpha = 5^h24^m$, $\delta_{J2000} = -69°44'$) exceeds 3.6×10^4 deg^{-2}. The expected mean separation among sources at this density,

$\zeta = 1/\sqrt{\rho} \sim 20''$, is much greater than 2MASS resolution and therefore confusion should not be significant (see also Wood 1994). As a separate check, we have examined the source counts as the function of magnitude in dense central fields and in more sparse fields in the outer LMC. The distribution of source counts as a function of magnitude have similar shapes in both dense and sparse regions, consistent with low confusion.

We have cross-correlated our sources with the database of long-period variables (LPV) from Hughes & Wood (1990). Their sample includes 376 large-amplitude Mira-like variables and 224 smaller amplitude semi-regular variables. We find 370 (98.4%) and 224 2MASS counterparts, respectively[1]. Three of the 'missing' large-amplitude variables are present in the raw 2MASS data, but are degraded by artifacts (two diffraction spikes and one blend). Of the remaining three, two are matched by stars of the appropriate magnitudes within $7''$ radius, and only one does not have any match to within $20''$ radius. All 134 Wolf-Rayet stars in the LMC (Breysacher 1999) have been observed by 2MASS (van Dyk et al. 1999).

2.1.1 K_s vs. K Photometry

The 2MASS photometric system is similar to CIT/CTIO system (Elias et al. 1982), except that it uses K_s band ($2.00 - 2.32\,\mu$m) rather than K band. The K_s ('K-short') bandpass is described by Persson et al. (1998). It was designed to reduce the ground-based thermal background. The transmissivity curve for the filter is given in Persson et al., who also compared K_{CIT} with K_s photometry for a set of solar-type stars and red standards (see their Tables 2 and 3, respectively). Based on their data, the difference $K - K_s$ shows no significant systematic trend in the color range $0 < J - K < 3$. The strongest trends follow from the presence of CO-band absorption, which affects the K filter more than the K_s filter. The absolute value of the difference $|K - K_s|$

[1]The search radius extends to $5''$ from the listed positions of sources.

is less than 0.05^m and we will assume $K_s = K_{CIT}$ in comparing CIT/CTIO system-based stellar sequences with 2MASS data.

2.1.2 Interstellar Reddening

One of the advantages of 2MASS as compared to optical surveys is low interstellar reddening, since extinction at 2μm is approximately 10 times smaller than in V. The values of interstellar reddening E_{B-V} found in the literature[2] fall in the range between 0.08 (Mateo & Hodge 1987) and 0.20 (Harris et al. 1997). The distribution of reddening from Harris et al. (1997) has non-Gaussian tail to high values. Greve et al. (1990) have reported values as high as $E_{B-V} = 1.1$, found from their investigation of dust in emission nebulae in the LMC. Bessell (1991) has summarized reddening determinations from photometry, stellar polarization and HI column densities to derive foreground and intrinsic mean reddening in the Clouds. He obtained typical LMC internal reddening of 0.06 (with substantial variations), and foreground reddening in the range $0.04 - 0.09$. Galactic foreground reddening can be surprisingly large in the outer regions of the LMC: Walker (1990) reported $E_{B-V} = 0.18 \pm 0.02$ at NGC 1841, about 15° from the optical center of the LMC. On the other hand, in the cluster GLC 0435-59 (Reticulum), 11° from the LMC center, the reddening is only $E_{B-V} = 0.03$ (Walker 1992). Zaritsky (1999) has indicated that reddening for F and G stars in the LMC is much less than that for OB stars and derived the average $< E_{B-V} >= 0.03$ for late-type stars in the disk.

In the present study, the data are not dereddened. Rather, each diagram shows the direction and magnitude of the reddening vector for a specified value of E_{B-V}. The reddening vector is based on relations from Koornneef (1982):

$$A_K = 0.189 E_{B-V}; \quad E_{J-K} = 0.651 E_{B-V},$$

[2]foreground plus LMC internal reddening

for $R = A_V/E_{B-V} = 3.1$. Information about the reddening may be obtained directly from 2MASS data from the analysis of the color-color diagram (see below).

2.2 Analysis of the Color-Magnitude Diagram

Figure 2.2 shows the color-color ($J - H$ vs. $H - K_s$) diagram of the LMC for 823,037 2MASS sources selected in §2.1. The diagram shows relatively few distinct features. The most prominent among them the extended 'arm' of the thermally-pulsing AGB stars (TP-AGB) in the upper right corner. Typical colors of LMC M giants are in the range $0.2 \lesssim H - K_s \lesssim 0.3$, $J - H \gtrsim 0.8$ (Frogel & Blanco 1990). Most stars on the extended arm, with colors redder than $J - K_s = 1.6$ are carbon-rich stars (Hughes & Wood 1990). Of those with the extremely red colors, $J - K_s > 2.0$, many probably possess dusty circumstellar envelopes. The sample contains ~ 2000 such sources. Their locus is consistent with the track following the reddening vector for $H - K_s > 1.0^m$. Figure 2.2 also shows fiducial color tracks for both giants and dwarfs from Wainscoat et al. (1992; hereafter W92). The two sequences overlap near $H - K_s = 0.15$, $J - H = 0.5$, since NIR colors of late G — early M type dwarfs are the same as colors of late F — early K type giants.

Because of the small number of features and the general compactness of the color-color diagram, its usefulness in discriminating the major populations is limited, especially in the overlap region, $0.5 < J - K_s < 0.8$. However, some LMC populations which occupy distinct regions in the diagram can still be identified based of their location in the color-color plot (see Figure 2.2). In particular, the color-color diagram is quite useful in identifying candidate sources with large infrared excess, such as young protostars, cocoon stars, or obscured AGB carbon stars.

The color-color diagram may be used to determine the reddening distribution. The giant population forms a tight branch in near-infrared colors. The reddening direction nearly coincides with $J - K_s$ and therefore the distribution in $J - K$ of

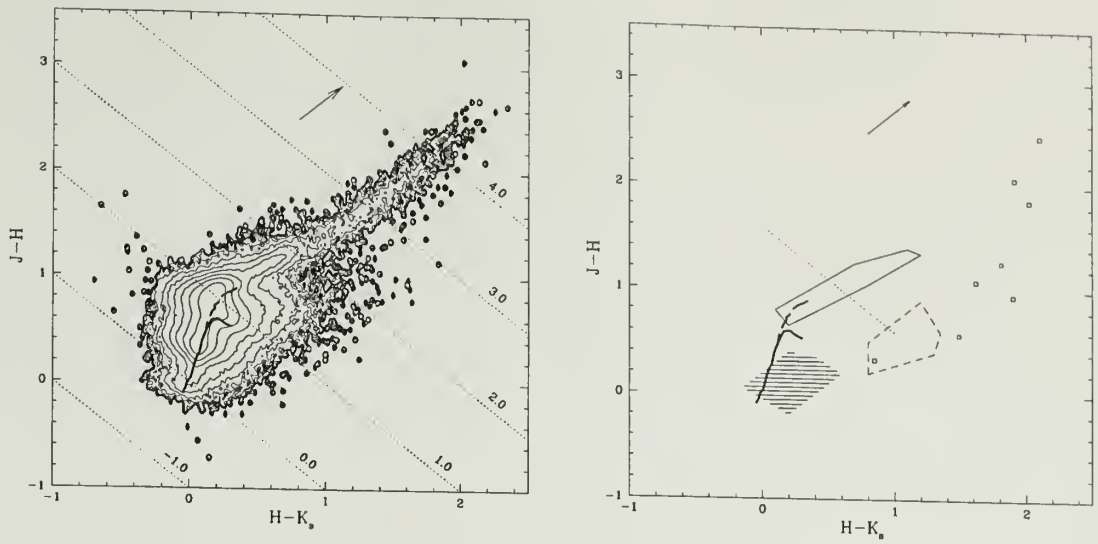

Figure 2.2 *Left panel*: Color-color diagram of the LMC field. Contour levels are logarithmic, from 2 to 6.5, spaced by 0.5. Diagonal lines are lines of constant $J - K_s$ values (marked). Color sequences of dwarfs (solid line) and giants (dashed line) from W92 are shown. Reddening vector for $E_{B-V} = 1.0$ (indicated by arrow) is based on relations from Koornneef (1982), assuming $R = 3.1$. *Right panel*: Color-color diagram showing approximate positions of some LMC populations. Shaded area corresponds to Wolf-Rayet stars (Breysacher 1999); region outlined by dashed lines encompasses known LMC B[e] stars (Gummersbach et al. 1995), open squares show individual observations of four LMC protostars (from Westerlund 1997). W92 fiducial colors of dwarfs (thick solid line) and giants (thick dashed line) are indicated. Region occupied by carbon stars in the sample of Costa & Frogel (1996) is shown with solid lines. Dotted line corresponds to $J - K_s = 1.6$. Reddening vector is drawn for $E_{B-V} = 1.0$.

a sample from narrow color interval in $J - H$ along the giant branch provides a sensitive diagnostic for reddening by dust. We considered a sample of sources in the range $0.78 < J - H < 0.85$. The resulting shift of the peak is $\Delta(J - K_s) < 0.03$ ($\Delta(J - K_s) < 0.06$) outside (inside) of the central region, suggesting only minor reddening on average on scales larger than 0.1 square degrees.

The color-magnitude diagram (CMD) presented in Figure 2.3 reveals a wide variety of details. Our goal is reliable identification criteria for LMC stellar populations based on their positions in the diagram. The CMD is hand-shaped with vertically-stretched 'fingers' (e.g., at $J - K_s$ colors of 0.4, 0.6, 1.1) due to varying distance

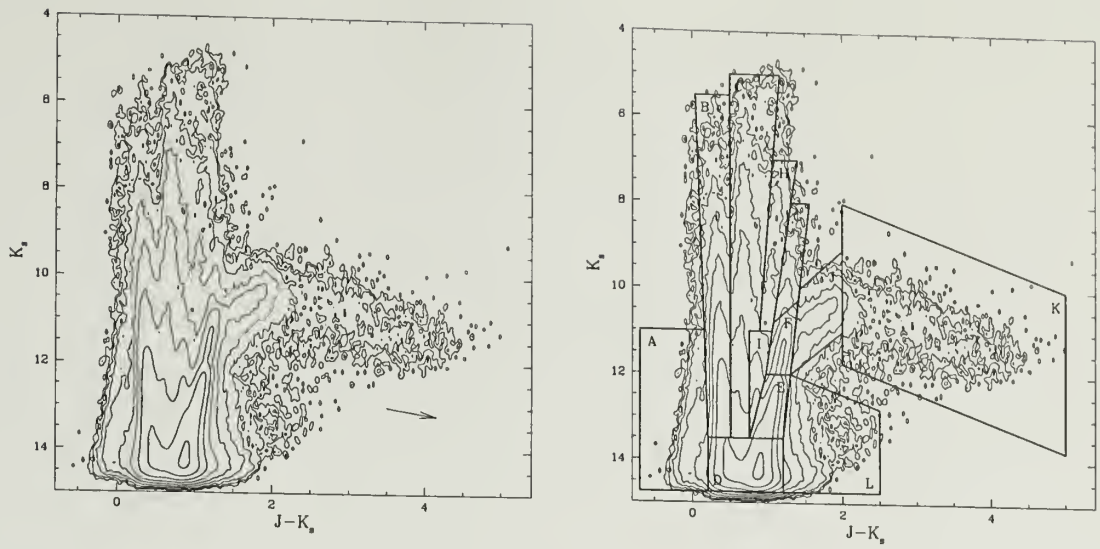

Figure 2.3 *Left panel*: Color-magnitude diagram of the LMC field. The density levels are logarithmic, from 2 to 6, spaced by 0.5. The reddening vector corresponds to $E_{B-V} = 1.0$. *Right panel*: The same diagram with highlighted 12 regions discussed in text. The regions correspond to major features of the CMD.

modulus for both Galactic and Magellanic sources. We have identified 12 regions shown in Figure 2.3 that highlight distinct features of the CMD. The regions are marked A through L and enclose 99.7% of the 823,037 sources in the field. To identify stellar populations in each region, we use a combination of several techniques. The Galactic foreground contribution is modeled by a synthetic CMD based on the tabulated near-infrared model of W92. The LMC populations are identified based on the infrared photometry of known populations found in the literature. In addition, we do a preliminary isochrone analysis, where we match the features of the CMD with Girardi et al. (2000) isochrones to derive the ages of populations and draw evolutionary connections among the CMD regions. The details of our population matching procedure are given in §2.2.1. In addition, we use the spatial density distributions of sources in each region to better discriminate local and LMC populations. The spatial distributions for each region are shown in Figure 2.4. In each panel of the figure, we plot source density contour levels of 15, 30, 60, 120, 240, 350, 480, 960, 1920, 3840,

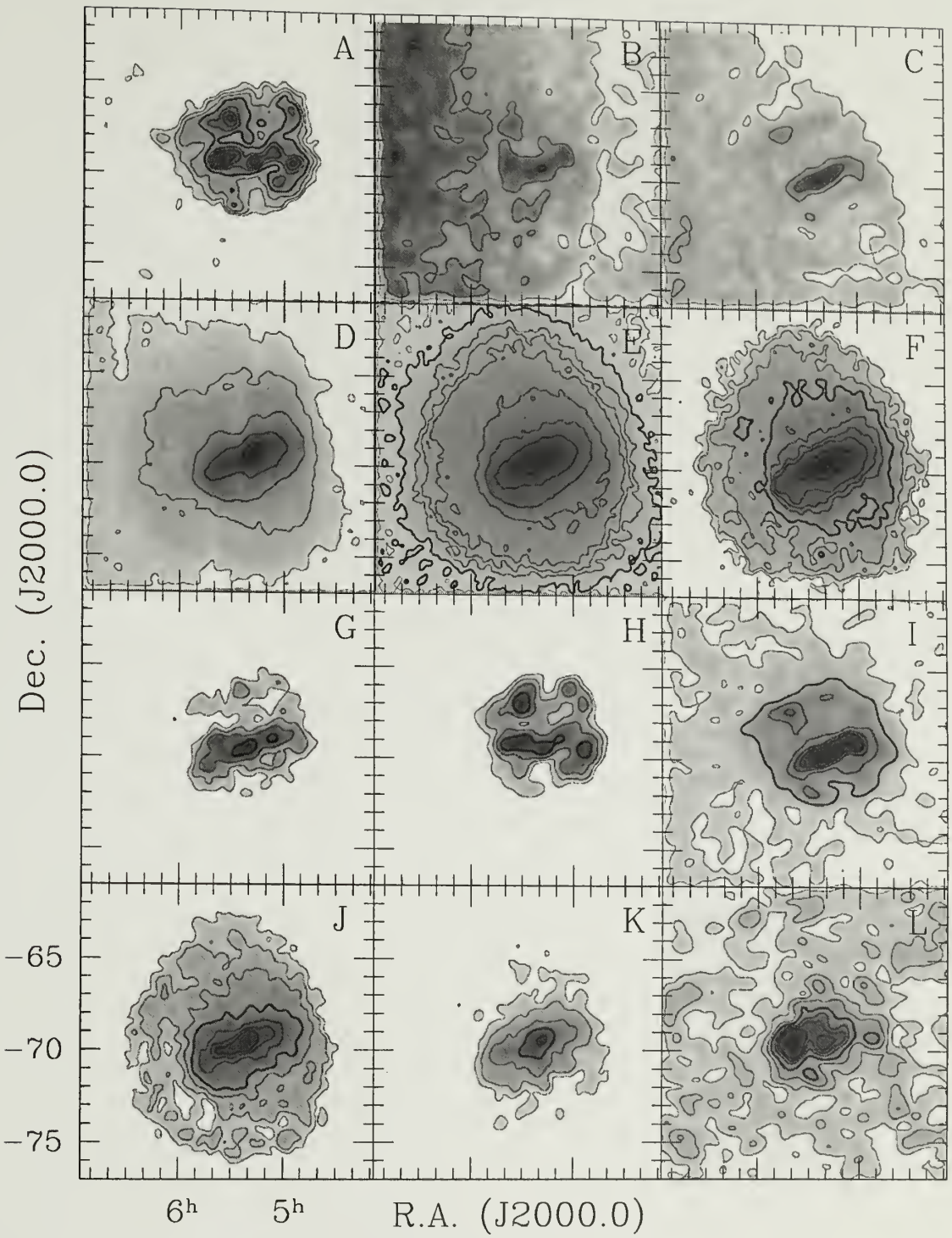

Figure 2.4 Spatial density distributions of sources in CMD regions. Letters correspond to the regions introduced in Figure 2.3. The distributions are kernel smoothed with a Gaussian kernel. The same sequence of contour levels is used in each panel (see text). Contour level of 120 deg^{-2} is highlighted.

7680, and 15000 deg^{-2}. The contour levels are selected both to show the underlying density profiles with maximum details and facilitate the comparison among different population densities. However, due to strong variations in relative density in the CMD, not all contour levels in this sequence are displayed: in panels E and I the lowest density contour corresponds to 60 deg^{-2}, in panels B and C the contours start from 240 deg^{-2}, and in very dense Region D the lowest contour level is 960 deg^{-2}.

2.2.1 Identifying Stellar Populations

The initial analysis of the CMD regions has two parts: 1) use of the spatial density distribution to estimate the location (Galaxy or LMC); and 2) use of the theoretical colors/isochrones to derive the properties of the population, such as age, approximate spectral class and distance modulus. Here we describe the procedure of identifying the populations, before examining each region of CMD in detail.

The CMD of the LMC field (Fig. 2.3) contains both Galactic and LMC populations. To quantify Galactic foreground, we use near-infrared model of W92, based on 8-25 micron point source counts. Galactic model of W92 has five structural components: exponential disk, bulge, stellar halo, spiral arms and molecular ring. The main contribution to the Galactic source density toward the LMC ($l = 280.5$; $b = -32.9°$) is the exponential disk. The source density due to other Galactic structural components combined does not exceed 0.0005% in any region of the CMD. The luminosity function in W92 model is represented by a sum of stellar classes, allowing independent estimate of the contribution of each class to the CMD. Each class of source is assumed to have a Gaussian distribution,

$$N(M) \propto \exp\left[-\frac{(M - M_\lambda)^2}{2\sigma^2}\right].$$

To model the Galaxy, we use the first 33 classes from Table 2 of W92 (Galactic dwarfs, giants and supergiants). The remainder (AGBs, planetary nebulae, etc.) are expected to give only a small contribution to source density and thus do not affect the CMD. In

the Galactic model, we use reddening parameters from Rieke & Lebofsky (1985). Dust is assumed to follow a double exponential distribution, with the radial scale length of the disk and the scale height of 100 pc. We reduced the magnitude dispersion σ of each stellar class by ten to accurately represent the CMD. Reducing σ results in a spiky differential luminosity function but this does not affect our application and the cumulative luminosity function remains well-approximated. Given the granularity of the model, the agreement between original W92 luminosity function and ours is acceptable. Our synthetic 'foreground' CMD is shown in Figure 2.5, along with the observed CMD of a Galactic field [3]. The agreement between the model and observed CMD is good, with few easily explainable discrepancies. For example, the extension of the CMD at $J - K_s \gtrsim 1$, $K_s \approx 13 - 14$ is due to the population of field galaxies (Jarrett et al. 1998).

Conclusions about the LMC populations in the CMD are made based on isochrone fitting or on empirical matching of populations found in the literature to features of the CMD. We use theoretical isochrones from Girardi et al. (2000). These isochrones supersede Bertelli's set (Bertelli et al. 1994), and use updated opacities and equations of state. The isochrones follow the evolution of low- and intermediate-mass stars ($0.15M_\odot < M < 7M_\odot$) from the main sequence up to the tip of the RGB or the start of the thermally-pulsing AGB. Some LMC populations are identified by matching morphological features of the CMD with colors of known populations from the literature. In particular, we use Cepheid colors from Madore & Freedman (1991), early M supergiant color sequence from Elias et al. (1985), and data on long-period variables from Hughes & Wood (1990). This matching is purely qualitative and is only used as a supplement. The fiducial colors of Galactic giants and supergiants from W92 model are unsuitable for LMC, since LMC has a lower metallicity com-

[3]To define our Galactic field, we combined three small fields, each ≈ 0.6 sq. deg. These fields were selected at the boundary of our LMC field where contamination from LMC source is minimal. At the time, other contiguous fields were not available.

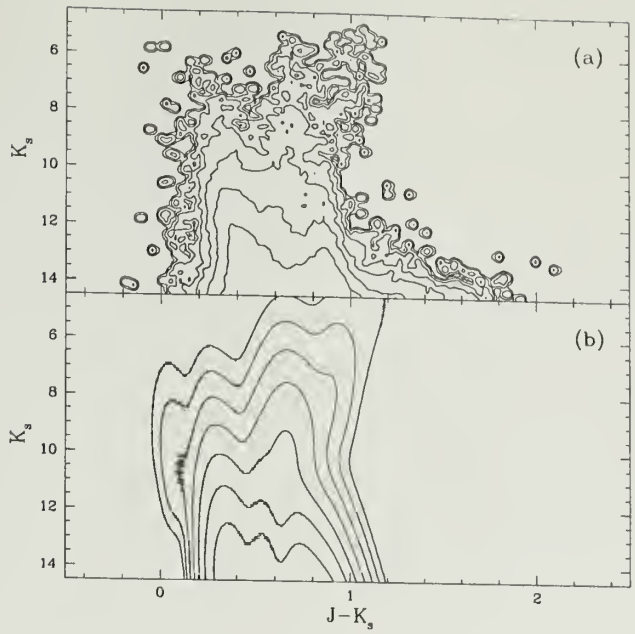

Figure 2.5 Comparison of (a) observed CMD of a Galactic field and (b) the synthetic Galactic CMD from W92 model, as explained in text. Densities in both diagrams are normalized to unity. The contour levels are logarithmic, from -0.5 to -3.5, spaced by 0.5. Similar plots for each stellar class and for each structural component of the Milky Way allows unambiguous determination of populations responsible for observed CMD features.

pared to the Milky Way. Moved to the LMC distance, $\mu = 18.5$, the W92 giant branch provides a poor fit to the observed RGB (see Figure 2.7 below).

2.2.2 Region A: Blue Supergiants, O Dwarfs

These blue-colored sources are readily identified as early type Population I stars in the LMC. This group of stars is the evidence of recent (< 30 Myr) star formation. Plotting the theoretical evolutionary tracks in the CMD (Figure 2.6) confirms that the region is populated by blue supergiants and brightest dwarfs (ZAMS). Only the hottest and most massive dwarfs of types O3—O6 can be seen in the LMC at $\mu = 18.5$. All other main sequence (MS) populations are too faint and fall below the limit at SNR = 10 imposed for this work. The supergiant population in the region are core helium-burning stars with masses $4 \lesssim M \lesssim 9 M_{\odot}$. These stars spend most of

their post-MS lifetimes as blue or red supergiants (Maeder & Meynet 1989) looping between Regions A and H of the CMD (cf. Figure 2.6b). Region A encompasses stars which are at the blue tips of their blue loops. While crossing Regions B and C, these stars enter the instability strip and become Cepheids (see §§ 2.2.3, 2.2.4).

The spatial distribution of these objects also clearly indicates an LMC population. The distribution is rather clumpy with several richest OB associations outlining the location of spiral arms and brightest and largest HII regions (e.g., 30 Dor). The density concentrations in Fig. 2.4A are consistent with the well-known superassociations and Shapley's Constellations (Martin et al. 1976, van den Bergh 1981). These youngest populations do not trace the bar of the LMC, in agreement with de Vaucouleurs & Freeman (1973). Quantitative analysis of the distribution (see Chapter 3) puts the centroid of the population at $\alpha = 5^h23^m$, $\delta = -68°48'$, about 1° north of the optical center of the bar.

The Galactic population of early dwarfs is readily seen in the CMD directly above Region A, blueward of Region B. The apparent magnitudes of these stars suggest a distance modulus between 5 and 10 ($r \sim 0.1 - 1$ kpc). In addition, this area of the CMD may also contain contribution from field blue stragglers and blue horizontal branch stars.

2.2.3 Region B: Galactic Disk F—K Dwarfs, LMC Supergiants

Region B is a vertically stretched band in the CMD with $J - K_s = 0.2 - 0.5$. This color cut isolates the main sequence turnoff of the halo ($J - K_s \approx 0.3$) and the disk ($J - K_s \approx 0.4$). The spatial density distribution increases toward NE corner of the field (Fig. 2.4B), i.e. toward the Galactic center, and indicates a predominantly Galactic population. The vertical extent in the CMD indicates a wide range of distance moduli for these stars. Based on relative population abundances in our synthetic Galactic CMD, we conclude that these sources are disk dwarfs of spectral classes in the range from late F to early K. These stars account for $\sim 90\%$ of the foreground source density

in the region. Their position in the CMD (see Figure 2.6a) suggests that the dwarfs have distance moduli $\mu = 3 - 10$ ($r \sim 0.04 - 1.0$ kpc). Galactic giants in the region are of types F—G, but their contribution to foreground source density is insignificant, smaller than 5%.

The distorted shape of the central isopleth in Figure 2.4B suggests presence of the LMC population in this region. The isopleth outlines the structure similar to the one seen in the central regions in Figure 2.4A. Note the overdensity near $\alpha = 5^h40^m$, $\delta = -69°$ and $\alpha = 5^h35^m$, $\delta = -67°30'$, marking positions of superassociations IV and V, respectively (Martin et al. 1976). Based on the colors, the LMC component is comprised of young blue and yellow supergiants, corresponding to spectral types A—G. This population includes luminous blue variables and short period Cepheids ($P \lesssim 50^d$). Figure 2.7b shows the Cepheid sequence based on PL relations for LMC Cepheids (Madore & Freedman 1991). Figure 2.6b also shows the colors of supergiants from W92 (Table 2). In addition, Region B contains the majority ($\gtrsim 80\%$) of the known LMC Wolf-Rayet stars. Most LMC Wolf-Rayet stars have infrared colors in the range $0 < J - K_s < 0.5$. Their numbers, however, are not significant to produce an observable effect in the CMD density.

2.2.4 Region C: Disk K Dwarfs and K Giants, Young Supergiants in the LMC Bar

Similar to B, Region C is stretched along the magnitude axis, indicating that the CMD feature is formed by sources at a range of distances. The colors of this population are in a tight range, $\Delta(J - K_s) \sim 0.3$. Our synthetic Galactic CMD suggests that most ($\sim 70\%$) of the observed density in this region is produced by disk K dwarfs at $\mu < 9$ ($r \lesssim 600$ pc). Disk K giants are also present in this region. Most of them have $\mu \sim 6 - 13$ ($r \sim 0.2 - 4$ kpc). They contribute $\sim 20\%$ of the foreground density. The inspection of isochrones in Figure 2.6a suggests that Galactic giants in this region are in the evolutionary phase of red clump/horizontal branch stars. The

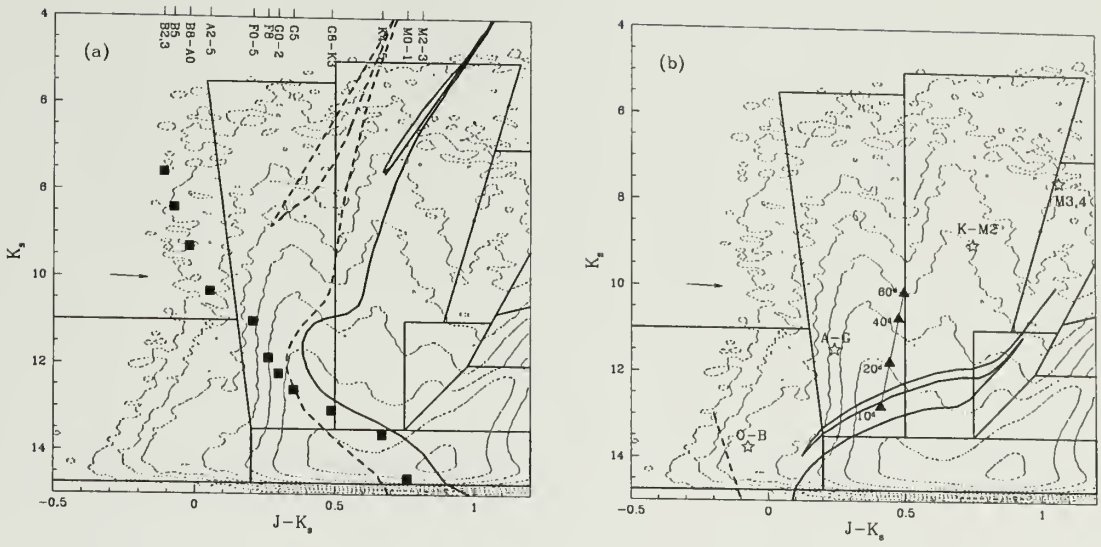

Figure 2.6 Part of the CMD showing Galactic and young LMC populations. (a) Galactic dwarf populations in 2MASS CMD. Solid line: theoretical isochrones for $\tau = 7$ Gyr, $Z = 0.019$, $\mu = 9.0$, $E_{B-V} = 0.1$, representing intermediate/old Galactic disk population; dashed line: isochrones for $\tau = 14$ Gyr, $Z = 0.0004$, $\mu = 9.0$, $E_{B-v} = 0.1$. Fiducial unreddened dwarf colors from W92 (for $\mu = 9.0$) are indicated by filled squares, with the approximate spectral types marked in the top axis. The reddening vector corresponds to $E_{B-V} = 0.2$. (b) Young LMC populations. Solid line shows the theoretical isochrone for $\tau = 60$ Myr, $Z = 0.008$, $\mu = 18.5$, $E_{B-V} = 0.2$. Empirical colors for Cepheids (Madore & Freedman 1991) are shown with triangles and mark the location of the instability strip in the diagram. Stars show fiducial color sequence of supergiants (I-II) from W92. Dashed line shows the tip of the ZAMS at $\mu = 18.5$, corresponding to hottest O3-O6 dwarfs. Colors of Cepheids, supergiants and O dwarfs are unreddened. The reddening vector corresponds to $E_{B-V} = 0.2$.

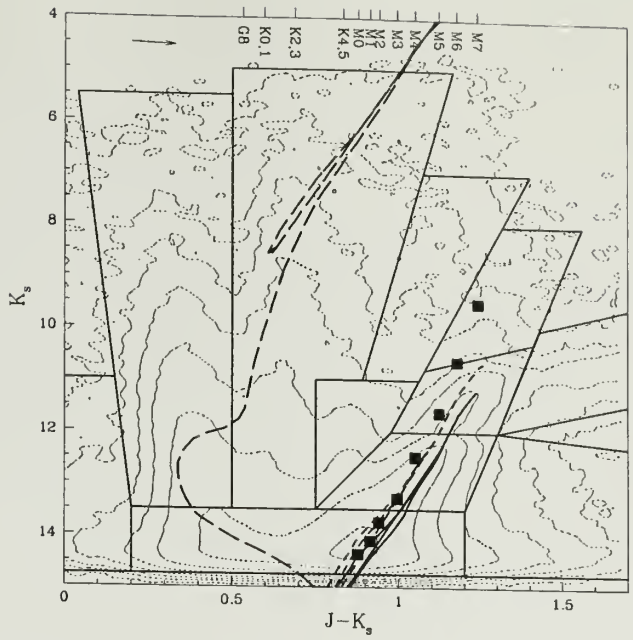

Figure 2.7 Part of the CMD showing intermediate and old LMC populations. Theoretical isochrones represent prototype populations — solid line: $\tau = 11$ Gyr, $Z = 0.004$, $\mu = 18.5$, $E_{B-V} = 0.2$; dashed line: $\tau = 4$ Gyr, $Z = 0.004$, $\mu = 18.5$, $E_{B-V} = 0.2$. The long-dashed line shows the isochrone for Galactic RGB stars, $\tau = 9$ Gyr, $Z = 0.019$, $\mu = 10.0$, $E_{B-V} = 0.0$. Fiducial unreddened RGB color sequence (W92) at $\mu = 18.5$ is shown with squares, with approximate spectral types along the sequence marked in the top axis. The reddening vector corresponds to $E_{B-V} = 0.2$.

intrinsic brightness and color of these stars ($M_K = -1.4 \pm 0.1$, $J - K_s = 0.6 \pm 0.1$) make them natural candidates in this region. Because of the narrow magnitude range of the clump, the source distribution in Region C along the magnitude axis could help constrain the structure of the Galactic disk.

The LMC population in Region C (seen in Figure 2.4C) is slightly older than youngest supergiants in Regions A, B. The central isopleths of the figure outline the bar of the LMC and show no overdensity at the positions of superassociations, seen in previous two regions. Most of the LMC sources in Region C have $K_s > 10.5$. The similarity in the shapes of central isopleths between Fig. 2.4C and 2.4I suggests they are lower mass young supergiants with ages $300 - 500$ Myr, evolving into Region I (Figure 2.6a). These stars trace the bar of the Cloud (Grebel & Brandner 1998).

Some contribution from more massive supergiants, including longer-period Cepheids ($P \lesssim 100^d$) may also be present.

2.2.5 Region D: Disk G—M Dwarfs and LMC RGB and Early AGB Stars

Region D is the most heavily populated area of the CMD: it includes more than a half of all sources in the sample. Because of its position in the CMD and the large color range it spans ($0.25 < J - K_s < 1.2$), this region is also the most inhomogeneous. The spatial distribution, shown in Figure 2.4D shows both the foreground and LMC populations (note the distorting effect of Galactic populations on outer LMC isopleths). The observed CMD is distinctly bimodal in this region, with the red half populated by RGB and early AGB stars in the LMC, and the blue half populated mostly by G—M dwarfs in the Galaxy. The AGB stars in the red half of the region ($J - K_s > 0.7$) are in their 'early-AGB' (E-AGB) phase, during which the energy is produced in the thick helium shell and outer hydrogen shell is extinguished. These stars have recently passed the base of the AGB, the so-called 'AGB-bump' at $K_s \approx 16$ that marks the transition from core to shell helium burning (Castellani et al. 1991). The AGB-bump was first observed by Hardy et al. (1984) in their CMD of the LMC bar. At only ≈ 1 mag brighter than the horizontal branch, this feature is not visible in the CMD in Figure 2.3 although it is present in deeper data (Figure 2.10). Empirically, most stars at the E-AGB are M type (oxygen-rich).

Only foreground stars are a minor contributor to the red half of Region D. (cf. Figure 2.5). Galactic dwarfs in this region have $\mu \sim 8 - 11$ ($r \sim 0.4 - 1.6$ kpc). Populations contributing insignificantly to the source density in this region include young supergiants, Cepheids, intermediate mass red stars in the vertically extended red clump (VRC; see §2.2.10).

2.2.6 Region E: Upper RGB and Tip of the RGB

Region E covers the upper RGB and includes the tip of the RGB (see §2.3). Most of these stars are on the first-ascent red giant branch; they have degenerate helium cores and hydrogen burning shells. The majority of these stars have ages anywhere between 1 and 15 Gyr old. The tip of the RGB is defined the helium flash, the ignition of the degenerate helium core in old (low-mass) stars (Renzini & Fusi Pecci 1989). Stars at the TRGB ignite helium in their cores and evolve rapidly to the horizontal branch. The region also contains a significant fraction of AGB stars in transition from E-AGB to TP-AGB, the stage at which the outer hydrogen shell is re-ignited (Iben & Renzini 1983). During thermal pulses, the star begins alternating between hydrogen and helium shell burning. The transition from E-AGB to TP-AGB is theoretically predicted to occur near the TRGB. While on the TP-AGB, these stars may also experience the shorter-term atmospheric pulsations that lead to Mira-type variability. Analysis of MACHO data (Alves et al. 1998b, Wood 1999) suggests that essentially all stars brighter and redder than the TRGB are variable. Most of the E-AGB stars in this region are M stars. Extrapolated to brighter magnitudes, the sequence of oxygen-rich AGB stars extends to Regions F and G (§§2.2.7, 2.2.8).

Stars in this region of the CMD carry the most weight in our analysis of the RGB+AGB luminosity function (see §2.3). Their spatial distribution is relatively smooth, showing strong disk and bar components. Note the absence of significant foreground population in Figure 2.4E: the outer contours are elliptical in shape. A small fraction of foreground sources in this region is due to disk M dwarfs. Their density is steadily increasing toward fainter magnitudes (cf. Figure 2.5).

2.2.7 Region F: O-Rich AGBs

Region F contains primarily oxygen-rich AGB stars of intermediate age ($\gtrsim$ 1 Gyr) that are the descendants of stars in Region E (note the similarity between Fig. 2.4E

and 2.4F). These are E-AGB and TP-AGB stars. The outer CMD isopleth in this region (Figure 2.3) is distorted and extends into Region J and indicates the presence of carbon stars in this region. During thermal pulses, the outer convective envelope may reach into the region where He has been transformed into C and bring carbon-enriched material to the surface. This dredge-up process leads to an increase in C/O ratio, and M stars in Regions F and G may become carbon stars. In the CMD, carbon stars form a 'branch' with redder colors, $J - K_s \gtrsim 1.4$ (see §2.2.11). Some fraction of Region F stars are LPVs (see Figure 2.8) and reddened supergiants. Figures 2.4F and G do not show isopleths due to a Galactic population. The Galactic component in these regions are negligible because it is both too bright and too red for disk M dwarfs and too faint for Galactic AGB stars.

2.2.8 Region G: AGB Stars

Region G contains the most massive stars with degenerate C/O cores. This is a population of young AGB, post core-helium burning stars with initial masses between about 5-8 solar masses. These are too short-lived to become carbon stars (0.1 – 1 Gyr old), but not massive enough to become red supergiants. Similar to Region F, this region also includes LPVs (Figure 2.8). The period-color relation for oxygen-rich Miras derived from Feast et al. (1989) rather closely traces the young AGB branch of the CMD outlined by Regions F and G. Region G lies at bright enough apparent magnitudes that the foreground density of M dwarfs is low, even in comparison to the relatively small number of O-rich luminous AGB stars in the LMC.

2.2.9 Region H: LMC K—M Supergiants, Galactic M Dwarfs, K—M Giants

Panel H of Figure 2.4 reveals an LMC population. The spatial distribution is similar to the distribution of young OB stars (Region A), suggesting that these objects are also relatively young. At $\mu = 18.5$, these stars are too bright to be normal M

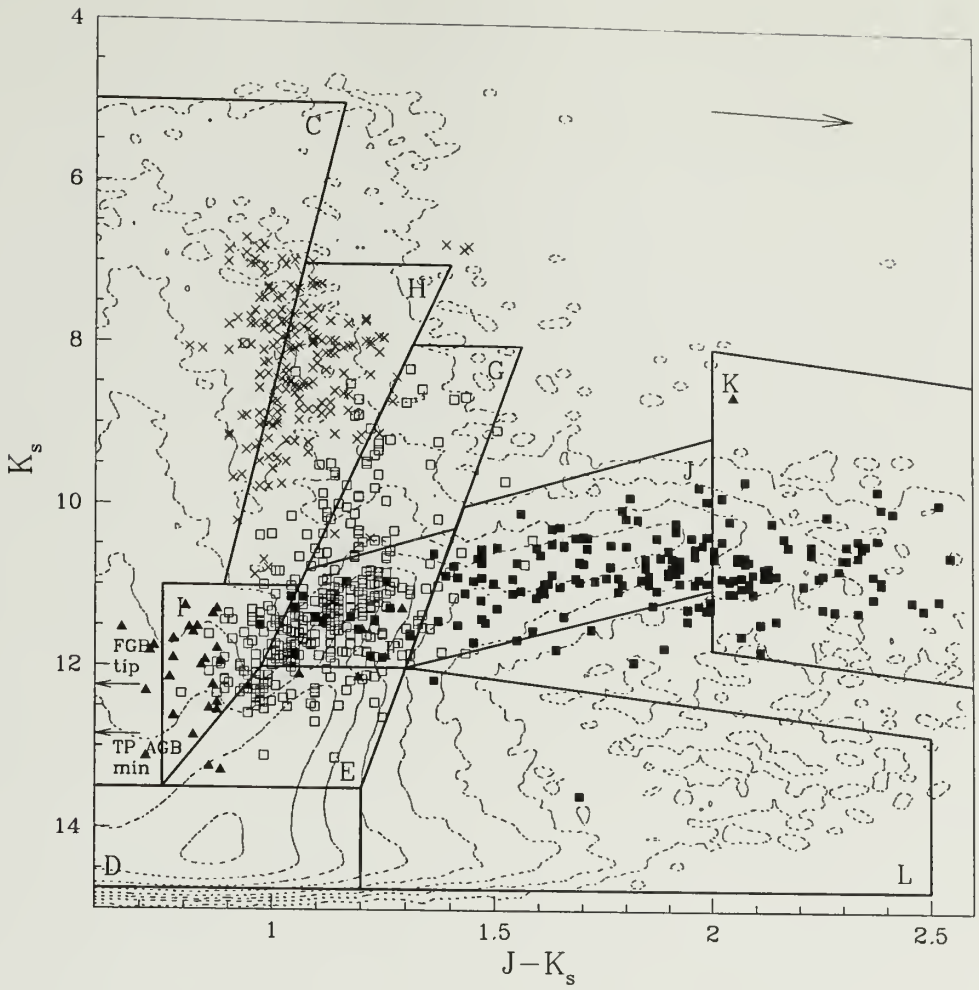

Figure 2.8 Portion of the CMD showing evolved stars. Crosses indicate M supergiants M1—M4 from Elias et al. (1985), solid triangles — K-type LPVs, open squares — M-type LPVs, and solid squares — C-type LPVs from Hughes & Wood (1990). Arrows at left show the theoretical tip of the RGB stars and the lower luminosity limit for thermally pulsing AGBs. The reddening vector is for $E_{B-V} = 0.5$.

giants. Based on their near infrared colors, we identify the Region H sources as supergiants of M type. They trace the spiral structure of the LMC and do not show significant overdensity in the bar of the Cloud, consistent with a young population. The masses of these stars are believed to be $\sim 2-9$ solar masses (Bertelli et al. 1985). In the evolutionary sequence, these stars are descendants of stars in Region A (note

the similarity between corresponding panels in Figure 2.4). These stars are also the high mass extension of the VRC.

In Figure 2.8, we plot the observed colors of M1—M4 supergiants from the sample of Elias et al. (1985). The colors of their sample occupy a portion of Region H, supporting our identification. The Galactic foreground consists of roughly equal contributions from disk K—M giants and M dwarfs, but their overall contribution to the source density in the region is only a few percent. This is confirmed by the absence of the Galactic isopleths in Figure 2.4H.

2.2.10 Region I: LMC Intermediate-Mass Red Supergiants, Galactic K—M Dwarfs

Region I is located at the center of the CMD, at $0.7 \leq J - K_s \leq 1.0$. The observed overdensity in the CMD is associated with the vertically extended red clump (Zaritsky & Lin 1997). This feature consists of intermediate mass stars and is the low-mass extension of the red supergiants (Region H). The VRC extends upward from the red clump at $K_s \approx 17$ and becomes visible in the CMD near $K_s = 13.5$. At the this point, the redward slope of the RGB is sufficient to distinguish the VRC.

The spatial distribution is dominated by the bar and shows traces of the spiral structure. We conclude that this LMC population is young, with the age $\lesssim 500$ Myr. The major LMC contributors to the source density in this region are K and M supergiants. This is supported by the overall similarity of LMC isopleths in Figures 2.4I and 2.4H, and also the fact that Region I is at the extension of Region H to fainter magnitudes and lower masses. Figure 2.8 shows K and M type Miras and SR variables in the sample of Hughes & Wood (1990). A significant fraction of their variables falls in this CMD region suggesting that some of these 2MASS stars also are variables.

The distribution in Figure 2.4I also reveals foreground populations. The Galactic foreground consists of M and late K dwarfs. Galactic giants contribute less than 5%

of the foreground density. The dwarfs are located in the disk, with distance moduli $\mu = 5 - 8$ ($r \sim 0.1 - 0.4$ kpc; Figure 2.6). The contribution from the Milky Way halo is smaller than 0.0005% by number for this and for all other regions of the CMD.

2.2.11 Region J: Carbon Stars in the LMC

At $J - K_s \gtrsim 1.4$, Region J sources are primarily carbon-rich TP-AGB stars. These stars are descendants of oxygen-rich TP-AGBs in Regions F and G. Their outer layers are enriched in C through convection from stellar interior. As mentioned in §2.2.6, most of these stars are long-period variables. The variability cannot be determined based on single epoch 2MASS data, but the well-defined sequence motivates a follow-up campaign. Figure 2.8 shows the sample of C-rich LPVs from Hughes & Wood (1990) overplotted on the 2MASS CMD. The contamination by M-type LPVs is small. The spatial distribution of C stars in the field is similar to the distribution of their precursors (Figs. 2.4F). The distribution is rather smooth and shows a loop of stellar material[4], which has been described by Westerlund (1964). The loop is the extension of the main northern spiral arm circling the main body of the system and returning toward the bar after a nearly complete turn.

Sources in this region of the CMD offer the best opportunity to study the three-dimensional structure of the LMC for two reasons. First, the spatial coverage of the Cloud achieved by 2MASS is total and allows to probe the entire LMC. Second, as long-period variables, Region J stars are potentially good standard candles, since their intrinsic luminosity can be characterized based on their period or color. Given the selection efficiency[5] and easily quantifiable intrinsic brightness through the period-luminosity-color relation (e.g., Feast et al. 1989), these stars are excellent probes of the LMC structure along the line of sight. Preliminary results (WN) indicate that the width of the intrinsic brightness distribution is smaller than $\sigma_M = 0.2$ magnitudes

[4]The feature to the SE of the bar in Figure 2.4J, near $\alpha \approx 5^h50^m$, $\delta \approx -73°$ represents a hole in the disk.

[5]owing to their extremely red colors, these stars are uncontaminated by other populations

in a narrow color range, $\Delta(J - K_s) \sim 0.1$. At this accuracy, these standard candles can resolve features in the LMC at $\Delta r \sim 4.5$ kpc. 2MASS detected approximately 10^4 potential carbon LPVs and these are sufficient to attain a reasonable confidence level in the inferred spatial structure. In Weinberg & Nikolaev (2000), we present our study of the three-dimensional structure of the LMC.

2.2.12 Region K: Dusty AGBs

An extension of Region J, Region K contains extremely red objects. We identify them with obscured AGB carbon-rich stars. Their large $J - K_s$ colors are due to dusty circumstellar envelopes ($E_{B-V} \gtrsim 1$). The latter is confirmed by the appearance of their spatial and CMD distributions: (1) Figure 2.4K shows traces of the spiral structure outlined by these sources; and (2) the distribution in the CMD spreads from the end of Region J in the direction of reddening vector. Matching with existing near infrared photometry of obscured AGB stars in the LMC (Zijlstra et al. 1996, van Loon et al. 1998) shows that most of these sources are indeed in this region of the CMD. Other extremely red populations could also be found here, e.g. 'cocoon' stars (Reid 1991), or OH/IR stars (Wood et al. 1992, van Loon et al. 1998). In addition, two of the known LMC protostars, N159-P1 and N159-P2 (Jones et al. 1986) also fall in this region.

2.2.13 Region L: Reddened LMC M Giants, Galactic M Dwarfs and 2MASS Galaxies

Stellar sources in Region L are reddened M giants in the LMC and a small number of reddened Galactic M dwarfs. However, a significant number of sources in this region are background galaxies. The predicted CMD density in Region L due to Galactic stars is too low even after the decrease in the photometric quality near the flux limit has been taken into account; the decreasing signal-to-noise ratio causes the apparent

widening of the contour levels (see Figure 2.5). According to Jarrett et al. (1998), more than 90% of 2MASS galaxies have colors redder than $J - K_s = 1$.

The spatial distribution of sources (Figure 2.4L) shows some overdensity toward the center of the LMC. The densest part of the diagram corresponds to the position of 30 Doradus complex. Traces of spiral structure of the LMC are also visible. Based on their colors, these sources are heavily obscured RGB stars in the LMC: they lie in the direction of the reddening vector from the RGB. The inferred reddening for these sources, $E_{B-V} \sim 0.5$, is consistent with the extended tail of the LMC reddening distribution (Harris et al. 1997). Region L also includes contribution from massive ($> 10 M_{\odot}$) protostars and ultra-compact H II regions, see Figure 2.8.

A population of dwarfs is implied by the outer isopleths of Figure 2.4L that show the increase in the direction of Galactic center. These are local M dwarfs in the disk of the Milky Way, with $\mu \sim 5 - 8$ ($r \sim 100 - 400$ pc).

2.3 Luminosity Function of LMC RGB and AGB Populations

We derive the LMC giant branch luminosity function (LF) from the color-magnitude diagram after subtracting Galactic foreground. Since we did not have the access to Galactic data at the time, the foreground contribution was estimated from three small fields located at the edges of our LMC field. We then scaled the resulting foreground CMD to the entire LMC field by using the estimate for the number of Galactic sources from our synthetic model. Figure 2.9a shows the field CMD for LMC populations only, after subtracting Galactic foreground. The expected Galactic source counts is $\sim 4 \times 10^5$ or about 50%. The uncertainties in the observed CMD and in the Galactic model result in negative density regions (dotted contours) in Figure 2.9. The average negative density is $-10^{3.2}$ mag^{-2}.

The luminosity function of the LMC giants is obtained by projecting the color-magnitude diagram perpendicular the straight line fit to the giant branch. The function is normalized to unity. Numerical values for the RGB luminosity function are given in Table 2.1 and shown in the inset to Figure 2.9. A strong feature of the LF is a significant excess at $K_s \approx 12.5$, due to the TRGB. From the analysis of the derivative of the apparent luminosity function, we derive the position of the TRGB at $K_s = 12.3 \pm 0.1$. Brightward of the TRGB, the number of RGB stars drops off. The increase in the number density at the faint end, $K_s \gtrsim 14$, is due to the increased contribution from Galactic M dwarfs (cf. Fig.2.5). At the bright end of the magnitude range, $11 < K_s < 12$, the luminosity function is nearly constant. It is also well above the expected number from extrapolated RGB counts. The fraction of RGB stars is small in this magnitude range and most of the stars contributing to the LF are on the AGB. As discussed above (§2.2.7), these stars tend to be oxygen-rich, but carbon-rich AGBs (and LPVs) are also present.

We select two $2^\circ \times 1^\circ$ fields, one near the optical center of the bar, and the other one at $\alpha = 93^\circ$, $\delta = -67.5^\circ$ (J2000.0), near the outer loop, to compare the observed M giants luminosity functions in distinct LMC environments. The outer field is probing the LMC's outer loop delineated by the evolved stars (see §2.2.11). For each of the fields, we subtract the estimated Galactic foreground density scaled to the surface area of the fields. Similar to Fig. 2.9a, inaccuracies in both observations and models produce negative density regions. However, the average negative density in these regions is small compared to the giant branch, only $-10^{0.4}$ mag^{-2} for bar region and $-10^{0.5}$ mag^{-2} for loop field. Comparing the two CMDs qualitatively, we note that contribution of young OB stars and supergiants, at $J - K_s \lesssim 0.2$, appears stronger in the central regions of the LMC. Even though the luminosity functions in the respective fields appear different, careful analysis shows that the difference is superficial: χ^2/d.o.f.≈ 0.2, which gives no motivation to entertain any difference in

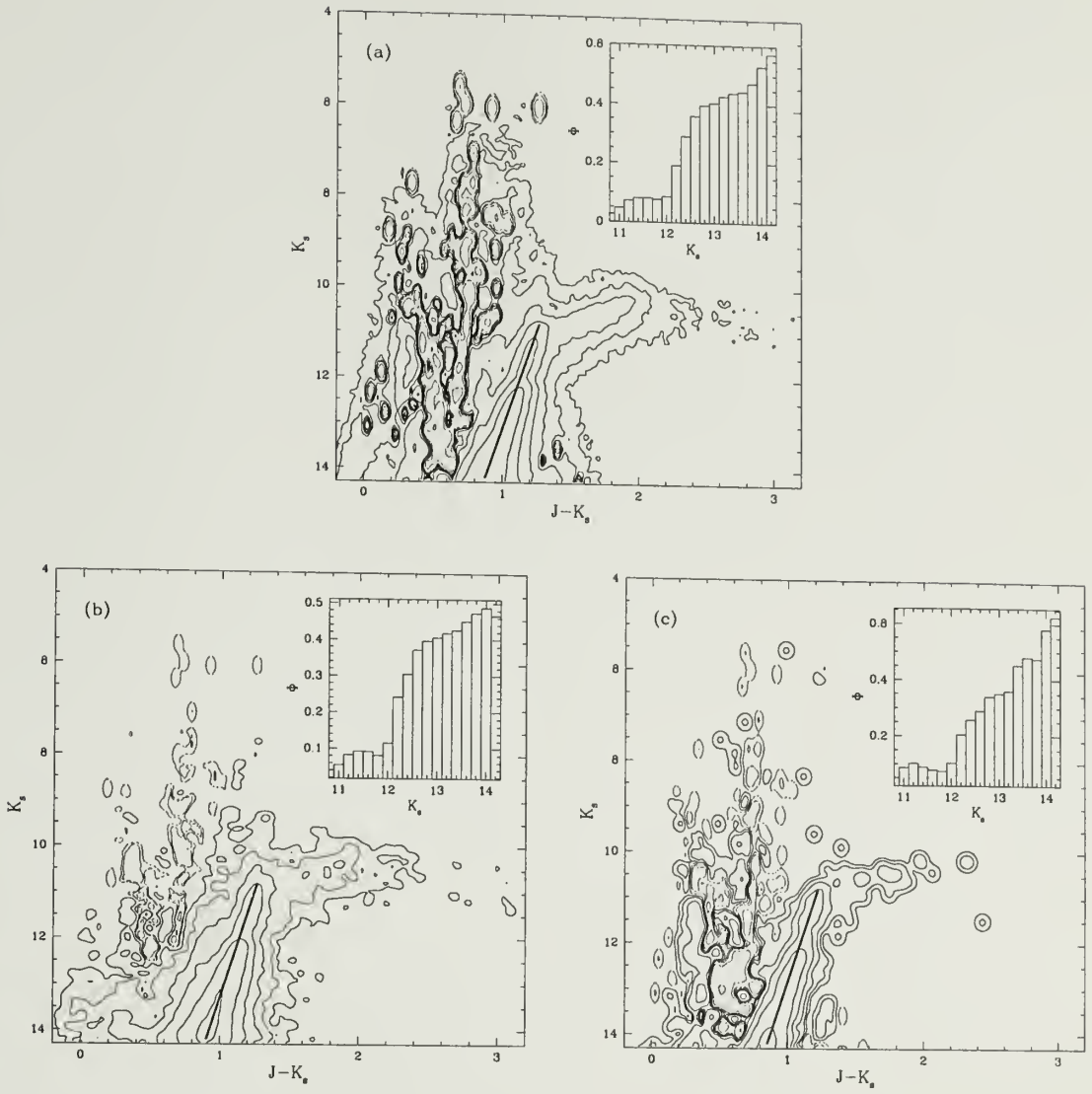

Figure 2.9 Color-magnitude diagrams of the LMC populations and the apparent luminosity functions of the LMC giants. Panels show CMDs of (a) entire field, (b) bar field, and (c) outer loop field (see text). The CMDs are constructed by subtracting Galactic foreground contribution from CMD in Figure 2.3, normalized to the same sky area. Contour levels in all panels are logarithmic, spaced by 0.5, from 2.5 to 5.5 (a), 2.0 to 4.0 (b), and from 1.0 to 3.5 (c). Dotted lines indicate negative density regions. Luminosity functions, normalized to unity, are shown in the insets of each panel.

the parent populations. The bar LF is similar to the luminosity function of the entire field (Figure 2.9a), which is not surprising because the source density in the LMC field is dominated by the LMC bar. The bar luminosity function also has a pronounced TRGB at $K_s \approx 12.3$ and a number density due to AGBs at $11 < K_s < 12$. The sharp increase due to Galactic M stars, seen in Figure 2.9a at $K_s \gtrsim 14$, has disappeared in the bar field, because we have boosted the ratio of LMC/Galactic counts by narrowing down the field to the area of greatest LMC density. The off-bar LF shows only a mild increase in the source counts at the location of TRGB, but has the same, roughly constant profile at $K_s < 12$, due to the AGB population, visible in the other two luminosity functions. To quantify both LFs, we present their numerical values in Table 2.1. The luminosity functions are given in relative units, normalized to unity. The table also gives the source counts for the LMC giant branch. For the entire LMC field we present the total counts per magnitude bin, and for the two smaller fields we give stellar density (counts mag^{-1} deg^{-2}).

We fit theoretical isochrones (Girardi et al. 2000) to each giant branch in Figure 2.9 to test for differences in metallicity between central and outer parts of the LMC. We chose 20 equally-spaced grid points in K_s magnitude between 14.3 and 12.3 and compute the peak in the distribution in $J - K_s$ at these fixed K_s points. The difference between an isochrone (model) and the RGB (data) is characterized by the cost function (mean integrated square error):

$$f = \sum_j [(J-K_s)_{j,\,RGB} - (J-K_s)_{j,\,iso}]^2 + w\,[K_s^{TRGB} - 12.3]^2, \qquad (2.1)$$

where the second term is weighted measure of the match between theoretical magnitude at helium flash and observed TRGB. The weight w is an adjustable parameter on the order of unity. The cost function (2.1) is minimized on a grid of parameter values, where the free parameters are the log-age τ, metallicity Z, distance modulus μ and average reddening E_{B-V}. The best fit isochrones are as follows: $(\tau, Z, \mu, E_{B-V}) = (9.8 \pm 0.3, 0.004^{+0.002}_{-0.001}, 18.45 \pm 0.11, 0.21 \pm 0.07)$ for the central field

Table 2.1 Apparent luminosity function and source number density for the LMC giants.

K_s	Φ (mag^{-1})[a]			log number density (mag^{-1} deg^{-2})		
	LMC	Bar	Loop	LMC[b]	Bar	Loop
10.8	0.03	0.04	0.05	3.16	2.17	1.16
11.0	0.05	0.06	0.09	3.44	2.32	1.39
11.2	0.07	0.08	0.10	3.61	2.50	1.46
11.4	0.08	0.09	0.09	3.65	2.54	1.40
11.6	0.08	0.09	0.08	3.66	2.54	1.35
11.8	0.08	0.08	0.08	3.64	2.48	1.33
12.0	0.09	0.12	0.11	3.68	2.63	1.47
12.2	0.19	0.24	0.21	4.04	2.96	1.76
12.4	0.29	0.31	0.26	4.22	3.06	1.87
12.6	0.36	0.37	0.30	4.31	3.14	1.92
12.8	0.40	0.40	0.35	4.35	3.17	1.99
13.0	0.40	0.41	0.36	4.36	3.18	2.00
13.2	0.43	0.42	0.36	4.39	3.20	2.01
13.4	0.44	0.43	0.45	4.39	3.20	2.11
13.6	0.44	0.45	0.47	4.40	3.23	2.14
13.8	0.47	0.47	0.46	4.43	3.25	2.13
14.0	0.54	0.49	0.57	4.48	3.26	2.22
14.2	0.58	0.47	0.61	4.51	3.24	2.25

[a]The luminosity functions are given in relative counts per magnitude.
[b]Number density for the entire field is given as source counts per magnitude bin.

and $(\tau, Z, \mu, E_{B-V}) = (9.8 \pm 0.4, 0.004^{+0.002}_{-0.001}, 18.50 \pm 0.13, 0.13 \pm 0.09)$ for the outer field (all errors statistical). These results imply an age range for RGB populations from 3 to 13 Gyr with an average of 6 Gyr. The slope degeneracy of the isochrones in the RGB makes specific tests of star formation history difficult. In particular, our preliminary RGB isochrone analysis cannot distinguish between a continuous and single/multiple burst star formation history of the Cloud prior to approximately 4 Gyr ago. Overall, our results do not indicate a radial metallicity gradient and provide only marginal evidence for larger reddening in central fields. The absence of strong metallicity gradients in the LMC is in agreement with results of Olszewski et al. (1991), who found no evidence for abundance gradient for cluster system. Constant C/M star ratio across the face of the LMC (Westerlund 1997) and Cepheid abundances

(Harris et al. 1983) also support this result. Our results imply the range of abundances for field populations -0.8 <[Fe/H]< -0.5, which is in good agreement with the mean abundance [Fe/H]= -0.58 ± 0.05 (systematic) ± 0.30 (statistical) for the inner LMC disk (Cole 1999). Our results agree with the disk abundance [Fe/H]= -0.7 (Cowley & Hartwick 1982), and with results of Bica et al. (1998), who derived the range -1.1 <[Fe/H]< -0.4 with the average < [Fe/H] >= -0.61 ± 0.11 from fields in the outer disk of the LMC.

The adopted detection threshold (SNR = 10; §2.1) leads to the effective completeness limit of $K_s \approx 14.3$ in our data (cf. Figure 2.3). With this flux level, only the upper RGB is visible, leaving out both the AGB-bump at $K_s \approx 16$ and the red clump at $K_s \approx 17$. To resolve the giant branch down to $K_s \approx 16-17$, we use 2MASS engineering data, which includes six LMC scans, positioned as shown in Figure 2.10. Each of the 'deep' scans has six times the standard exposure. The color-magnitude

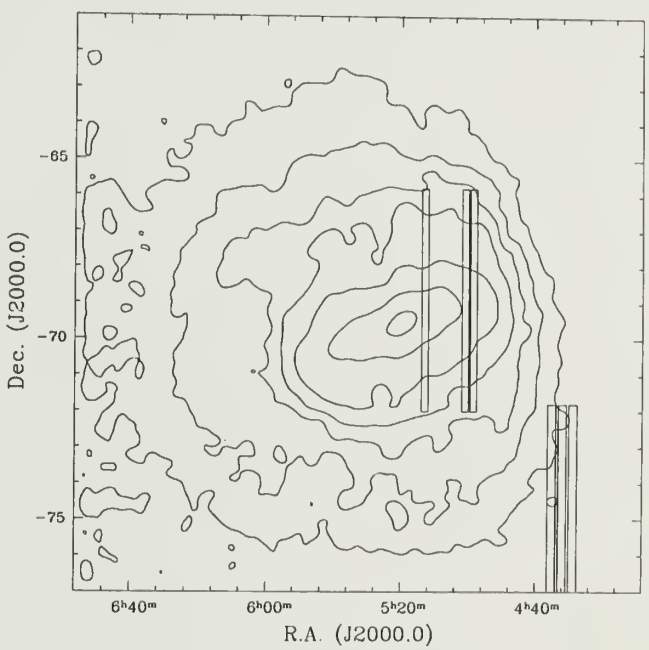

Figure 2.10 Positions of six 'deep' scans in the sky. Each scan has six times the standard integration time.

diagram of the deep data is shown in Figure 2.11. Total number of sources in the

diagram is 87,093, of which 69,878 ($\sim$ 80%) are in the three bar scans. Because of the bar dominance in deep data, the CMDs of the entire deep sample and the bar scans (Figs. 2.11a and 2.11b, respectively) are similar. The increased sensitivity reaches the AGB-bump at $J - K_s = 0.7$, $K_s = 15.8$, but still shy of the red giant clump. As with the main dataset, we quantify the deep RGB population by fitting isochrones. The resulting best fit parameters are $Z = 0.004^{+0.002}_{-0.001}$, $\tau = 9.7 \pm 0.3$, $\mu = 18.50 \pm 0.12$, $E_{B-V} = 0.19 \pm 0.08$. The uncertainties here are statistical errors, derived from the shape of the χ^2 surface near minimum. The range of ages for RGB populations inferred from the deep data is similar to that derived for the main data set: from 3 to 10 Gyr, with the average of 5 Gyr. The other parameters are also consistent with the values derived from the regular 2MASS data. These estimates are in good agreement with recent results in the literature, e.g., the average reddening $E_{B-V} = 0.20$ (Harris et al. 1997); the LMC distance from Key Project, $\mu = 18.5$ (Mould et al. 1999); the LMC distance from TRGB, $\mu = 18.59 \pm 0.09$ (Sakai et al. 1999).

2.4 Summary

We have analyzed the near-infrared CMD of the Large Magellanic Cloud and identified the major stellar populations. The populations are identified based on isochrone fitting and matching the theoretical CMD colors of known populations to the observed CMD source density. Tables 2.2 and 2.3 summarize the contents of the CMD regions.

The main points of this preliminary analysis of 2MASS data are the following:

- The quantity and the quality of 2MASS data allow unprecedented look at the entire LMC. 2MASS has produced a rich sample of LMC sources, a few million stars, with the photometric accuracy of 3-4%. JHK 2MASS photometry is potentially useful for studying the star-formation history of the Cloud. Cross-

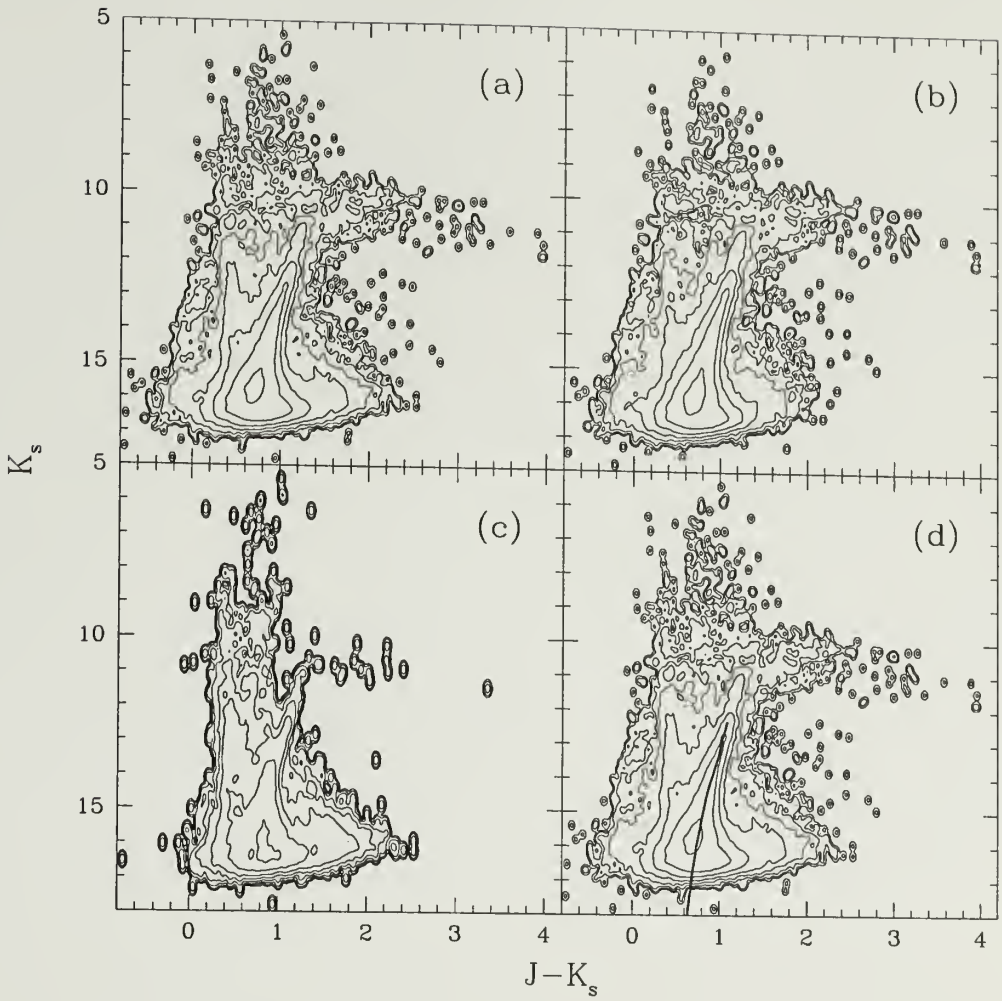

Figure 2.11 'Deep' color-magnitude diagrams of the LMC. Panels show CMDs of (a) all six deep scans combined, (b) three bar scans, and (c) three outer field scans. Panel (d) is the same as panel (a), except also shows the best-fit isochrone for the RGB. Galactic foreground is not subtracted. The contour levels are spaced logarithmically by 0.5, from -3.6 to -0.1 (a,b,d), and from -3.7 to -0.2 (c). The lower RGB is enhanced as compared to Figure 9. Weakness of RGB in panel (c) indicates strong relative contribution from Galactic foreground. The red giant clump is just below the completeness limit in this diagram, at $K_s \approx 17$, $J - K_s \approx 0.65$.

Table 2.2 Regions of interest in the 2MASS CMD of the Large Magellanic Cloud.

Region	N_{src}	f_{Gal}[a]	Region boundaries	Dominant Spectral Types[b]
A	6,659	0.15	$11 < K_s < 14.75$	
B	77,204	0.80	$J - K_s < 0.2$ $5.5 < K_s < 13.5$	**B-A I-II, O3-O6 V**
C	62,713	0.80	$0.2 < J - K_s < 0.5$ $5 < K_s < 13.5$	F-K V
D	440,472	0.45	$0.5 < J - K_s \lesssim 0.8$ $13.5 < K_s < 14.75$	K V, K III
E	166,263	0.05	$0.2 < J - K_s < 1.2$ $12 < K_s < 13.5$	**K-M III**, F-M V
F	22,134	0	$0.9 \lesssim J - K_s \lesssim 1.2$ $10.5 \lesssim K_s < 12$	**M III**, M V
G	1,438	0	$1 \lesssim J - K_s \lesssim 1.3$ $8 < K_s \lesssim 10.5$	**M, MS**
H	2,450	0.05	$1.2 \lesssim J - K_s \lesssim 1.5$ $7 < K_s < 11$	**M, MS**
I	21,986	0.55	$1 \lesssim J - K_s \lesssim 1.3$ $11 < K_s \lesssim 13$	**M I-II**
J	8,229	0	$0.75 < J - K_s \lesssim 1$ $9.5 \lesssim K_s \lesssim 11.5$	**K-M I-II**, K-M V, M III
K	2,212	0	$1.4 \lesssim J - K_s < 2$ $9 \lesssim K_s \lesssim 13$	**C III**
L	8,940	0.01	$2 < J - K_s < 5$ $12.5 \lesssim K_s < 14.75$	**C III**
			$1.2 \lesssim J - K_s < 2.5$	M late V

[a]Fraction of Galactic sources estimated from synthetic W92 model
[b]Based on $J - K_s$ color and W92; **LMC** populations in boldface

correlating 2MASS database with existing catalogs will provide homogeneous and accurate IR photometry of supergiants (Sanduleak catalog), Wolf-Rayet stars (Breysacher catalog), Cepheids (OGLE and EROS datasets), LBVs and LPVs;

- The color-color diagram is generally ill-suited to distinguish between giant (III) and dwarf (V) populations, especially in the color range $0.5 \leq J - K_s \leq 0.8$. Nevertheless, the diagram may be useful in identifying some candidate LMC objects with infrared excess, such as obscured AGB stars, B[e] stars, or LMC

protostars. In addition, the distribution of $J - K_s$ colors of a population in a narrow $J - H$ color range is a sensitive reddening test;

- Major populations can be identified based on the comparison of observed CMD features with theoretical positions of known populations. Isochrone overplotting provides tentative age and metallicity estimates. We identify a substantial LMC population of AGBs ($\gtrsim 10^4$ sources), and obscured AGBs (~ 2000 sources);

- The luminosity function of the LMC giants is determined and tabulated. We find the RGB tip at $K_s = 12.3 \pm 0.1$. Our preliminary analysis of luminosity functions in two test fields suggest that luminosity function is the same in the bar and the outer regions of the Cloud;

- Fitting isochrones to the location of the giant branch (including TRGB) gives metal abundances consistent between fields. In particular, we derive average metallicity $Z = 0.004^{+0.002}_{-0.001}$ for our fields. Analysis of deep data gives the same average metallicity. Our results confirm the absence of strong radial metallicity gradient in the field populations of the LMC;

- The estimates of the distance modulus obtained from our isochrone fits to the RGB, are consistent with each other and the most recent results in the literature. The average reddening is marginally different between the bar and the outer field, the E_{B-V} for the bar field being greater. Distance modulus and reddening estimates from the analysis of deep data produces similar values;

- The ages of dominant RGB populations fall in the range from 3 to 13 Gyr, with the average age $\sim$ 6 Gyr. Isochrone fits to the deep data produce similar age interval, from 3 to 10 Gyr, with the average age $\sim$ 5 Gyr. A more detailed isochrone analysis is required to draw conclusions about the history of star formation in the LMC prior to $3 - 4$ Gyr ago;

- Carbon-rich long-period variables are noted as potential standard candles. Due to their significant numbers and narrow luminosity range (which may be parametrized through a period-luminosity or luminosity-color relations), these stars are ideally suited for studying the structure of the LMC along the line of sight.

Table 2.3 LMC stellar populations in the 2MASS CMD.

Stellar types	Regions[a]	Typical age
Very Young		
Centrally concentrated, localized to star-forming regions		
trace spiral structure, weakly trace bar		
O3-O6 dwarfs	**A**	$\lesssim 10$ Myr
Red supergiants, $5-8M_\odot$	**H**	$\lesssim 50$ Myr
Luminous AGB stars, O-rich LPVs,		
$M \approx 5-8M_\odot$	**G**, H, F	$\sim 40-100$ Myr
Blue and yellow supergiants, LBVs	A, B, C	< 100 Myr
Massive protostars,		
Cocooned OB associations	L	$\lesssim 5$ Myr
Young		
Bar-dominated		
Luminous E-AGB stars	**G**, H	$200-800$ Myr
Core He-burning giants,		
supergiants, $M \sim 2-5M_\odot$, LPVs	**I**, D, C, H	$100-900$ Myr
E-AGB, oxygen-rich LPVs	F, E, D	$\lesssim 1$ Gyr
Carbon stars, C-rich LPVs	J, K	$\lesssim 1$ Gyr
Intermediate and Old		
Disk and bar		
Low- and intermediate-mass RGB stars	**D**, **E**, L	$1-15$ Gyr
O-rich AGB stars, M-S-C stars	**F**	$1-4$ Gyr
C-rich TP-AGB stars	**J**	$1-4$ Gyr
Dust-enshrouded TP-AGB, carbon stars	K	$1-4$ Gyr
Foreground and Background		
Disk populations and extragalactic component		
Disk main-sequence turnoff stars	**B**	$\lesssim 7-9$ Gyr
Nearby K dwarfs, red clump and red HB stars	**C**, I	$\lesssim 9$ Gyr
Local F-M dwarfs	**D**, E	varies
Background galaxies	**L**	

[a]Where a population is the dominant contributor to a region, it is labeled in bold type.

CHAPTER 3

LMC STRUCTURE FROM ANALYSIS OF PHOTOMETRIC DISTRIBUTION

3.1 Introduction

Morphologically, the LMC is an irregular barred spiral galaxy with three spiral arms and an extended outer loop of stellar material (de Vaucouleurs & Freeman 1973). Based on deprojection and photometric distances (e.g. de Vaucouleurs 1957, 1980), its disk is inclined at an angle of 27° to the plane of the sky. The disk exhibits solid body rotation out to 2.5° with a rotation center at 5^h21^m, $-69°17'$ (1950), about 0.6° north of the optical center of the bar. This kinematic signature is present in a variety of tracers: HI gas, planetary nebulae, HII regions, supergiants, CH stars, etc. Freeman et al. (1983) have examined kinematics of rich star clusters with ages between 100 Myr and 10 Gyr. They found that young clusters rotated with HI gas, while the older ones (SWB VII; Searle et al. 1980) formed a flattened rotating system with dispersion along the line of sight $\sigma \sim 18$ km/s. A later study of more extended sample of outer LMC clusters (Schommer et al. 1992) confirmed the absence of isothermal pressure-supported spheroid. All this has led to the standard view that the LMC is a *geometrically thin* object.

However, recent studies have suggested that the LMC may have an extended component. First, the evidence for a flattened spheroid population was found in the kinematics of old long-period variables (Hughes et al. 1991). Kunkel et al. (1997) describe a population of carbon stars out to 12 kpc from the LMC center. These authors interpret these in the context of a thin disk model and derive a rotation

curve and mass estimate. However, Weinberg (2000) argues that the LMC should be evolving rapidly in the Milky Way tidal field, based on both analytic calculations and n-body simulations. The tidal field causes the LMC disk axis to precess and torques disk orbits out of the disk plane, causing a strongly flared, spheroidal-like distribution in the outer Cloud and loss of stars and gas. This interaction leads to an a spatially extended population while roughly preserving the disk-like kinematic signature (i.e., small σ).

The detection of, or strict limits on, the predicted extended distribution would resolve these views and is one of the goals for the present study. Our star count analysis is based on fitting the projected spatial density of several LMC populations among those identified in Chapter 2, based on their location in the color-magnitude diagram (CMD) of the field. The late-type giant populations are dominated by the LMC and may be used as tracers of the spatial structure of the Cloud. Each population is fitted by two models: 1) thin exponential disk and 2) spherical power law model. Our best-fit disk models give the inclination of the LMC to the line of sight $i = 22° - 29°$ and the position angle $\theta = 168° - 173°$, in good agreement with previous estimates. The direction of the LMC disk inclination is also determined. In short, projected 2MASS star counts reproduce the standard LMC values.

The near-infrared 2MASS photometry easily discriminates carbon stars in the color-magnitude diagram. While the 2MASS single-epoch survey of the LMC does not provide variability information, we identified a region of the CMD populated nearly exclusively by carbon-rich AGB stars (Region J), which are also long-period variables (LPVs). This identification is reinforced by recent analyses of MACHO data (Alcock et al. 2000a, Alves et al. 1998a, Wood 1999), although roughly 25% could be binaries (Wood 1999). LPVs obey period-luminosity-color (PLC) relations (e.g., Feast et al. 1989), and based on the PLC relations, the LPVs in a narrow color range ($1.6 < J - K_S < 1.7$) are standard candles with $\sigma_K \approx 0.3^m$. Their photometric dis-

tribution in selected LMC fields has a least three distinct components: a well-defined narrow distribution due to LMC disk and two secondary peaks at fainter and brighter magnitudes. The differential photometric distance to the central disk peak provides a direct determination of the inclination: $42.3° \pm 7.2°$. This value is consistent with but larger than those inferred by deprojecting isopleths. The secondary peak could in principle be due to stellar blends, geometric structure, interstellar reddening, distribution of periods, gradient in age and metallicity, or contaminating population of overtone pulsators in the sample. We examine and discuss the possible origins of this secondary component and conclude that spatial structure is a plausible explanation. Although AGB variability is known to be physically complex and a multimodal explanation can not be ruled out, no available evolutionary models account for the observed signature. This interpretation is bolstered by the good match of the central peak, which includes known fundamental mode pulsators, with the established LMC disk inclination. The distribution of AGB stars suggests the presence of an extended LMC population, which may be as thick as 8 kpc along the line of sight. This would be thicker than the 2.8 kpc flattened spheroid suggested by Hughes et al. (1991) from kinematic data and may be streams of material rather than be smooth and well-mixed. The bright peak is then an intervening population at a distance of roughly 36 kpc and the existence of relatively young carbon-rich AGB stars suggests tidal debris.

3.2 Observations

The LMC field, (4^h00^m to $6^h\ 56^m$ in right ascension, $-78°$ to $-60°$ in declination, J2000.0) has been observed by 2MASS and is included in the most recent data release. Details of the data reduction and sample selection are described above. Figure 3.1 shows both the projected spatial distribution of sources and the color-magnitude diagram of the field. The color-magnitude diagram also shows the location of 12 regions

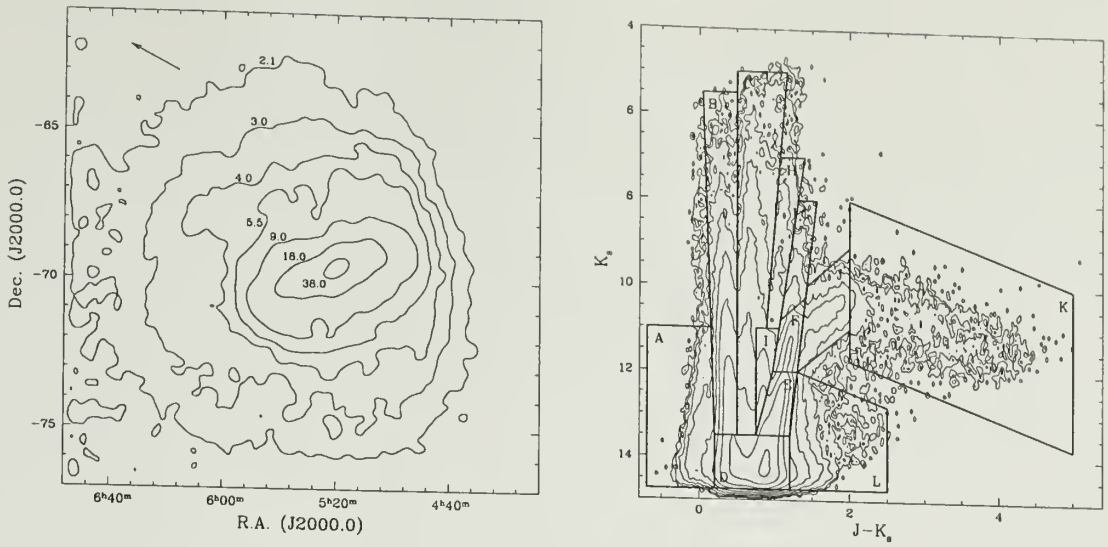

Figure 3.1 *Left panel*: Density distribution of 2MASS sources in the LMC field. Contour levels are labeled in units of 10^3 deg^{-2}. The arrow points in the direction of Galactic center. *Right panel*: CMD of the field showing 12 regions corresponding to major features of the diagram. Contour levels are logarithmic, from 2.0 to 6.0, spaced by 0.5.

analyzed in previous chapter. Total number of sources in our sample is 823,037.

In previous chapter, we examined the populations in selected CMD regions and associated the features with known populations of stars (cf. Table 2.3). Here, we take an in-depth look at the spatial distribution of sources in seven of those regions (Table 3.1) which contain mostly LMC stars. These seven areas of the CMD account for a quarter of all sources in the field.

Table 3.1 Stellar populations of selected CMD regions.

Region	N_{src}	f_{Gal}[a]	LMC populations
A	6,659	0.15	Young O,B,A supergiants, O3—O6 dwarfs
E	166,263	0.05	Low- and intermediate-mass RGB stars, E-AGB stars
F	22,134	0	Oxygen-rich AGB stars, E-AGB and TP-AGB, LPVs
G	1,438	0	Luminous E-AGB stars, O-rich LPVs
H	2,450	0.05	Red supergiants, luminous E-AGB stars
J	8,229	0	Carbon-rich TP-AGB, LPVs
K	2,212	0	Dust-enshrouded C-rich TP-AGB, OH/IR, cocoon stars
Total	209,385		

[a]Fraction of Galactic sources estimated from synthetic model.

The projected spatial density distribution for each of the seven regions is shown in Figure 3.2. Younger populations (Regions A and H) have relatively clumpy distributions which trace the spiral pattern of the LMC (cf. Figure 7 of Schmidt-Kaler 1977). Older stars, on the other hand, have smoother and more extended distributions with significant overdensity in the bar of the Cloud. Several well-known morphological features of the LMC are easily recognizable in Figure 3.2, e.g. 30 Doradus complex (an HII region near $\alpha = 5^h36^m$, $\delta = -69°$) and asymmetric outer loop in the south-eastern part of the LMC, traced by AGB stars.

3.3 Spatial Structure Using Parametric Maximum Likelihood

To quantify the spatial distribution of sources in six selected regions, we perform maximum likelihood (ML) analyses for thin exponential disk and spherical power-law models. The observed source counts for each population are binned in equatorial coordinates, n^o_{ij}, $i = 1, N$; $j = 1, M$. The ML scheme selects a parametric model for which the expected source counts n^e_{ij} most closely match the observed source counts n^o_{ij}. The goodness-of-fit measure,

$$u^2 = \sum_{i,j} \frac{(n^o_{ij} - n^e_{ij})^2}{n^e_{ij}},$$

is asymptotically distributed as χ^2 with $(N \times M - 1 - n_p)$ degrees of freedom, where n_p is the number of free parameters of the model (see below). The expected source counts n^e_{ij} are obtained from the corresponding source density in each bin, ρ^e_{ij}, predicted by the model:

$$n^e_{ij} = \frac{N_{src}\, \rho^e_{ij}}{\sum_{i,j} \rho^e_{ij}}$$

(see Appendix A for details).

The residuals for axisymmetric models show a significant bisymmetric component and, therefore, we have added an LMC LMC bar component in our model fits. The density models with a bar are given by

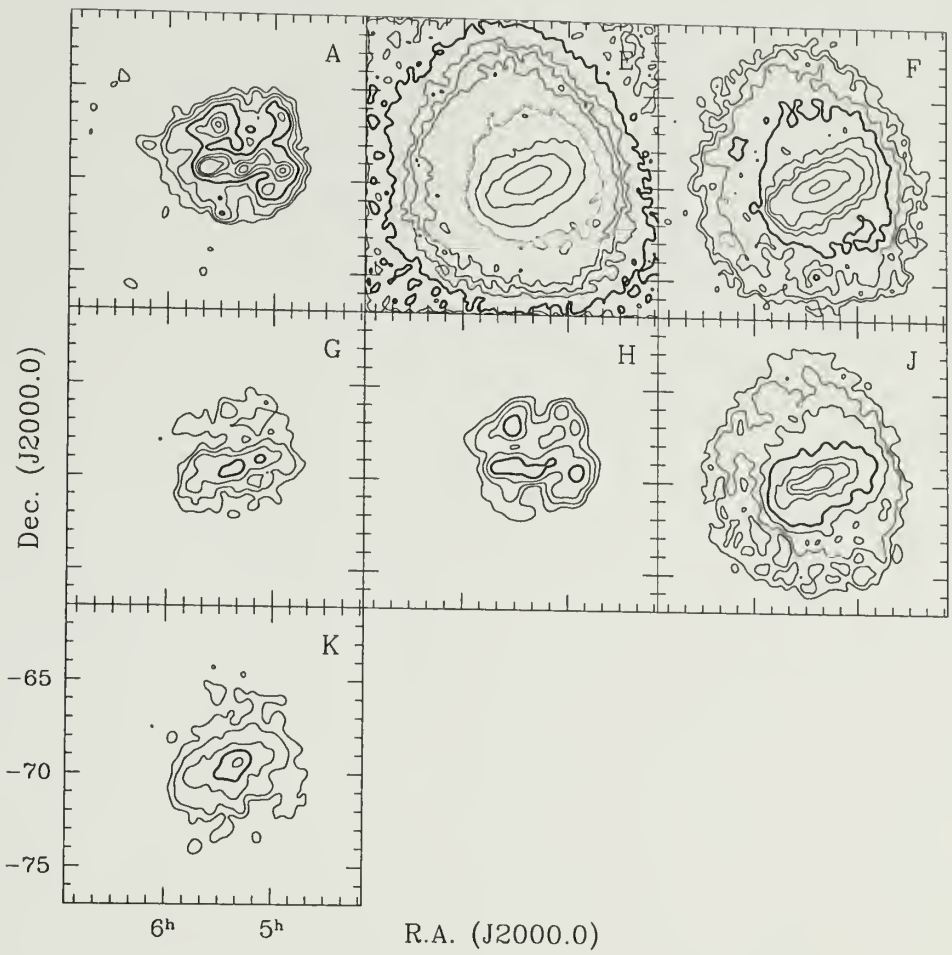

Figure 3.2 Projected spatial density distributions of 2MASS sources in selected CMD regions. The contour levels are 15, 30, 60, 120, 240, 350, 480, 960, 1920, 3840, 7680 deg^{-2}. In panel E the lowest contour level is 60 deg^{-2}. The contour level of 120 deg^{-2} is highlighted for convenience.

$$\rho = \rho_D \exp(-r/R) + \exp(-\Re/a), \tag{3.1}$$

for the 'bar+exponential disk' model, and by

$$\rho = \rho_S r^{-\nu} + \exp(-\Re/a), \tag{3.2}$$

for the 'bar+spherical power law' model. The bar is two-dimensional and has an elliptical shape, $\Re = \sqrt{x^2 + y^2/q^2}$, with the axis ratio q. Both models have 9 free parameters, 7 of which are common to both density representations. The common parameters are the coordinates of the LMC center α_0, δ_0 (J2000.0), inclination i ($0° \leq i \leq 180°$), position angle θ ($0° \leq \theta \leq 360°$), azimuthal angle of the bar ϕ ($-90° \leq \phi \leq +90°$), and scaling constants a and q. In spherical model, i and θ are used to describe the orientation of the bar plane, while in the exponential disk model they are used both for the disk and the bar (the bar is constrained to lie in the disk plane). The remaining two parameters give the relative strength of the axisymmetric component in each case (ρ_D and ρ_S), and the spatial extent of the model (scale length R in the exponential disk model and power-law index ν in the spherical model).

The results of parametric fits are presented in Tables 3.3 and 3.4, along with the corresponding χ^2 values. The best fit parameters in both tables can be grouped by the population age: results for young stars (A, H) and older stars (E, F, J, K) show good agreement among themselves. Sources from Region G form a stand-alone class, with parameters different from the above two groups. The large χ^2/d.o.f. values are due to strong non-axisymmetric components (Figure 3.3). We assume that fitting the non-axisymmetric components would reduce the χ^2 to an acceptable level without strongly affecting the derived global parameters. Therefore, the relative values of χ^2 are interpretable in the relative likelihood sense and we can compare our results with previous work. The AGB populations, Regions G and K, provide acceptable fits with weak asymmetric residuals and admit the possibility of reliable parameters ab initio, especially when a bar is included in the fit.

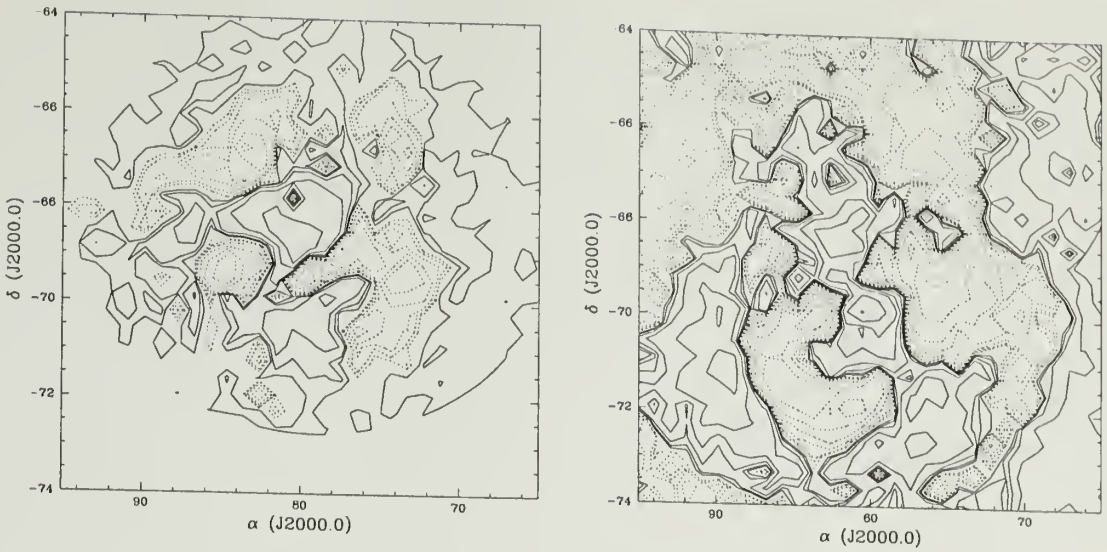

Figure 3.3 Residual plots for exponential disk model with elliptical bar for Regions A (left) and E (right). The dotted contours denote overdensity regions (positive residuals), solid contours are underdensity regions (negative residuals). Both panels show clear non-axisymmetric component consistent with spiral pattern of the LMC; right panel also shows a strong Galactic field gradient.

The distributions of young OB stars and supergiants are clumpy and therefore poorly fitted by a smooth model. The centroid of these populations is $\sim 1°$ to the north of the optical center of the bar (defined by the center of symmetry of the bar, at $\alpha_{2000} = 80.9°$, $\delta_{2000} = -69.8°$), similar to the displacement found by de Vaucouleurs & Freeman (1973). The scale lengths R derived for these populations are noticeably greater than the scale lengths for older populations and reflect the location of the distinct star forming activity. The position angles for these populations are mutually consistent. In the model without bar, the inclination derived from Region A sources, $i = 35°$, is consistent with $i = 38.2°$ found from the distribution of HI regions (Feitzinger et al. 1977), and also with $i = 36^{+2}_{-5}$ degrees found from Monte Carlo simulations of ultraviolet photopolarimetric maps of the western LMC (Cole et al. 1999).

The older populations (M giants, AGB stars and LPVs) are well-represented by a smooth density law. The centroids for these populations are within 0.4° of each other

on the sky and are close to the optical center of the bar. Average scale length for these populations is $R = 1.42 \pm 0.01$ kpc (without bar), in agreement with $R = 1.46$ kpc (Bothun & Thompson 1988), and $R = 2.15 \pm 0.01$ kpc (with bar). Note that Region E sources have the scale length, $R = 1.58$ kpc, significantly higher than other old populations, $R \sim 1.4$ kpc, and similar to MACHO result $R = 1.6$ kpc derived from RR Lyrae (Alcock et al. 2000a). Figure 3.4 shows the deprojected density of Region E sources as the function of LMC radius for models with and without bar. The likely reason for the increase in the scale length is the substantial population of Galactic foreground M dwarfs at deprojected radii $r \gtrsim 8$ kpc, which is also suggested by the large-scale approximately linear gradient in Figure 3.3. The density plots for other old populations (not shown) show evidence for disk truncation near $r_t \sim 3$ kpc, similar to $r_t = 2.41$ kpc found by Bothun & Thompson (1988). The inferred inclinations

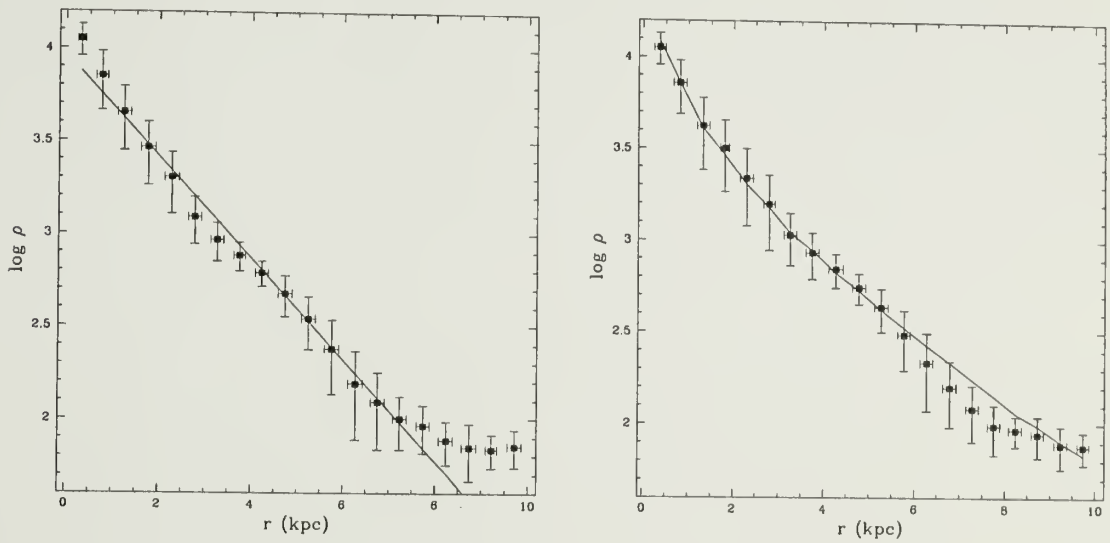

Figure 3.4 Projected density of Region E sources as the function of LMC radius. The fits are shown for model without bar (left) and with elliptical bar included (right). Note the Galactic foreground at $r \gtrsim 8$ kpc.

are in the range $i \sim 22° - 29°$. The variance weighted average for inclination is $i = 24.0° \pm 0.3°$, in good agreement with previous determinations from star counts (de Vaucouleurs 1955), $i = (25 \pm 5)°$, distribution of star clusters, $i = (25 \pm 9)°$ or

HI isophotes, $i = (27 \pm 5)^\circ$ (McGee & Milton 1966), or photographic R isophotes (de Vaucouleurs 1957), $i = (27 \pm 2)^\circ$. The inclination values derived from bar models are in agreement with each other and higher by $\sim 15^\circ$. Their weighted average is $i = 38.2^\circ \pm 0.4^\circ$. The deprojection-based position angles for the group are mutually consistent, $\theta \sim 168^\circ - 173^\circ$, and fall in the range $\theta = 160^\circ - 180^\circ$ derived from surface photometry of the LMC by others (see, e.g. Table 2 of Schmidt-Kaler & Gochermann 1992). Position angles for bar models vary from 12° to 17°.

The extended spatial coverage of the LMC field by 2MASS allows one to determine the absolute direction of the inclination, i.e. to determine the closest side of the LMC. To illustrate this point, we make two different test models of an exponential disk with $\{\alpha_0, \delta_0, R, i, \theta\} = \{80^\circ, -70^\circ, 1.5, \pm 30^\circ, 135^\circ\}$. Both disks are modeled with 3,000 point sources. The restored density contours are presented in Figure 3.5. The difference in the expected source counts is clearly seen in the outer regions. This suggests that for relatively spatially extended populations both the absolute value and the direction of the inclination can be reliably determined. On the other hand, if a population is relatively compact in the sky, the inferred direction of inclination may differ from the actual value (cf. Table 3.3). Based on the results for older populations, we see that the nearest side of the LMC is its eastern side, in agreement with previous results based on photometry of Cepheids in the Cloud (de Vaucouleurs 1955, Gascoigne & Shobbrook 1978, Laney & Stobie 1986). Restricting our attention to Region J, which has little if any Galactic contamination, we can effectively eliminate any gradient caused by the Galactic foreground.

The results of fits to a spherical power-law profile are described in Table 3.4. There are no significant difference between power-law exponents for various populations: all values are ≈ 2.5. The centroid shift for younger populations, present in Table 3.3, is seen here as well. The underlying distribution, a disk and spheroid together, is described here as a single profile. A power-law disk profile, of course, will have an

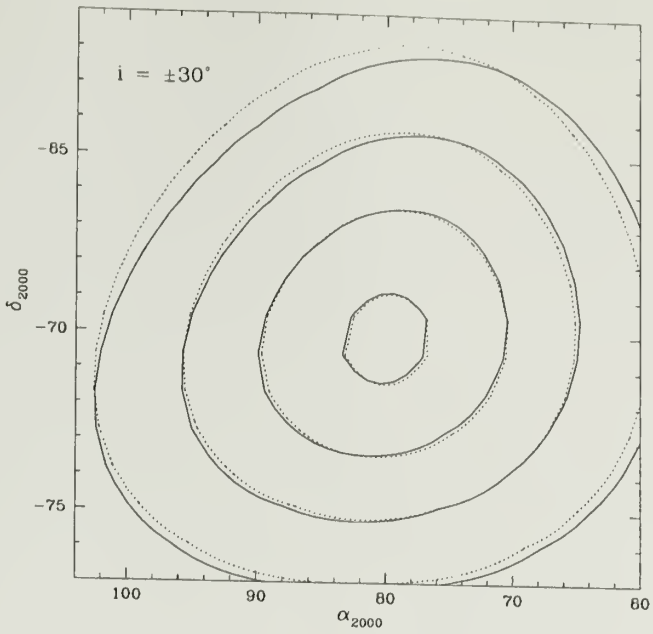

Figure 3.5 Isodensity contours of test models showing the sensitivity to the direction of inclination. Each test model is represented by 3000 sources distributed according to an exponential disk with $\{\alpha_0, \delta_0, R, i, \theta\} = \{80°, -70°, 1.5, \pm 30°, 135°\}$. Four logarithmically spaced density levels of 0.0003, 0.001, 0.003, 0.01 deg^{-2} are shown. Solid line shows model with $i = -30°$, dotted line — model with $i = +30°$. The difference is clearly seen, especially in outer contours.

index $1+\nu$, where ν is the index for the spherical profile, and therefore some unknown combination of a disk and spheroid makes interpretation difficult. We note that these fits are worse than the exponential fits and probably do not bear on the reality of a spheroidal population. An independent test for a spatially extended population is described below (§3.4.2).

We compared the results of our fits to those by Hughes et al. (1991), who modeled the distribution of intermediate and old long-period variables (ILPV and OLPV, respectively) with exponential disk and power law models. They derived $\nu = 1.8 \pm 0.1$ and $R = 1.6 \pm 0.2$ from 63 OLPVs, and $\nu = 1.7 \pm 0.1$ and $R = 1.7 \pm 0.2$ from 81 ILPVs in their sample. Our analysis for $\sim 200,000$ 2MASS sources of similar populations (Regions E, F, G, and J) gives $\nu \sim 2.5$ and $R \approx 1.4$ kpc. We note that the scale lengths

R are in agreement, while the best-fit power law exponents differ. We attribute this difference to the increased source counts at the periphery of the LMC, in the regions of greatest sensitivity of power-law models.

To summarize, the projected distribution of LMC populations observed by 2MASS is consistent with previous studies. We found the scale length of the LMC disk, $R \sim 1.4$ kpc, the inclination angle, $i \sim 22° - 29°$, and the direction of the LMC tilt in good agreement with existing estimates.

3.4 Standard Candle Analysis

We complement our previous analysis (§3.3) by incorporating photometric distances in addition to our CMD selection. Below, we describe the selection of standard candles, the details of the analysis, and the implications for the structure of the LMC derived from 2MASS photometry.

3.4.1 Selecting Standard Candles from 2MASS Data

Good standard candles for this purpose satisfy three conditions: 1) they must be luminous and easily identified; 2) they must be sufficiently numerous and representative of the underlying structure, and 3) they must have small photometric dispersion as a class (that is, small σ_M). In previous chapter, we argued that stars in Region J of the 2MASS CMD are potentially good standard candles. Being brighter and redder than the RGB tip, most of these stars are carbon-rich thermally-pulsating AGB stars (TP-AGB). Recent data (Alves et al. 1998a, Wood 1999) suggest that most of these stars are Miras or semi-regular variables (SR)[1]. The fraction of variables in this region is close to 100%, although roughly 25% could be binaries (Wood 1999). Here, *we will assume that all sources in Region J are carbon-rich long-period variables.* Their red colors effectively discriminate against the population of oxygen-rich LPVs, since the

[1]As follows from the analysis of period-luminosity relations of MACHO variables (Wood 2000), the majority of these stars are SRs.

latter rarely have $J - K_s > 1.5$ (Hughes & Wood 1990). As long-period variables, these stars follow a linear PLC relation (e.g. Feast et al. 1989). The luminosity of these stars can be characterized by their periods or near-infrared colors, and therefore, these stars can be used to probe the structure of the LMC along the line of sight. In the absence of the period data, we cannot use standard period-luminosity or period-color relations to calibrate the intrinsic brightness of these variables. Rather, we have to rely on luminosity-color (LC) relation. However, since the sources in Region J are a mixture of SRs and Miras, we must address the question of whether applying the same LC relation to Miras and SRs is justified. The period-luminosity diagram from MACHO data (Figure 1 of Wood 2000) identifies 5 distinct sequences of variables. The sequence of classic Miras (C) also hosts many SR variables, called type "a" semi-regulars, or SRa. The distinction between Miras and SRas, based on the amplitude of visible pulsations (SRas have smaller amplitudes, $V < 1.5$ mag), may be artificial; some authors (Kerschbaum & Hron 1994) argue that SRa is not a distinct class of variables but a mixture of Miras and SRb (semi-regulars of type "b") variables. Since these SRas lie on Mira sequence, they follow the same PL relation as Miras. To check whether they follow the same LC relation, we separately perform linear regression for Miras and SRas selected from the sample of Hughes & Wood (1990). The resulting LC relations for $J - K_s < 2.0$ are:

$$K_s = (-0.96 \pm 0.17)\,(J - K_s) + (12.52 \pm 0.28), \qquad \sigma = 0.33$$

$$K_s = (-0.90 \pm 0.21)\,(J - K_s) + (12.24 \pm 0.35), \qquad \sigma = 0.31$$

Since the relations are consistent with each other, we justify using the same LC relations for Miras and SRas on sequence C. The same Figure shows SR sequence (B), which runs parallel to Mira sequence and includes many sufficiently red stars ($J - K > 1.4$) to enter our region J. These stars are in a higher-order pulsation mode and seem more numerous than C-rich Miras and SRas. If follow different LC relation, they may seriously hinder the quality of standard candles. Below (see §3.5.2), we

demonstrate that these overtone pulsators *do not affect* our analysis and hence we will consider that all C-rich LPVs in Region J follow the same LC relation.

The 2MASS sample of C-rich LPVs in the LMC contains 8229 stars. The surface map of Region J is shown in Figure 3.6. The luminosity-color relation for these stars results in the well-defined ridge in the figure. In Figure 3.7, we plot the sample of 79 oxygen- and carbon-rich Miras in the LMC (Glass et al. 1990) on top of 2MASS color-magnitude digram. Magnitude and color of each Mira are averaged over period. The luminosity-color relation (shown with the solid line) for 14 carbon Miras in the color interval bounded by vertical dashed lines is

$$< K_s >= (-0.99 \pm 0.80) < J - K_s > +(12.36 \pm 1.33), \qquad \sigma = 0.38.$$

The average r.m.s is $\sigma \lesssim 0.3^m$ for $1.4 < J - K_s < 1.7$. Given this LC relation, we may argue that selecting LPVs from a reasonably narrow color range will result in sources with similar luminosities, i.e., standard candles. For our analysis, we choose color interval $1.6 < J - K_s < 1.7$, sufficiently narrow to ensure similar luminosities of our standard candles and sufficiently broad to host enough sources (1385) for statistically meaningful inference.

Finally, we must address the issue of random phase observations. The ridge-line fit above was based on the *average* LC relation. Given single-epoch 2MASS data, we may expect significant broadening of the LC relation due to random phase observations. From analysis of light curves in Glass et al. (1990), the amplitudes of carbon-rich LPVs are $\Delta K \lesssim 0.5$ mag. However, Miras constitute only a modest part of our sample. The majority of variables in Region J are SRas and have much smaller amplitudes ΔK. As such, the impact of random phase observations will be less noticeable. In fact, as we will demonstrate below (§3.5), the width of main peak in the apparent luminosity function is only $\sigma \approx 0.2^m$. This suggests that using the phase-average LC relation for random phase data is appropriate.

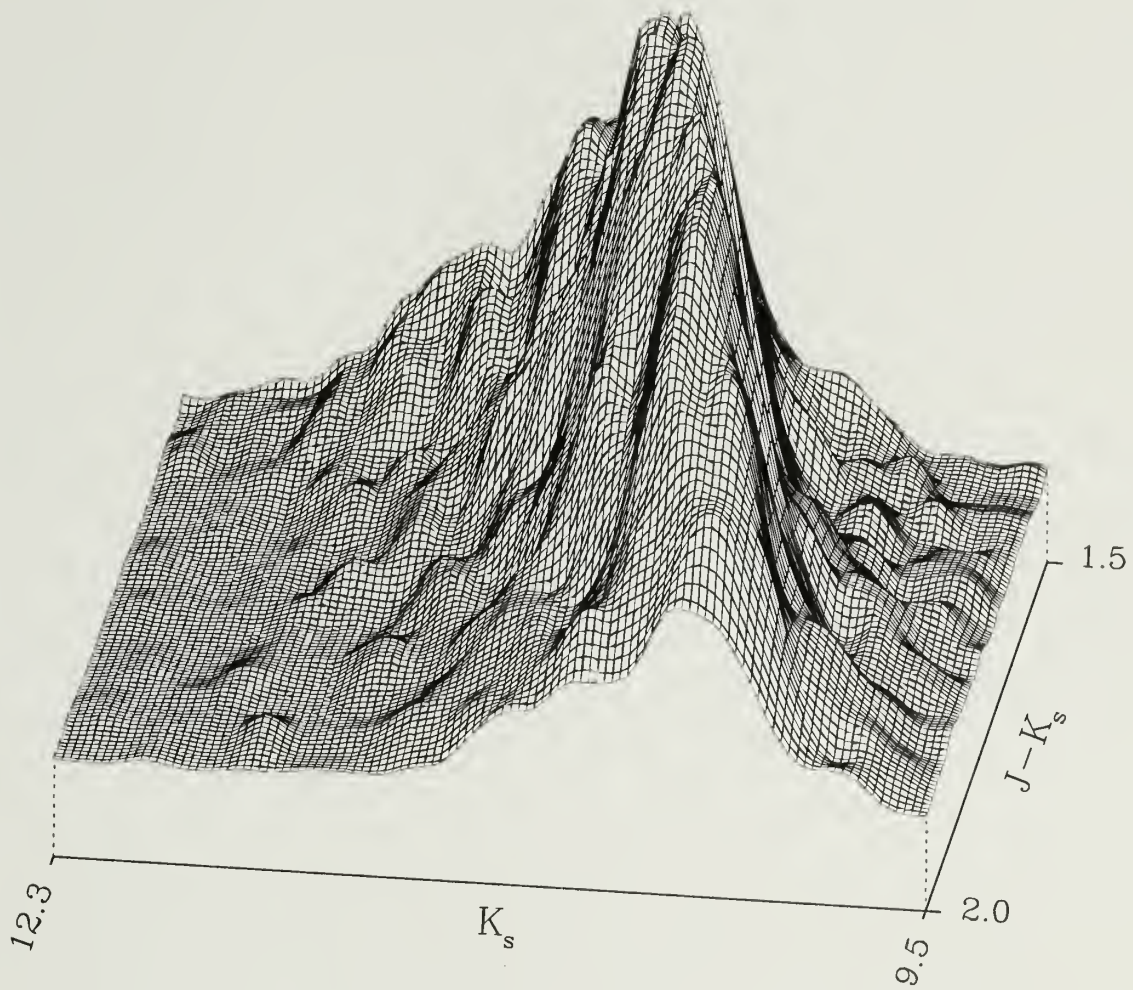

Figure 3.6 Density map of CMD Region J. The surface map covers color range from $J - K_s = 1.5$ to $J - K_s = 2.0$. Note the well-defined ridge, which suggests a luminosity-color relation for these stars.

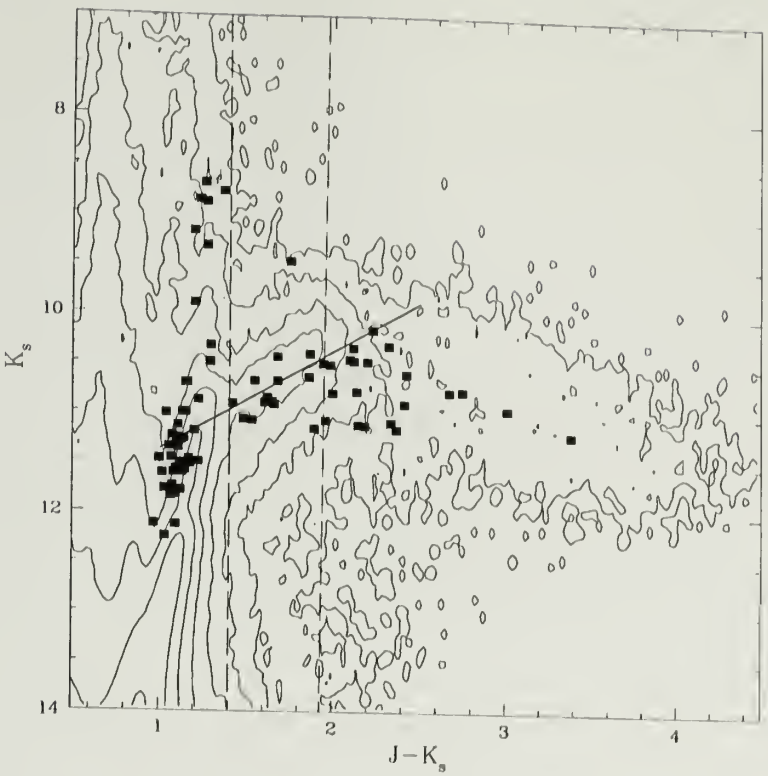

Figure 3.7 The sample of 79 oxygen- and carbon-rich Miras from Glass et al. (1990), plotted over the color-magnitude diagram of 2MASS. Magnitude and color of each Mira are converted to CIT photometric system and averaged over the period. Vertical dashed lines show the color range, $1.4 < J - K_s < 1.9$, used for the straight line fit to luminosity-color relation. The best-fit LC relation is indicated with thick solid line.

3.4.2 Method

Without prior knowledge of the true source distribution, which is likely to be irregular due to tidal interaction (e.g. Weinberg 2000) or sufficient characterization of the stellar populations to allow a non-parametric density estimation with all of the data, we study the photometric distribution in several fields in the LMC. We select reasonably small-sized fields to suppress the inclination effect inside the fields (the stars within a field may be considered at the same distance). This should produce a well-defined centroid in the apparent brightness distribution, corresponding to the average distance to the disk plane. The fields are located along two great circle arcs

passing through the central region of the Cloud: Arc 1, parallel to the line of nodes, and Arc 2, perpendicular to the line of nodes (see Fig. 3.8). The arcs correspond to major and minor axes of the inclined LMC disk and were chosen for enhancing and contrasting the inclination effect.

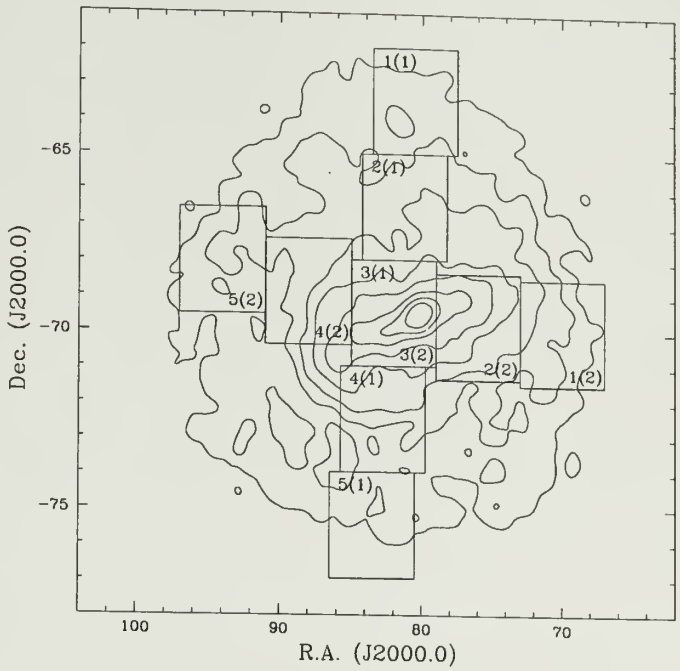

Figure 3.8 Locations of selected LMC fields. Field positions follow two arcs: Arc 1 (North-South direction, parallel to the line of nodes), and Arc 2 (East-West direction, perpendicular to the line of nodes). Field numbers are indicated, with arc numbers given in parentheses. Field 3 is the same for both arcs.

The apparent luminosity function can be analyzed in terms of the centroid $\overline{m}$ and the width $2\sigma_m$ of the distribution. For a homogeneous standard candle population, the centroid of the distribution measures LMC distance and the width of the distribution gives an estimate of its line-of-sight depth. An error propagation analysis of the apparent magnitude-absolute magnitude-distance relation gives

$$\sigma_m^2 \approx \sigma_M^2 + \frac{4.72}{R_{LMC}^2}\sigma_r^2 + \sigma_A^2 + \sigma_{ph}^2, \tag{3.3}$$

where $R_{LMC} = 50$ kpc is the average distance to the LMC, σ_M is the intrinsic precision of our standard candles, σ_A is the variance due to extinction, σ_r is the geometric depth,

and σ_{ph} is the photometric error. Equation (3.3) states that the apparent brightness distribution is the convolution of the spatial density and the intrinsic luminosity function and therefore provides an *upper limit* to the geometrical depth.

3.5 Results and Interpretation

The brightness distributions of standard candles in selected fields are shown in Figures 3.9 and 3.10. All fields in Figures 3.9 and 3.10 exhibit well-defined central

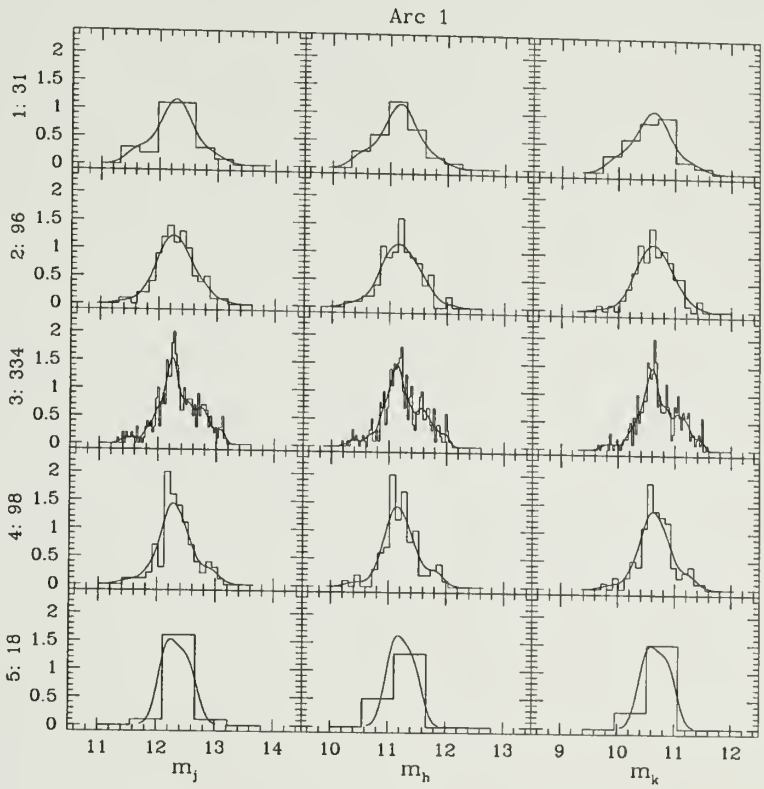

Figure 3.9 Apparent brightness distribution of selected C-rich Miras in fields along Arc 1. Histograms are normalized raw data, smooth curves are kernel smoothed densities. The bin widths in each histogram are chosen to ensure signal-to-noise ratio of 3 or better. Columns correspond to J, H, K_s bands, rows correspond to fields. Fields and the numbers of C-rich LPVs in the fields are labeled. See Figure 3.8 for field designations.

peaks corresponding to the midplane of the LMC disk. We immediately notice that the narrowest features in the brightness distributions have widths $\sigma_m \approx 0.2^m$ (cf.

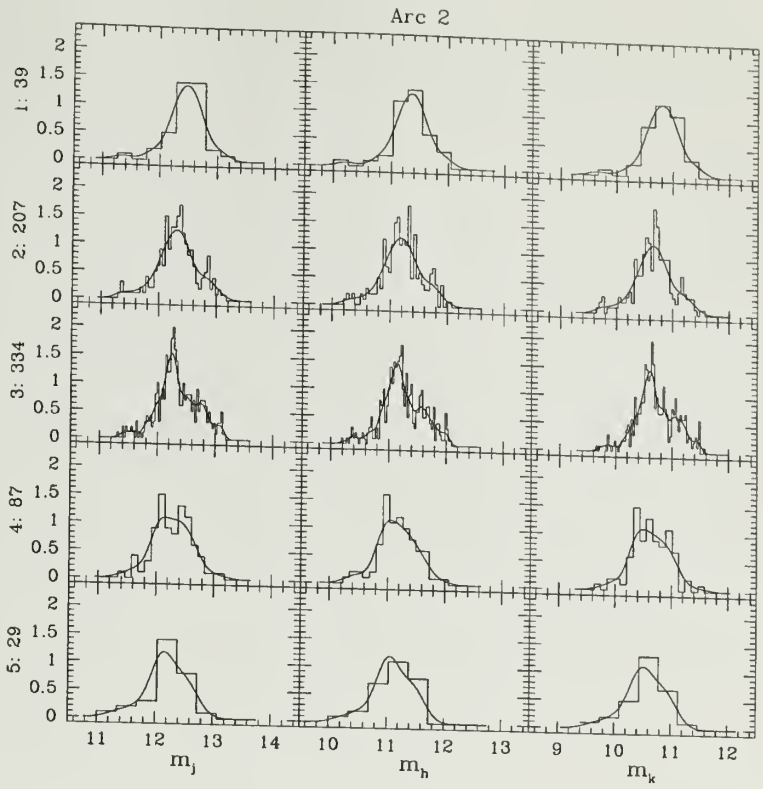

Figure 3.10 Apparent brightness distribution of selected C-rich Miras in fields along Arc 2.

Field 3). This is a *direct evidence* that our color-selected sources are standard candles at least as good as $\sigma_M \approx 0.2^m$. In fact, they are even better, because of the additional terms on the right-hand-side in equation (3.3). This suggests that carbon LPVs in the narrow (~ 0.1 mag) color range are excellent standard candles, even observed at random phases.

3.5.1 Analysis of the Distribution Centroids

The centroids of the distributions are consistent with the inclination of the LMC derived in §3.3. Since Arc 1 is parallel to the line of nodes, the stars in the fields along this arc should be roughly at the same distance. Hence, we do not expect any drift in the means $\overline{m}$ for stars in these fields. On the other hand, we expect a shift in the mean magnitude for fields along Arc 2, which is perpendicular to the line of nodes.

Assuming the Eastern part of the Cloud is closer to us, sources in Eastern fields should be, on average, brighter than their counterparts in Western fields. Figures 3.9 and 3.10 confirm the expectations. The magnitude of the effect is shown in Figure 3.11 for both arcs as the function of the angular distance from the optical center of the bar. To improve the signal-to-noise ratio, we take the average $\overline{m}$ of the mean magnitudes

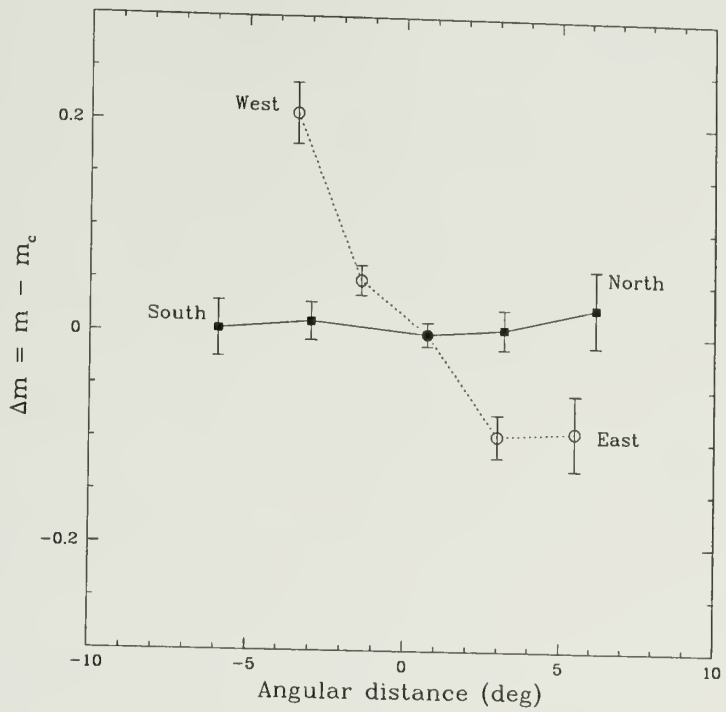

Figure 3.11 The mean magnitude offset averaged over J, H, K_s bands as the function of the angular distance from the optical center of the bar. The offsets are given relative to the central fields of the corresponding arcs.

in three bands and plot the resulting averages normalized to the central field of the respective arc. We find that fields along the North-South line have similar mean magnitude, whereas Eastern fields are on average 0.1^m brighter and Western fields are $\sim 0.2^m$ fainter than central bar fields. The magnitude difference is similar to what Caldwell & Coulson (1986) found in their analysis of Cepheids in the Cloud.

Data shown in Figure 3.11 allow independent determination of the LMC inclination angle. We provide results of two methods: (1) the inclination of the best fit

plane to the photometric distance estimate for each field; and (2) the mean inclination of each field paired with the central field. In Method 1, we compute the best fit line through spatial positions of the field centers. The estimates for each arc are $0.9° \pm 0.3°$ and $42.3° \pm 7.2°$, respectively. We observe that the inclinations along our Arc 1, as expected, are consistent with zero, while the inclination angles along Arc 2 are consistent with values in Table 3.3 at 2σ level. Alternatively, the LMC disk may be warped and therefore not coplanar. Method 2 does not presuppose a tilted plane but rather computes the inclination of each field relative to the line of sight through the central field. We then compute the weighted average over all pairs. The resulting inclinations are $1.0° \pm 4.1°$ and $34.4° \pm 2.7°$ for the first and second arcs, respectively.

In principle, this magnitude drift could have been produced by a reddening gradient across the Cloud. However, the extinction maps by Oestreicher & Schmidt-Kaler (1996) do not show any systematic change in reddening in the West-East direction across the LMC. In addition, an analysis of the extinction across the entire cloud based on the location of the giant branch reveals little evidence for significant extinction on average outside of the inner square degree (see Chapter 2). Moreover, if the magnitude drift were indeed due to reddening gradient, it would have had band-dependent signature. The ratios of magnitude offset in J, H, K_s bands would be in direct proportion to the extinction coefficients A_J, A_H, A_K. Since this is not the case, we have to reject this possibility and interpret the drift as the true distance effect.

3.5.2 The Shape of the Distributions

Careful study of the density distributions in Figures 3.9 and 3.10 shows that some distributions have extended tails. For example, distributions in Fields 3 and 4 clearly show positive skewness. Figure 3.6 also shows the extension of the central ridge toward fainter magnitudes. To quantify the shape of the distributions, we first enhance the S/N ratio of the data by combining five fields along Arc 1 and three

photometric bands[2] into single dataset. Then, we fit the resulting sample of 1719 stars with multiple Gaussians:

$$P(\Delta m) = C \sum_{i=1}^{N} \frac{a_n}{\sigma_n \sqrt{2\pi}} \exp\left[-(\Delta m - \overline{\Delta m_n})^2 / 2\sigma_n^2\right], \tag{3.4}$$

where N is the number of Gaussians in the fit, Δm is the magnitude offset and C is the normalization constant. The free parameters are adjusted to maximize the log-likelihood function:

$$\log L = \sum_{j=1}^{1719} \log P(\Delta m_j). \tag{3.5}$$

The results for multiple Gaussian fits are presented in Table 3.2 and Figure 3.12.

Table 3.2 Gaussian fits of the apparent luminosity function of carbon stars in the LMC.

N (number of Gaussians)	a_n	$\overline{\Delta m_n}$	σ_n	$\Delta \log L^{a}$
1	1.00	0.11 ± 0.01	0.35 ± 0.01	0.0
2	0.24	0.01 ± 0.02	0.12 ± 0.02	39.8
	0.76	0.14 ± 0.02	0.39 ± 0.02	
3	0.05	-0.66 ± 0.06	0.14 ± 0.04	52.3
	0.20	0.58 ± 0.07	0.19 ± 0.03	
	0.75	0.03 ± 0.02	0.22 ± 0.02	
4	0.15	0.62 ± 0.08	0.18 ± 0.04	56.3
	0.75	0.05 ± 0.03	0.25 ± 0.04	
	0.06	0.01 ± 0.03	0.06 ± 0.04	
	0.04	-0.70 ± 0.05	0.12 ± 0.03	
4[b]	0.71	0.03 ± 0.02	0.24 ± 0.02	55.7
	0.06	0.03	0.06 ± 0.03	
	0.19	0.58 ± 0.06	0.20 ± 0.03	
	0.04	-0.69 ± 0.05	0.13 ± 0.03	

[a] The difference between log-likelihood values relative to single Gaussian model.
[b] Constrained model, $\overline{\Delta}m_1 = \overline{\Delta}m_2$.

Using generalized likelihood ratio test, we compare the significance of derived fits. For example, double Gaussian representation provides an improvement of $\Delta\chi^2 = 2\Delta \log L = 80$ for three additional degrees of freedom, which suggests statistical significance $1 - 10^{-16.5}$. Thus, single Gaussian model must be rejected based on observed

[2]We offset each band data so that the peak corresponds to zeroth magnitude.

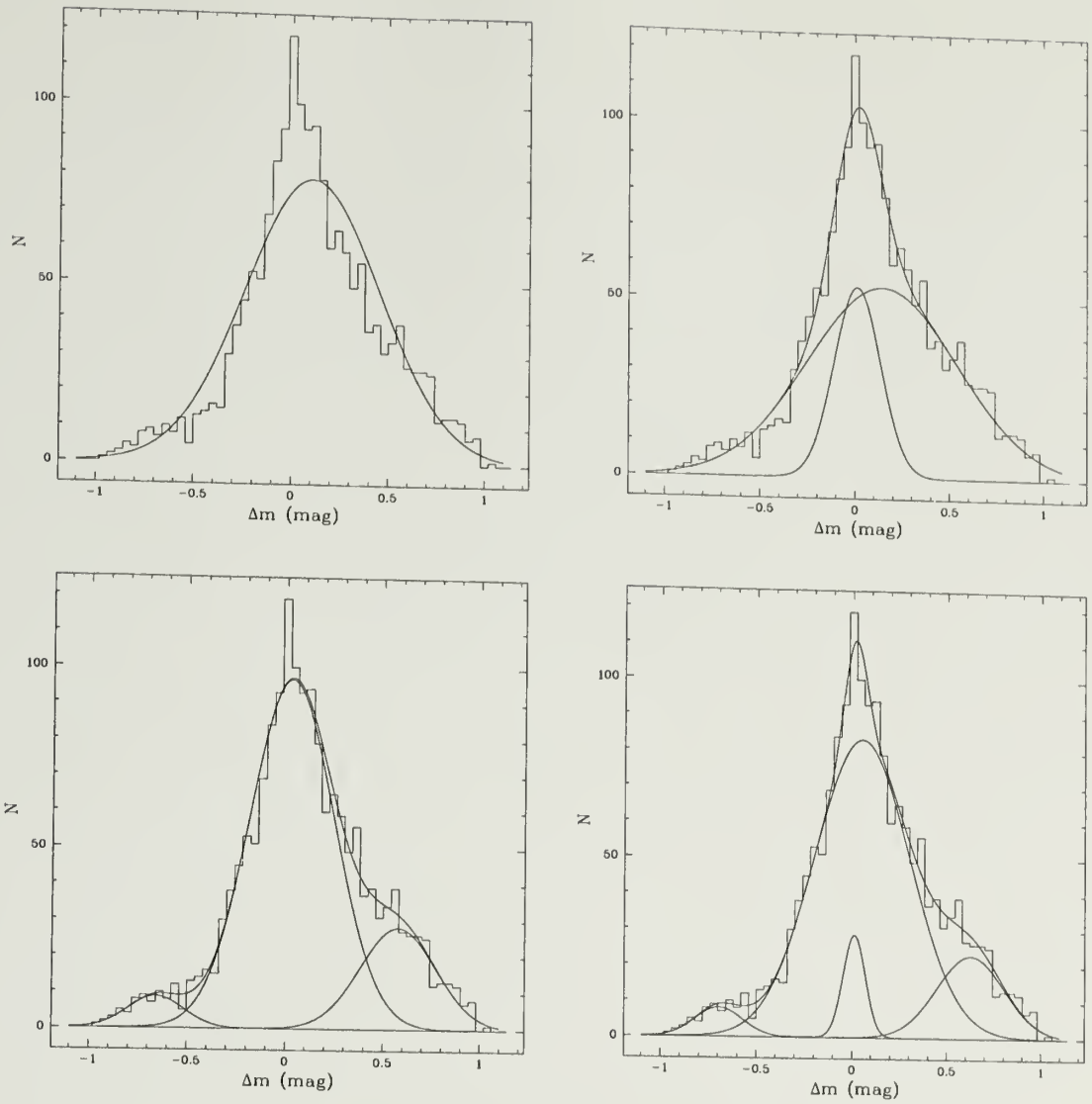

Figure 3.12 Gaussian components of the apparent luminosity function.

distribution. The improvement of triple Gaussian model over the double Gaussian solution is $\Delta\chi^2 = 23$ for three additional degrees of freedom. The statistical significance of this result is $1 - 1.5 \times 10^{-5}$, which suggests that triple Gaussian fit must be favored over double Gaussian representation. Similar, four Gaussian model is preferred over triple Gaussian with statistical significance 0.95. This is relatively strong evidence for yet additional component in the observed distribution. However, the fourth peak in Figure 3.12 is coincident with the main central peak. A possible explanation for

this is that we are seeing two disk populations, located at the same distance: younger disk ($t \lesssim 1$ Gyr) with small exponential scale height along the line of sight, and intermediate-age disk with larger velocity dispersion and greater scale height. Such an interpretation should be directly verifiable from kinematics of Region J stars, provided a large enough sample of velocities for these stars exists. Accepting the two-disk interpretation, the ratio of young/intermediate carbon-rich stars in the LMC disk is estimated from the areas under the two curves: $f(\text{young/old}) \sim 0.06/0.75 \sim 0.08$. In Table 3.2 we also provide the result for constrained four Gaussian model, where we impose a physically plausible condition $\overline{\Delta}m_1 = \overline{\Delta}m_2$.

In the discussion above, we used asymptotic behavior of likelihood ratio to test hypotheses about the LMC structure. Real structure of the LMC may be (and probably is) more complex than our crude representations and may involve a whole spectrum of vertical scale heights rather than just one or two characteristic values. Nevertheless, in further discussion, we will assume the three-component mixture as the true representation of the LMC structure. We interpret the central peak as the midplane of the LMC disk, which hosts 75% of all sources and has width $\sigma \approx 0.2^m$. The extended distribution consists of two distinct components: the stronger one with 20% of the sources, approximately 0.6^m fainter than the main peak; and the weaker one (5%) with the centroid 0.7^m brighter than the main peak.

Among the factors which could produce the extended component visible in Figures 3.9 and 3.10 are: 1) foreground population, 2) source blending, 3) interstellar reddening, 4) population of overtone pulsators, 5) distribution of periods, 6) age/metallicity variations, and 7) spatial density distribution[3]. Foreground population can be rejected because the fraction of Galactic sources in Region J is nearly zero (see Table 3.1). Interstellar reddening would produce a band-dependent effect

[3]Our sample consists of S/N ten or better detections in J, H, and K so spurious sources are unlikely.

(i.e. longer tails in J band than in K_s band). We consider each of the remaining five possibilities in detail:

1. *Source blending.* Considering that the secondary peak runs parallel to the main LC relation (cf. Figure 3.6), at least one member in the blend must be a carbon star. However, blending a carbon star with an unresolved source would produce a source brighter than the carbon star. This means the secondary peak would be brighter than the main feature, which contradicts to data;

2. *Population of overtone pulsators.* The pulsation mode of Mira variables seem to have been resolved recently with Miras unambiguously identified as fundamental mode pulsators (Wood & Sebo 1996, Wood et al. 1998). It is conceivable, then, that our color-selected sample of standard candles includes a population of first- and higher-overtone LPVs. Based on Figures 3.9 and 3.10, this 'secondary' population should constitute about 20% of the entire sample, and be fainter by $\sim 0.6^m$. We test this possibility by cross-correlating 2MASS data with the subsample of fundamental-mode LPVs from Hughes & Wood (1990). After the magnitudes of matched sources are corrected for the LMC inclination, we found only 16 are in the color interval $1.6 < J - K_s < 1.7$, which is not sufficient for statistical inference. To boost the S/N ratio, we project all sources with $J - K_s < 2$ along the LC regression line to bring them to the same color interval. This increases the sample to 91 stars. The resulting histogram of K_s magnitude is shown in Figure 3.13, where we also plot the histogram of our 1719 sources normalized to the same area. The KS-test of the two distributions gives probability $P = 0.257$, which is not sufficient to reject the null hypothesis that the two samples are drawn from the same distribution. The histogram reveals the same extended component, approximately 0.6 mag fainter than the main peak. Since the feature is present even in the data without overtone pulsators, this explanation can not be favored. Following the referee's suggestion, we

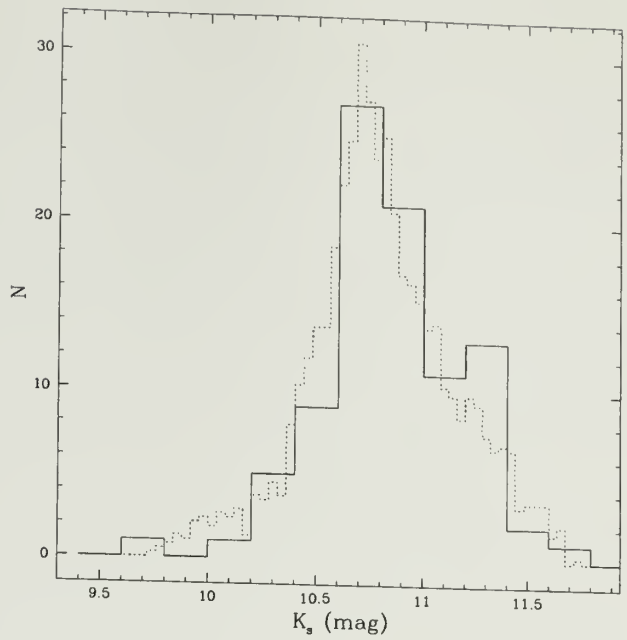

Figure 3.13 The histogram of K_s magnitudes of fundamental-mode pulsators from Hughes & Wood (1990). The magnitudes were projected along the mean LC regression line to bring stars to the same color interval. Dashed line shows the histogram of 1719 sources from our sample, normalized to the same area.

have also looked at underluminous carbon-rich variables found by Bergeat et al. (1998) as possible candidates for secondary population. The location of these variables in the PL-plane identifies them as MACHO variables on sequence D (see Wood 2000). The nature of these pulsators with a long secondary period (LSP) is still unknown, but two seemingly plausible reasons for LSPs are binarity or strange pulsation mode (Wood 2000). Whatever the mechanism, the number of red variables in this sequence is simply not sufficient to explain the observed secondary peak. There are only three MACHO variables with $J - K_s > 1.4$ among more than a hundred on sequence D, and only eight of approximately 600 stars in the sample of Bergeat et al. (1998) while the observed fraction in the fainter peak is 20%. Thus, even though the magnitude offset for these variables is consistent with the observed secondary peak, their small number is a main reason why we reject this explanation.

3. *Distribution of periods.* Even in the case of a zero-dispersion PLC relation for C-rich LPVs, the observed magnitude distribution could result from an intrinsic period distribution (in addition to overtone pulsations discussed above). Although this explanation remains a possibility because the physics of these stars remains uncertain in detail, such an effect is not apparent in current theoretical models, which confirms an intrinsic width of the instability strip but not multiple peaks. Conversely, as previously mentioned, the good fit of the primary peak to the disk inclination gives us confidence in a well-defined instability strip and width of this peak is consistent with other pulsators.

4. *Age-Metallicity Variations.* Alternatively, the pulsation periods depend on mass and metallicity and distribution of periods implies the range of mass, ages and metallicities, and vice versa. Assuming a range of initial AGB masses leads to the range of intrinsic bolometric magnitudes for a single period (Marigo et al. 1996). Marigo's et al. theoretical evolutionary tracks show the difference in a few tenths of a magnitude for carbon Miras at a constant period, depending on the mass of the star. Fitting the apparent luminosity function to these tracks (Cole 2000) suggests that the stronger peak may be due to younger ($\sim$ 0.6 Gyr) and more massive stars ($2M_{\odot}$), while the broader component is formed by older ($\sim$ 2.8 Gyr) and less massive ($\sim 1.2M_{\odot}$) stars. This appears consistent with observations: Frogel et al. (1990) found that carbon stars are present in globular clusters aged 100 Myr to about 3 Gyr and that carbon stars in intermediate-age LMC clusters are a few tenths of a magnitude fainter than those in young LMC clusters. Alves et al. (1998) reported that AGB variables in the intermediate age cluster NGC 1783 are about 0.5 mag brighter at given period than variables in ancient LMC globular cluster NGC 1898. We find two aspects of this possibility to be unsatisfying. First, it does not naturally explain

the bright secondary peak. Second, the star formation rate subsequent to the 2.8 Gyr burst would have to be small in order to result in a well-defined feature;

5. *Extended density distribution in the LMC.* This appears to be the most natural explanation to the observed brightness distributions: it is band-independent, it does not rely on a special star formation history, and straightforwardly explains both the brighter and fainter secondary distribution. The distinct feature at fainter magnitudes may be associated with the population kinematically distinct from the disk sources, recently found by Graff *et al.* (1999). To strengthen the case, we note the similarity of the source fractions in primary/secondary components in their work (80/20) and in ours (75/25). This motivates a detailed kinematic follow-up of the small bright "clump" in the photometric distribution. Based on the offset, this population is 14 kpc from the LMC center and coincident with the intervening population detected by Zaritsky & Lin (1997). The existence of LPVs implies a relatively young population, and the broad area is consistent with tidally stripped material. A future detailed study will attempt to self-consistently model the disk, an extended spheroid component as suggested by Hughes et al. (1991), and test for other distinct features. Figure 3.12 allows rough estimate of the thickness of the LMC disk/spheroid. Using equation (3.3) on the central peak ($\sigma_m = 0.22$), and taking $\sigma_{ph} = 0.04^m$, $\sigma_A = 0.05^m$, and $R_{LMC} = 50$ kpc, we derive half-thickness $\sigma_r \sim 4.3$ kpc for $\sigma_M = 0.1$, or $\sigma_r \sim 1.5$ kpc for $\sigma_M = 0.2$. The uncertainty of the LC relation is the limiting factor in estimating the thickness of the LMC along the line of sight, and future studies using full PLC relation, rather than LC relation (e.g., using MACHO data) can prove useful in reducing the uncertainty. In summary, the spatial interpretation of these photometric distributions suggests the LMC consists of a centrally concentrated barred disk and some number of extended

distributions, including a spheroid and tidally distorted and possibly stripped populations.

3.6 Summary

We have analyzed the spatial distributions of several LMC populations, identified based on their location in the color-magnitude diagram. Quantitative analysis of the observed distributions includes parametric source-count and a preliminary standard candle analysis. Our major conclusions are:

- Projected star count analyses based 2MASS data yield scale lengths, deprojection-based inclinations, and position angles consistent with previous studies. The near-far degeneracy of the disk orientation is broken by perspective difference. The near side of the Cloud subtends a larger angle in the sky-and this allows us to determine that Eastern side of the disk is closer, in agreement with Cepheid-based results.

- We propose using carbon-rich LPVs in a narrow color range, $1.6 < J - K_s < 1.7$ as standard candles to probe the structure of the LMC along the line of sight. Based on published light curves, their intrinsic magnitudes have a dispersion of $\lesssim 0.3^m$ including the random phase of the observations. The width of the LMC disk in the observed photometric distribution ($\sigma_m = 0.2$) suggests that these are acceptable standard candles.

- The photometric distribution of our standard candle sample reveals strong central peak with extended tails in both directions, with tail toward fainter magnitudes more pronounced. The stronger secondary peak is 0.7^m fainter than the main peak and includes 20% of the LPVs, while the weaker secondary component is 0.6^m brighter than the main peak and includes only 5% of all variables.

We interpret the primary peak as due to the midplane of the LMC disk and examine various possibilities which could produce the tails and secondary peaks of observed distribution. We conclude that the photometric distribution of standard candles is most likely caused by a spatially extended stellar component and tidally stripped debris, consistent with a tidally disturbed dwarf companion. It is possible that the distribution reflects the intrinsic period distribution of LPVs or distinct populations of masses (ages) and metallicities for these stars, but such explanations special populations or evolutionary histories.

- The distribution of apparent magnitudes of standard candles is consistent with tilted geometry derived from star counts. We derive a *direct* determination of the LMC disk inclination of $42.3° \pm 7.2°$, consistent with Laney & Stobie (1986) estimate of $45° \pm 7°$ and with results of Welch et al. (1987), $37° \pm 16°$. Interpreting the apparent luminosity function as due to real source density, we find evidence of the extended component of the LMC, with a width of approximately 8 kpc (for $\sigma_M = 0.1^m$ and the LMC distance $R_{LMC} = 50$ kpc).

This detection of this thick component implies that LMC may contain a kinematically distinct population as suggested by Graff et al. (1999) and/or an the extended component found by Hughes et al. (1991) and predicted for the tidal interaction with the Milky Way (Weinberg 2000). Tidal stripping is a natural dynamical consequence of the LMC–Milky Way interaction and some evidence for extra-tidal debris may have been found by Kunkel et al. (1997). Theoretically, mass loss should be found for any star cluster or dwarf. Indeed, tidal debris has now been detected in globular clusters (e.g. Grillmair et al. 1995) with the characteristic S-shaped profile expected for loss through the saddle points in the effective potential (Lagrange points). Similar predictions have been made by Johnston et al. (1999) for dwarf galaxies. Conversely, a definitive failure to detect a stripped stellar component will necessitate a reevaluation of LMC structure. A speculative possibility is that a more massive LMC recently lost

equilibrium in the Milky Way tidal field. The exposure of the disk to a significant tidal force might be recent. In such a scenario, the SMC most likely was a satellite of the larger primordial LMC and is now interacting directly with its luminous gas-rich disk. More generally, these dynamical mechanisms will affect all Magellanic-like systems and may help constrain their histories and determine the extent of their dark matter halos.

The existence of such a population may affect the self-lensing models of the LMC in the microlensing studies depending on its spatial distribution. These preliminary results suggest a number of projects for short- and long-term follow-up. An improved analysis of the 2MASS sample may be obtained with larger sample of standard candles, or with full three dimensional analysis based on several distinct standard candles using data from the entire survey rather than selected fields (work in progress). Assuming that the extended stars originated in the disk, both populations will appear rotationally supported. However, using the 2MASS photometric distribution as a guide, a combined disk and extended spheroid population should be kinematically separable and these stars are good candidates for future spectroscopic work.

Table 3.3 Best fit parameters of exponential disk model ($\sim$ 1000 d.o.f.). The reported errors are purely statistical.

Region	α_0^a	δ_0^a	R	i	θ^b	ρ_D	ϕ^c	a	q	χ^2/d.o.f.
					No bar					
A	81.1	−68.8	1.63 ± 0.01	35.0 ± 0.8	87.3 ± 1.4					7.67
E	80.8	−69.6	1.58 ± 0.01	23.3 ± 0.4	167.6 ± 1.1					23.05
F	80.7	−69.5	1.34 ± 0.01	25.8 ± 0.9	168.3 ± 2.4					4.81
G	80.6	−69.3	1.33 ± 0.03	28.7 ± 2.4	114.5 ± 5.8					1.20
H	80.8	−68.7	1.77 ± 0.02	22.3 ± 2.0	90.7 ± 5.6					4.26
J	80.9	−69.5	1.37 ± 0.01	25.4 ± 1.5	168.9 ± 3.7					2.27
K	80.6	−69.5	1.44 ± 0.02	27.2 ± 2.4	173.4 ± 5.3					1.16
					Bar included					
A	80.9	−68.7	1.74 ± 0.02	-57.8 ± 0.8	59.1 ± 0.7	2.8 ± 0.3	-8.0 ± 0.5	1.1 ± 0.1	3.9 ± 0.2	7.10
E	80.6	−69.7	2.40 ± 0.02	-37.9 ± 0.4	16.9 ± 0.6	0.2 ± 0.0	9.3 ± 0.4	0.4 ± 0.0	2.7 ± 0.0	8.27
F	80.4	−69.6	1.89 ± 0.03	-40.2 ± 1.0	17.1 ± 1.3	0.3 ± 0.0	9.2 ± 0.9	0.4 ± 0.0	3.5 ± 0.1	2.97
G	80.5	−69.5	1.64 ± 0.06	26.7 ± 4.0	176.5 ± 9.5	0.4 ± 0.1	17.3 ± 8.1	0.3 ± 0.0	3.5 ± 0.3	1.06
H	80.5	−68.6	2.11 ± 0.06	-61.6 ± 1.6	54.8 ± 1.0	1.8 ± 0.3	-3.2 ± 0.5	1.1 ± 0.1	4.4 ± 0.3	3.70
J	80.7	−69.6	1.81 ± 0.04	-38.3 ± 1.6	11.8 ± 2.2	0.4 ± 0.0	9.9 ± 1.7	0.4 ± 0.0	3.4 ± 0.2	1.75
K	80.5	−69.6	2.09 ± 0.11	-40.9 ± 2.7	11.7 ± 3.3	0.3 ± 0.0	10.4 ± 2.5	0.4 ± 0.0	3.2 ± 0.3	0.91

[a]Distribution centroids are in J2000.0 system. Their positional accuracy is $\lesssim 0.1°$.

[b]Position angle is measured from the North in the counterclockwise direction (i.e., NESW).

[c]Orientation (i.e. azimuthal) angle of the bar in the plane of the exponential disk.

Table 3.4 Same as Table 3.3, except for power-law models.

Region	α_0	δ_0	ν	i	θ	ρ_D	ϕ	a	q	χ^2/d.o.f.
					No bar					
A	80.7	-69.0	2.49 ± 0.02							12.10
E	80.6	-69.6	2.45 ± 0.02							40.42
F	80.5	-69.6	2.52 ± 0.02							9.98
G	80.6	-69.5	2.53 ± 0.02							2.04
H	80.6	-68.5	2.45 ± 0.02							5.55
J	80.6	-69.5	2.48 ± 0.02							4.60
K	80.5	-69.5	2.49 ± 0.02							1.55
					Bar included					
A[a]										
E	80.5	-69.7	1.67 ± 0.02	74.2 ± 0.7	151.9 ± 2.2	0.7 ± 0.0	7.2 ± 0.4	2.9 ± 0.1	3.3 ± 0.0	9.96
F	80.3	-69.7	1.75 ± 0.04	80.7 ± 0.8	137.0 ± 3.5	0.8 ± 0.1	4.6 ± 0.8	4.1 ± 0.4	4.1 ± 0.0	3.24
G	80.6	-69.3	2.81 ± 1.03	73.8 ± 3.2	139.3 ± 20.2	0.1 ± 0.2	3.1 ± 0.9	4.2 ± 1.1	3.3 ± 0.1	1.23
H[a]										
J	80.7	-69.6	1.77 ± 0.08	79.4 ± 1.2	152.3 ± 7.3	0.8 ± 0.2	4.2 ± 0.5	5.6 ± 0.9	5.3 ± 0.0	1.96
K	80.2	-69.6	1.81 ± 0.09	81.7 ± 2.7	92.3 ± 13.0	1.2 ± 0.3	-5.8 ± 1.8	4.3 ± 1.2	6.0 ± 0.1	1.22

[a]In Regions A and H, no solution have been found.

CHAPTER 4

LMC STRUCTURE FROM PHOTOMETRIC AND KINEMATIC DATA

4.1 Introduction

The Large Magellanic Cloud is our closest galactic neighbor and its structure is important to understanding the dynamics and stellar evolution in the 'Galaxy-Magellanic Clouds' system. Based on wide-angle photographs (de Vaucouleurs & Freeman 1973), the LMC represents a $16° \times 14°$ elliptical object at $l = 280.5°$, $b = -32.9°$ (Westerlund 1997), approximately 50 kpc from the Sun. (Recently, Irwin (1991) estimated a size of $23° \times 17°$ from star counts.) Morphologically, the LMC is an irregular galaxy with a few recognizable features: *the stellar bar*, measuring $3.5° \times 1.0°$ with the position angle of its major axis at 120°; *spiral arms* outlined by very young Population I stars, superassociations and H I complexes (Kim et al. 1998); and *faint outer loop* seen in the distribution of carbon stars (Westerlund 1964).

Despite the apparently complex morphology of the LMC, the kinematical studies based on a variety of stellar and gas tracers indicate a kinematics dominated by a single disk. Rotation solutions derived from H I gas (Rohlfs et al. 1984, Luks & Rohlfs 1992, Kim et al. 1998), H II regions, supergiants, CO clouds (Hughes et al. 1991), CH stars (Cowley & Hartwick 1991, Hughes et al. 1991), star clusters (Schommer et al. 1992), long-period variables (Hughes et al. 1991), and planetary nebulae (Meatheringham et al. 1988) all imply a single disk potential. No hot pressure-supported halo has been discovered in the LMC, although Hughes et al. (1991) argue for flattened spheroid kinematics in population of old LPVs. Perhaps due to such a strong evi-

dence pointing to a single disk, most studies attempting to analyze the structure of the LMC have *a priori* assumed a simple disk model suggested by kinematics. The inclinations and position angles of the disk derived from isophotal fits (McGee & Milton 1966, de Vaucouleurs & Freeman 1973, Bothun & Thompson 1988, Schmidt-Kaler & Gochermann 1992), star counts (de Vaucouleurs 1955) and other techniques (Feitzinger et al. 1977, Caldwell & Coulson 1986, Welch et al. 1987, Cole 1999) have been in general agreement with each other, and solidified the view of the LMC a single disk.

However, recent data suggest that the LMC may not be such a simple system after all:

1. Analysis of MACHO microlensing statistics toward the Cloud (Alcock et al. 2000b) results in microlensing optical depth $\tau = 1.2^{+0.4}_{-0.3} \times 10^{-7}$. While an interpretation of this result in terms of Galactic MACHO halo has problems with baryonic fraction (Fields et al. 1998), such an optical depth is also too high to be explained by thin disk self-lensing models (Gould 1995, Gyuk et al. 2000). For efficient self-lensing, there must be sufficient separation between sources and lenses, which is lacking in thin disk models. All searches for extended halo of the LMC based on kinematic tracers have so far turned up negative (see summary of results in Gyuk et al. 2000). However, numerical n-body simulations (Weinberg 2000) suggest that LMC disk stars will be torqued out of the disk plane thus thickening the disk and increasing the microlensing optical depth. Importantly, this mechanism will not isotropize stellar orbits and the kinematics torqued stars will remain disk-like. In addition, during this process, the binding energy of the disk will decrease, which may result in tidal stripping of the outer regions of the Cloud. The stripped stars may also contribute to microlensing;

2. At least two MACHO events (MACHO-LMC-1a and MACHO-LMC-9) are probably located in the LMC (Zhao & Evans 2000, Kerins & Evans 1999). Bi-

nary caustic crossing removes the degeneracy in three lens parameters: mass, distance, and transversal velocity. The fact that all binary lenses (MACHO-LMC-9, Bennett et al. 1996; 98-SMC-1, Albrow et al. 1999, Alcock et al. 1999) are located in the Clouds suggests that most observed events are due to Cloud deflectors (Di Stefano 1999, Kerins & Evans 1999). This also argues against the thin disk scenario;

3. Zaritsky & Lin (1997) have argued for a presence of intervening population toward the LMC. Even though the claim has been disputed by several groups (Gallart 1998, Bennett 1998, Gould 1998, Beaulieu & Sackett 1998), the evidence for tidally stripped material from simulations of (Weinberg 2000) may have been found in the distribution of carbon-rich LPVs (see previous chapter);

4. Zhao & Evans (2000) proposed that the LMC "bar" is in fact a misaligned and displaced plane structure seen in projection. They argued that $\sim 25°$ difference in disk and "bar" inclinations could bring the self-lensing optical depth close to MACHO result. An extreme suggestion at first sight, this does not seem so contrived given the well known fact that the optical center of the LMC bar is displaced relative to both the rotation center and the centroid of old populations (de Vaucouleurs & Freeman 1973). Moreover, the origin of the spiral system of the LMC is also off-centered (30 Dor; simulations (Gardiner et al. 1998) suggest that an off-center bar could generate an asymmetric spiral structure). Also, if one interprets the observed photometric distribution of carbon stars (see previous chapter) as due to geometric structure, then the magnitude shift between components $\sigma \approx 0.13$ mag also suggests an out of plane configuration;

5. Possible signature of a non-disk population has also been discovered in kinematic studies. Analysis of H I rotation (Luks & Rohlfs 1992) produced two distinct components: disk with a symmetric rotation curve, and L-component,

consisting of two large complexes linked by 30 Dor nebula. The velocity difference of the L-component and the disk is $\sim 20 - 30$ km/s; it is believed to be located behind the main H I disk. Recently, Graff et al. (2000) have argued for a distinct kinematic population, seen in the velocities of carbon stars; the velocity difference is very similar to Luks and Rohlfs' value;

To summarize, the LMC is clearly more complex than a single thin disk. It may have a thick disk/spheroid, possibly misaligned bar and be immersed in a shroud of tidal debris. In this paper, we use a ML approach to analyze LMC photometric and kinematic data *combined*. We analyze the residuals (both photometric and kinematic) from single-disk LMC representation. Any correlation between photometric and kinematic residual would provide a very strong evidence to an LMC structure other than the disk. By utilizing high-accuracy photometric data from 2MASS and kinematics data from several sources in the literature we are able to improve the sampling of data space and better constrain the models.

4.2 Data

Our ML analysis is based on combination of photometric and kinematic data[1]. The photometric data are taken from 2MASS Second Incremental Release catalog. Based on the analysis of the LMC color-magnitude diagram (see Table 2.3), only four regions in the diagram have the estimated fraction of Galactic foreground sources f_{gal} less than 0.05: regions F, G, J, K[2]. Since our ML-algorithm is a variation of standard candle analysis, we need to choose sources whose luminosity can be quantified. Sources in Region K can therefore be discarded as strongly affected by circumstellar dust. These stars have large reddenings $E_{B-V} \gtrsim 1$ and cannot be considered standard candles. This leaves only sources in Regions F, G, and J, which have been identified with

[1]Astrometric data (positions) are also known.

[2]Region L has $f_{gal} = 0.01$, but is contaminated by extragalactic objects

oxygen-rich (F, G) and carbon-rich (J) long-period variables. As LPVs, these stars obey a statistical linear period-luminosity-color (PLC) relation (Feast et al. 1989). Projecting the PLC relation on the luminosity-color plane results in a linear LC relation. On the CMD, which is the luminosity-color plane, these stars will be distributed along two loci, one for oxygen-rich and the other for carbon-rich LPVs, and the luminosity of these stars can be quantified as a function of their near-infrared color. We have shown that carbon stars in a narrow color interval represent standard candles of high quality ($\sigma_M \sim 0.2$). Unfortunately, due to steeper LC relation for M-stars, parameters of their LC relation are constrained more poorly, and may be a cause for bias in our ML method. Because of this, and also because of the reasons discussed in §4.3, we use only sources from Region J as our photometric sample. This amounts to 8229 stars with accurate JHK_s photometry ($\sigma_{ph} < 0.04$). Given the fact that these stars are considerably brighter than 2MASS flux limit (14.3^m in K_s), and unaffected by crowding (as demonstrated in Chapter 2), we have a virtually complete sample of LMC carbon-rich LPVs in the color range $1.4 < J-K_s < 2.0$. In our analysis, we will utilize only two-band photometry, $J-K_s$ color and K_s-magnitude, but generalization to three and multiband case is straightforward.

Kinematics data for our ML analysis were taken from several sources in the literature (Kunkel et al. 1997a, Prévot et al. 1985, Hughes et al. 1991). Since one of the advantages of our ML method is that it places different data within the same framework (model), we may use a wide variety of kinematic data available in the literature. In fact, as we will show below (§4.3), one can use data obtained from a variety of tracers (HI gas, planetary nebulae, globular clusters, etc.), not just C-stars! Our main source for kinematics data is Kunkel et al. (1997a). They list radial velocities for 539 carbon stars in the LMC, SMC and intercloud region. Selecting only LMC sources leaves 428 stars, mainly in the periphery of the LMC, of which 232 are matched to our Region J sources to within $2''$. As an additional source, we use Hughes

et al. (1991), who provided radial velocities for a sample of $\sim$ 270 LPVs discovered in the LMC by Hughes (1989) and Reid et al. (1988). Their sample contains both C- and M-type LPVs. We find 114 stars in their sample classified as C or CS, and of those, just 27 can be matched to Region J sources. Sample of Prévot et al. (1985) contains 393 F—M type supergiants and does not have matching sources with our photometric sample. All kinematic data are corrected for the transverse motion of the LMC based on HIPPARCOS measurements of proper motions of 33 LMC stars (Kroupa & Bastian 1997), see Appendix B.

To summarize, our total sample consists of 259 stars with both photometry and kinematics, 7970 stars with photometry only and 823 stars with only kinematic data. The distribution of stars in our sample in the sky is shown in Figure 4.1. Figure 4.2 shows the location of selected sources in the color-magnitude diagram.

4.3 Method

In this section, we give the details of our ML algorithm, which represents photometric and kinematic data by a unified model to derive the structural parameters of the LMC. In further discussion, we assume that our total sample of size N contains n_1 records with both photometry and kinematics, $\{\alpha, \delta, J-K_s, K_s, v\}$, n_2 records with photometry only, $\{\alpha, \delta, J-K_s, K_s\}$, and n_3 records with kinematics only, $\{\alpha, \delta, v\}$. For clarity, we henceforth shall omit the subscript "s" in K_s, and denote $C \equiv J-K$.

4.3.1 Data Probabilities

The likelihood function is the cumulative probability of the data given the model. In our particular case, we may write

$$L = \prod_{i=1}^{n_1} P_i(\alpha_i, \delta_i, C_i, K_i, v_i|\Theta) \prod_{j=1}^{n_2} P_j(\alpha_j, \delta_j, C_j, K_j|\Theta) \prod_{k=1}^{n_3} P_k(\alpha_k, \delta_k, v_k|\Theta), \qquad (4.1)$$

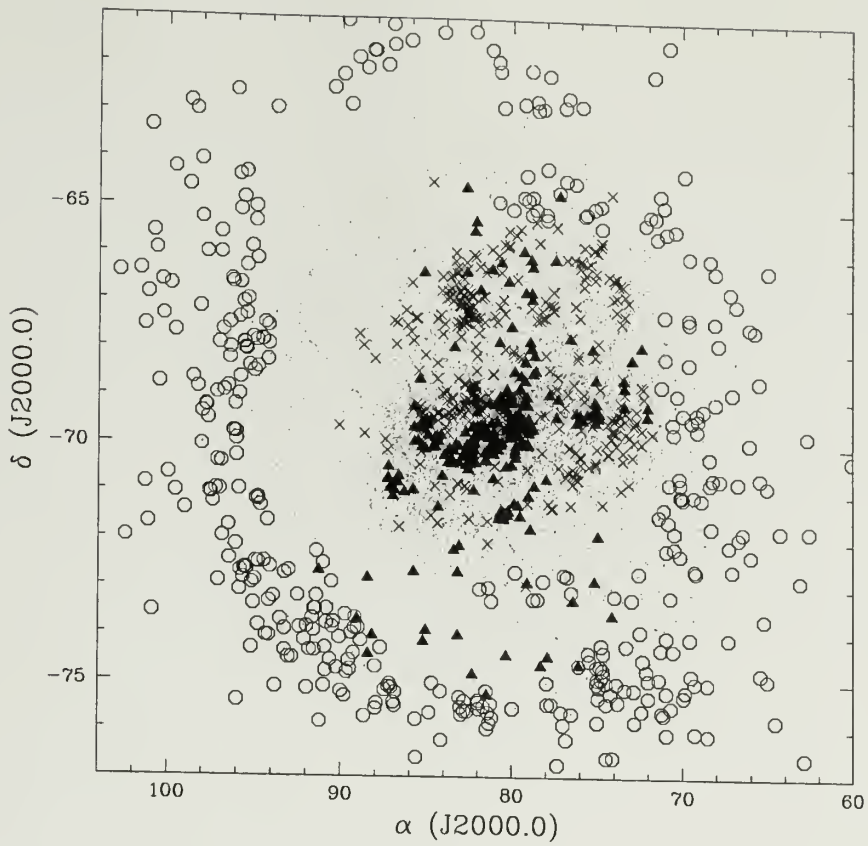

Figure 4.1 Sky distribution of sample sources. Points are 2MASS photometry data, open circles represent LMC carbon stars from Kunkel et al. (1997a), crosses are CORAVEL stars (Prévot et al. 1985), and triangles are LPVs from Hughes et al. (1991).

where Θ is the vector of model parameters to be estimated. The expressions for the constituent probabilities in equation (4.1) may be derived from the formula of full probability:

$$P(\alpha,\delta,C,K,v|\Theta) = \int P(\alpha,\delta,C,K,v,r|\Theta)\,dr = \int dr\, P(\alpha,\delta,r|\Theta)\, P(C,K|\alpha,\delta,r,\Theta)\, P(v|\alpha,\delta,C,K,r,\Theta), \quad (4.2)$$

where we have explicitly written the dependence on unobserved distance to a star r. By integrating (or 'marginalizing') over unobserved variables, we obtain the expression for the probability which depends only on observed quantities. Thus, we may write

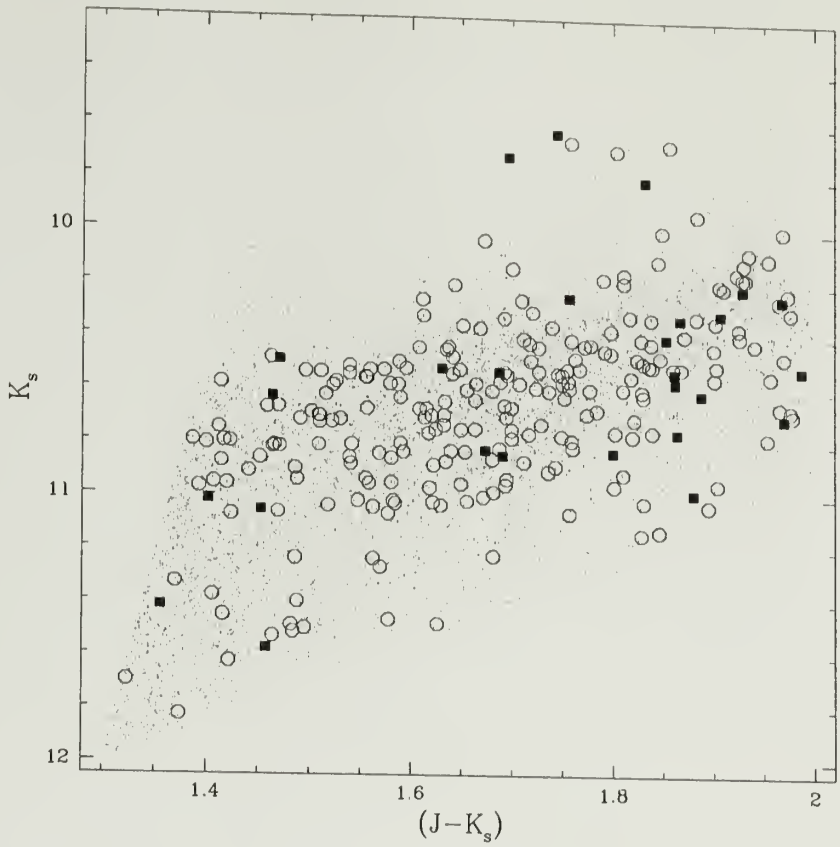

Figure 4.2 Color-magnitude diagram of the sample. Symbols are the same as in Figure 4.1.

$$P(\alpha, \delta, C, K|\Theta) = \int dr \int dv\, P(\alpha, \delta, C, K, v, r|\Theta), \tag{4.3}$$

$$P(\alpha, \delta, v|\Theta) = \int dr \int dC \int dK\, P(\alpha, \delta, C, K, v, r|\Theta) \tag{4.4}$$

for the other two probabilities on the right-hand side of equation (4.1).

Therefore, to write the likelihood function, we must provide the expressions for each probability distribution in equation (4.2). We consider each of them in turn.

4.3.2 Spatial Density

The probability $P(\alpha, \delta, r)$ is proportional to the spatial density. In our analysis, it is modeled with a thin exponential disk or with a sum of two thin exponential disks,

$$\rho(r, \alpha_i, \delta_i) = \Sigma_1 \exp(-R_i'/H_1) + \Sigma_2 \exp(-R_i''/H_2),$$

where C_2 is zero or a free parameter. The scale lengths H_1 and H_2 are free parameters of the model. The radius vectors R' and R'' are functions of position angle θ_0, inclination i and coordinates α_i, δ_i (see Appendix A.1). The two-disk model can also be used to detect a warp of the primary LMC disk or any material out of the primary disk plane (e.g. tidally pulled "tails"). The two disks may or may not coincide, to allow for a variety of possible configurations. This model can also accommodate disks of small, but finite thickness, because the double exponential disk $\rho = \rho_0 \exp[-R/H - |z|/h]$ will have the same projected density as thin disk with normalization parameter C adjusted by $2h$.

An important part of $P(\alpha, \delta, r)$ is indicator function, which represents the location of the data in the sky. Denoting this function by $\zeta(\alpha, \delta)$, we may write

$$P(\alpha, \delta, r) = \zeta(\alpha, \delta)\, \rho(\alpha, \delta, r).$$

This function is constant across the LMC field for photometric data, because 2MASS has complete coverage of the LMC. However, as apparent from Figure 4.1, the distribution of kinematic data in the sky plane is far from uniform. For example, it is clear that using data from Kunkel et al. (1997a) alone to determine the scale length of the exponential disk H in our model will lead to biased estimate. Even combined with the photometric sample, the uneven sky coverage of kinematic data will result in bias. To counter that effect, we assume a delta-function form for each star with kinematic data, $\zeta(\alpha, \delta) = \delta(\alpha - \alpha_0)\delta(\delta - \delta_0)$. This will effectively localize kinematic data and remove any effect they might have on the large-scale structure.

4.3.3 Distribution in Color-Magnitude plane

The color-magnitude diagram of the LMC (Figure 4.2) reveals that stars from our photometric sample follow a linear relation between color and magnitude. This is a manifestation of the LC relation for carbon-rich LPVs. In terms of the intrinsic magnitudes and colors, we can write

$$K_0 = \xi\, C_0 + \eta.$$

Given the usual relation between absolute and apparent magnitudes including interstellar reddening, $K = K_0 + 5\log r(kpc) + 10 + A_K$, the LC relation in the apparent plane will be parametrized by

$$K = \xi\, C + \eta'.$$

Note that the slope of the relation remains unchanged, while zero point η' now reflects the distance modulus of the LMC and the reddening that occurs between an observer and the LMC:

$$\eta' = \eta + 5\log r + 10 + A_K - \xi E_{J-K}.$$

Even assuming the distance modulus to the LMC is known, one cannot remove the degeneracy between true zero point η and reddening A. However, the degeneracy can be lifted by adding another photometric band (e.g., H) to the analysis. Indeed, by adding an extra color dimension, we introduce only one additional variable (respective zero point η_H), but two additional equations, one similar to the equation above, and the other for color correlation (A_H and A_K are not independent). In our analysis, we hide the true zero point and extinction (and the LMC distance modulus) in one variable η', which can be estimated from the observed CMD. The linear regression fit for our sample with $1.5 < C < 2.0$ gives

$$K = (-1.192 \pm 0.032)\, C + (12.641 \pm 0.056), \qquad \sigma = 0.338. \tag{4.5}$$

These values for ξ and η' are held fixed throughout the analysis.

To parameterize the distribution of stars in the CMD plane given the linear dependence (4.5), we first assume that intrinsic color and the luminosity of a carbon star are independent of star's location in the LMC. Therefore, we may drop the position coordinates:

$$P(C, K|\alpha, \delta, r, \Theta) = P(C, K|\Theta).$$

Furthermore, we assume a uniform distribution of colors, $P(C) = Const.$ The actual distribution of colors in Region J is flat only up to $C = 1.8$ and then monotonically decreases by about 20% at $C = 2.0$. To test whether the assumption of flat color distribution leads to bias in the slope of the recovered LC relation we performed Monte Carlo simulations by drawing random samples from the actual color distribution and from the flat distribution and calculating the slope of the linear relation. The slopes are consistent with each other, ensuring no bias.

Finally, we assume a Gaussian distribution in magnitudes, centered on the magnitude defined by the LC relation:

$$P(C, K|\Theta) \propto \exp\left[-\frac{(K - \overline{K})^2}{2\sigma_K^2}\right], \tag{4.6}$$

where $\overline{K}$ is given by equation (4.5). We note that σ_K includes both the intrinsic dispersion of the LC relation as well as photometric errors, variance due to interstellar reddening and distance.

4.3.4 Radial Velocity Profile

The final term in equation (4.2) is the radial velocity profile. We make an assumption that radial velocity of a star in the LMC disk is independent of the star's color and luminosity and is a function of position only. Similar to magnitude distribution, we also assume a Gaussian distribution of rotation velocities,

$$P(v|\alpha, \delta, \Theta) \propto \exp\left[-\frac{(v - \overline{v})^2}{2\sigma_v^2}\right],$$

where $\overline{v}$ is the expected radial velocity in the midplane of thin Freeman disk (see Appendix B). The parameter σ_v characterizes the velocity dispersion of disk population, as well as errors in determined radial velocities.

4.3.5 Likelihood Function

Putting together the components of the full probability (Equation 4.2), and marginalizing the resulting components over unobserved variables, we arrive to the following

expressions:

$$P(\alpha,\delta,C,K,v) = \frac{1}{2\pi\sigma_v\sigma_K}\frac{\rho_1\overline{r}_1^2\Phi_1\Psi_1+\rho_2\overline{r}_2^2\Phi_2\Psi_2}{\rho_1\overline{r}_1^2+\rho_2\overline{r}_2^2},$$

$$P(\alpha,\delta,C,K) = \frac{1}{\sigma_K\sqrt{2\pi}}\frac{(\rho_1\overline{r}_1^2\Phi_1+\rho_2\overline{r}_2^2\Phi_2)\cos\delta}{\int d\alpha\int d\delta\cos\delta(\rho_1\overline{r}_1^2+\rho_2\overline{r}_2^2)}, \qquad (4.7)$$

$$P(\alpha,\delta,v) = \frac{1}{\sigma_v\sqrt{2\pi}}\frac{\rho_1\overline{r}_1^2\Psi_1+\rho_2\overline{r}_2^2\Psi_2}{\rho_1\overline{r}_1^2+\rho_2\overline{r}_2^2},$$

where we use the notations

$$\Phi = \exp\left[-\frac{(K-\overline{K})^2}{2\sigma_K^2}\right], \qquad \Psi = \exp\left[-\frac{(v-\overline{v})^2}{2\sigma_v^2}\right],$$

and the subscripts "1" and "2" denote first and second exponential disks. The distance $\overline{r}$ corresponds to the midplane of the disk (see Appendix A.1). Note that $P(\alpha,\delta,C,K,v)$ and $P(\alpha,\delta,v)$ are normalized to local density (no integral over spatial coordinates in the denominator), in accordance with the discussion above. Also, if no data with both photometry and kinematics are available, the method effectively reduces to weighted averaging of photometry-only and kinematics-only probabilities, with the weights given by respective numbers of sources.

As usual, ML algorithm is set to maximize the log-likelihood

$$\log L = \sum_{i=1}^{n_1}\log P_i(\alpha_i,\delta_i,C_i,K_i,v_i|\Theta)+\sum_{j=1}^{n_2}\log P_j(\alpha_j,\delta_j,C_j,K_j|\Theta)+\sum_{k=1}^{n_3}\log P_k(\alpha_k,\delta_k,v_k|\Theta), \qquad (4.8)$$

where P_i, p_j and P_k are given by equations (4.7). Model parameters that maximize the log-likelihood (4.8) define the best model given the data.

For the model represented by two exponential disks, the general number of free parameters is 16. The parameters are: disk centers, α_1, δ_1, α_2, δ_2 (we assume geometric center coincides with the rotation center); inclinations i_1, i_2; position angles of the lines of nodes, θ_1, θ_2; disk scale lengths H_1 and H_2; rotation parameters for

both disks V_{01}, V_{02}, $\Upsilon_{m,1}$, $\Upsilon_{m,2}$; the distance to the second disk[3] R_2; and the ratio of the disk normalization parameters[4] Σ_1/Σ_2. The peaks of the rotation curves $R_{m,1}$ and $R_{m,2}$ (see Appendix B) are constrained through theoretical result for thin disks by Freeman (1970), that $R_m \sim 2.2H$. The shape of the rotation curve (parameter a) is always held fixed at $a = 0.5$.

4.3.6 Possible Modifications of the Likelihood

Given the form of the likelihood function (4.8), one can easily introduce additional photometric bands. Existing LC relations for LPVs in all bands allow straightforward modification of the algorithm. Another possible improvement concerns weighting of data. Different weights may be assigned to separate sums in log-likelihood equation,

$$\log L = f_1 \sum_{i=1}^{n_1} \log P_i() + f_2 \sum_{j=1}^{n_2} \log P_j() + f_3 \sum_{k=1}^{n_3} \log P_k(),$$

to emphasize the importance of a certain kind of data. The weights may even be assigned to particular components of individual sums in (4.8) to manipulate the relative importance of data from a certain source in the sample.

Adding microlensing optical depth τ to the list of observed quantities in (4.2) can improve the analysis even further. The optical depth due to microlensing can be written as an integral along the line of sight:

$$\tau = \frac{\int_0^\infty \tau'(L)\rho_s(L)\,dL}{\int_0^\infty \rho_s(L)\,dL},$$

where

$$\tau'(L) = \frac{4\pi G}{c^2} \int_0^L \rho_l(l)\,\frac{l(L-l)}{L}\,dl$$

is the optical depth due to sources at a distance L. Here l is the distance to the lens, and ρ_s and ρ_l are densities of sources and lenses, respectively. We see that the optical depth is a function of the distribution of matter along the line of sight and thus should help in constraining different models.

[3]The distance to the first disk is assumed 50 kpc.

[4]As follows from equations (4.7), only ratio of the normalization is constrained, not the absolute values.

Table 4.1 Parameters of single disk LMC models.

Number	α_0	δ_0	i	θ_0	H	V_0	Υ_m	S_m
				Photometry only				
0[a]	80.9	-69.5	25 ± 2	169 ± 4	1.37 ± 0.01			
1	80.8	-69.5	23 ± 2	143 ± 3	1.27 ± 0.02			
2	(79.4)	(-69.03)	26 ± 2	141 ± 12	1.33 ± 0.02			
				Kinematics only				
3[b]	(79.4)	(-69.03)	(33.0)	163 ± 1	(1.6)	4.0 ± 0.5	21.7 ± 0.4	(0.28)
4[b]	(79.4)	(-69.03)	26 ± 5	162 ± 1	(1.6)	4.2 ± 0.5	26.7 ± 4.4	(0.28)
				Kinematics and Photometry				
5	(79.4)	(-69.03)	26 ± 2	166 ± 1	1.31 ± 0.02	5.6 ± 0.4	30.8 ± 2.3	(0.35)
6[b]	80.8	-69.4	24 ± 2	161 ± 2	1.22 ± 0.02	1.6 ± 0.7	39.3 ± 3.1	(0.37)
7	80.8	-69.4	24 ± 2	165 ± 1	1.25 ± 0.02	-1.1 ± 0.4	32.8 ± 2.4	(0.36)
				Split Center[c]				
8[b]	80.8	-69.5	24 ± 2	158 ± 1	(1.21)	4.0 ± 0.7	39.6 ± 3.0	0.37
9	80.8	-69.5	25 ± 2	164 ± 1	(1.27)	3.7 ± 0.4	31.1 ± 2.2	0.36
10[b,d]	80.8	-69.5	25 ± 1	159 ± 1	(1.26)	4.1 ± 0.1	36.7 ± 1.6	0.36

[a] Results from binned likelihood analysis (Chapter 3 on Region J sources.
[b] Kinematic data are taken from Kunkel et al. (1997a) only.
[c] Solution obtained assuming separate centers for photometric and kinematic distributions. Estimates are given for photometric center; rotation center is fixed to (79.4°, −69.03°).
[d] Photometric and kinematic subsamples are 'evened out' by introducing weight factors inversely proportional to the size of subsample, $f \propto N^{-1}$.
Note: Positions of the population centroids listed in the Table are in J2000.0 system, with typical errors $\sim 0.3°$. The values of parameters shown in parentheses are held fixed. For rotation curve parameters, see Appendix B.

4.4 Results

4.4.1 Single Disk Model

The results for a single disk model are summarized in Table 4.1. For most of the estimations, we use $\sigma_K = 0.4$ and $\sigma_V = 9.0$ km/s. The former number is an estimate of the intrinsic dispersion of luminosity-color relation, convolved with variance in extinction and observation errors; the latter is a conservative estimate of the velocity measurements for our kinematic sample.

First, we maximize the likelihood function for photometric data only. This procedure is similar to what we have done in the previous chapter, except sky coordinates are not binned. We find a reasonable agreement with the previous results, as indicated by comparison of the first two lines in Table 4.1. The observed projected density is compared to the model in Figure 4.3. Fixing the disk center to HI rotation

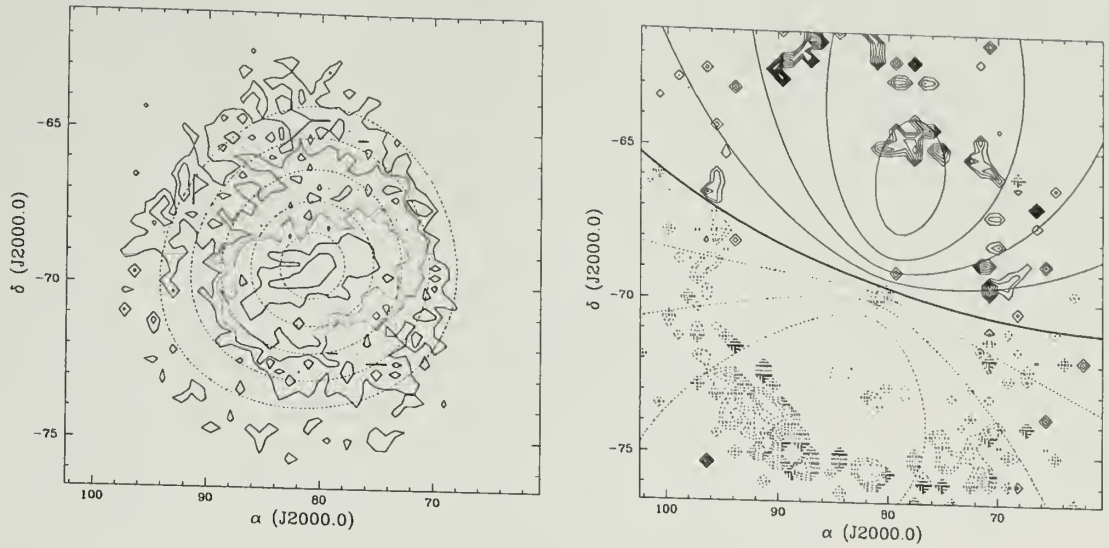

Figure 4.3 Model density and velocity field for single disk LMC models. *Left panel*: Observed projected density for the LMC (solid contour levels) and best fit single-disk photometry-only model (dotted lines). *Right panel*: Magellanocentric velocity field $v_{rad}(\alpha, \delta)$ for best-fit kinematics-only solution based on 428 carbon stars. Solid lines denote positive velocity, dotted lines – negative velocity. Contour levels are spaced by 10 km/s; contour level corresponding to zero velocity is highlighted.

center at $\alpha = 05^h17^m.6$, $\delta = -69°02'$ (J2000; Kim et al. 1998) does not affect the disk parameters.

As a test, we have applied our ML algorithm to the kinematics data used by Alves & Nelson (2000) to derive the rotation parameters of the LMC disk. Due to peculiar distribution of carbon stars in Kunkel's et al. data set, our estimate of the radial scale length is likely to be biased. Therefore, the radial scale length is set to a fixed value, $H = 1.6$ kpc. This value, derived from distribution of RR Lyr stars in the LMC (Alcock et al. 2000a), is somewhat higher than our typical scale length derived from photometry, $H \sim 1.3$ kpc. Nevertheless, we use this value to facilitate comparison with results from Alves & Nelson (2000). To further constrain the model, we use a theoretical result for thin exponential disks (Freeman 1970), $R_{max} \sim 2.2H$, where R_{max} is the radius where maximum rotation velocity is attained. From Table 4.1 we see that while some difference exists in the two approaches (e.g., instead of binning

the deprojected radii and solving for rotation in annuli, we parameterize the rotation curve shape through the parameter a), the two methods give essentially the same results. Figure 4.3 shows the rotation field v_{rad} as a function of sky coordinates. Adopting the same values for rotation center, inclination and disk scale length as used by Alves & Nelson (2000), we find the peak circular velocity $V_{max} = 76.4$ km/s, close to their estimate $V_{max} = 73$ km/s. If the disk inclination is allowed to change, the best solution has smaller inclination $i = 25.9°$, while the position angle of the line of nodes is unchanged. Smaller inclination means higher peak circular velocity (because of $\cos i$ factor), $V_{max} = 93 \pm 15$ km/s, and therefore, higher disk mass.

For a combined dataset with both photometry and kinematics, we find very similar results whether the disk center is fixed or allowed to change. Our best estimates give disk inclination $i = 24 - 26°$, with the line of nodes at position angle $\theta = 158 - 166°$. The disk scale length is ~ 1.3 kpc and the peak circular velocity is $V_{max} \sim 90$ km/s. Since the disparity between rotation and optical centers of the LMC has been a long known fact (e.g. de Vaucouleurs & Freeman 1973), in some solutions we explicitly separated the two. In these cases, the position of the rotation center is fixed, because kinematic data have peculiar distribution in the sky (see Figure 4.1, which may bias the derived estimate. We find no significant changes in disk parameters in disk parameters if kinematic and optical centers are separated. Finally, we also estimated disk parameters for a case of weighted data. Due to dominance of photometric data in our sample, the inference is based primarily of the photometric subsample. We may attempt to assign more weight to kinematic data, by introducing weight factors f, as mentioned in §4.3.6. Specifically, to 'even' the data, we introduce weights inversely proportional to the size of subsample, $f \propto N^{-1}$. The results for this case are also given in Table 4.1 (# 10) and are in good agreement with all other estimations. This suggests that both photometric and kinematic data reflect the same true underlying distribution.

In summary, results from single-disk models are in good agreement with values found in the literature. Our analysis tends to favor lower values of disk inclination ($i \sim 27°$) of the reported range, $i = 25° - 45°$ (Westerlund 1997). The disk radial scale length, $H = 1.31$ kpc is in agreement with the value established from preliminary analysis.

4.4.2 Analysis of Residuals from Single Disk Solution

In the previous paragraph, we showed that fitting photometric and kinematic LMC data with a single disk solution results in disk parameters consistent with what can be found in the literature. However, because of a very rich and accurate photometric data, we can look for second-order effects, i.e. can analyze the residuals from single-disk LMC model.

Figure 4.4 shows the photometric residuals, $K_i - \overline{K}$, and kinematic residuals, $v_i - \overline{v}$, for the solution based on photometry and kinematics combined. For comparison, we also present the histogram of 1719 sources from Region J selected in Chapter 3. As expected, the two distributions have similar shapes, in particular the excess at $\Delta m \sim 0.5$ mag. The distribution of photometric residuals has the mean $\mu = 0.05$ and the root variance $\sigma = 0.36$. Testing the hypothesis $H_0 : \mu = 0$ versus $H_a : \mu \neq 0$, we obtain z-test statistic $Z = 13.08$, which means our single-disk model has problems of explaining the observed distribution. The figure also shows the distribution of residuals from Graff et al. (2000), based on radial velocity measurements of carbon stars in the inner $\sim$ 70 sq. deg. of the LMC. The two distributions are markedly different which can be attributed to differences in sky coverage.

The results of Gaussian analysis of the two distributions in Figure 4.4 are shown in Table 4.2. This analysis treats photometric and kinematic residuals independently and the results suggest with high degree of confidence that there are multiple components on the distribution. From Table 4.2, we do not find the kinematically distinct population (KDP) claimed by Graff et al. (2000). However, our data does not disprove

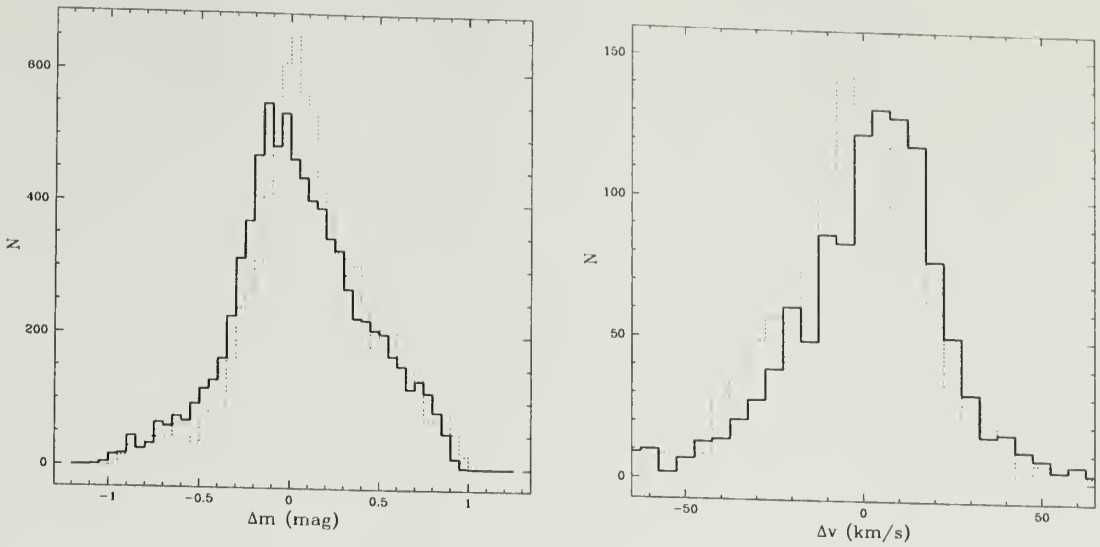

Figure 4.4 Photometric and kinematic residuals for single disk model. *Left panel:* Photometric residuals for single disk model. Solid line shows the histogram of the distribution of residuals, $K_i - \overline{K}$, for single disk model; dashed line is the distribution of 1719 sources analyzed in Chapter 3. The area under both histograms is the same. *Right panel:* Kinematic residuals for single disk model. Solid line and dashed line show the distributions of residuals from our model and from inner LMC data (Graff et al. 2000), respectively. Both histograms are normalized to the same area.

that this population does not exist, since we are looking primarily at the periphery of the LMC, while the evidence for KDP comes from central regions. By analogy with the terminology of Graff et al., we will introduce the term 'PDP' for photometrically distinct population. By PDP we will denote the secondary 'bump' in the photometric distribution, at $\sigma_m \sim 0.5 - 0.6$ mag.

The strongest evidence for support of multiple distinct components in the LMC would be obtained if we could show a definite correlation between different components seen in both distributions. Indeed, if one finds evidence that our relatively fainter stars from photometric distribution in Figure 4.4 have different systemic velocity relative to the main disk of the LMC, this would be very hard to reconcile by any scenario other than geometric structure. One way to look for this evidence is to examine the residuals plane (σ_m, σ_v). There are ~ 260 stars with both photometric and kinematic data in our sample. The distribution of these stars in the (σ_m, σ_v)-

Table 4.2 Gaussian analysis of LMC single-disk residuals.

Components	a_n	$\overline{x}_n$	σ_n	$\Delta\chi^2$
		Photometric residuals		
1	1.00	0.05 ± 0.01	0.36 ± 0.01	...
2	0.87	0.08 ± 0.01	0.38 ± 0.01	178.3
	0.13	-0.10 ± 0.01	0.11 ± 0.01	
3	0.15	0.60 ± 0.02	0.16 ± 0.01	379.5
	0.81	-0.01 ± 0.01	0.26 ± 0.01	
	0.04	-0.73 ± 0.02	0.14 ± 0.01	
		Kinematic residuals		
1	1.00	1.0 ± 0.6	24.5 ± 0.6	...
2	0.36	-5.7 ± 2.0	35.5 ± 2.0	160.4
	0.64	4.7 ± 1.0	14.2 ± 1.1	
3	0.30	10.8 ± 2.5	8.45 ± 2.2	173.5
	0.27	0.19 ± 2.7	16.59 ± 2.6	
	0.43	-4.5 ± 7.3	37.7 ± 3.1	

plane is shown in Figure 4.5, with contour levels representing a smoothed density distribution for these points. There is only a marginal evidence for correlation.

To quantify the strength of the correlation, we repeat the Gaussian analysis on the two-dimensional distribution in Figure 4.5. The two-dimensional distribution is parametrized by bivariate normal distribution with zero covariance,

$$P(\sigma_m, \sigma_v) = \sum_{n=1}^{N} \frac{a_n}{2\pi s_{m,n} s_{v,n}} \exp\left[-\frac{1}{2}\left(\frac{x_{m,n} - \sigma_m}{s_{m,n}}\right)^2 - \frac{1}{2}\left(\frac{x_{v,n} - \sigma_v}{s_{v,n}}\right)^2\right].$$

The results are presented in Table 4.3. The results are similar to what have been found by Graff et al. (2000). Single-component fit is rejected in favor of double-component model with statistical significance of 99.95%, while the statistical significance of rejecting a two-component model in favor of three-component fit is 98.8%. The velocity dispersions for two central components, $s_{v,1} = 14.7$ km/s and $s_{v,2} = 26.3$ km/s are in reasonable agreement with 8 km/s and 22 km/s derived by Graff et al. Nevertheless, there is no convincing evidence for the presence of KDP in our data.

In an alternative approach, we bin the photometric residuals and plot the spatial location of stars within these bins (Figure 4.6). The four panels in the Figure show the overdensity regions for photometric residuals in four magnitude bins: (-1,-0.5),

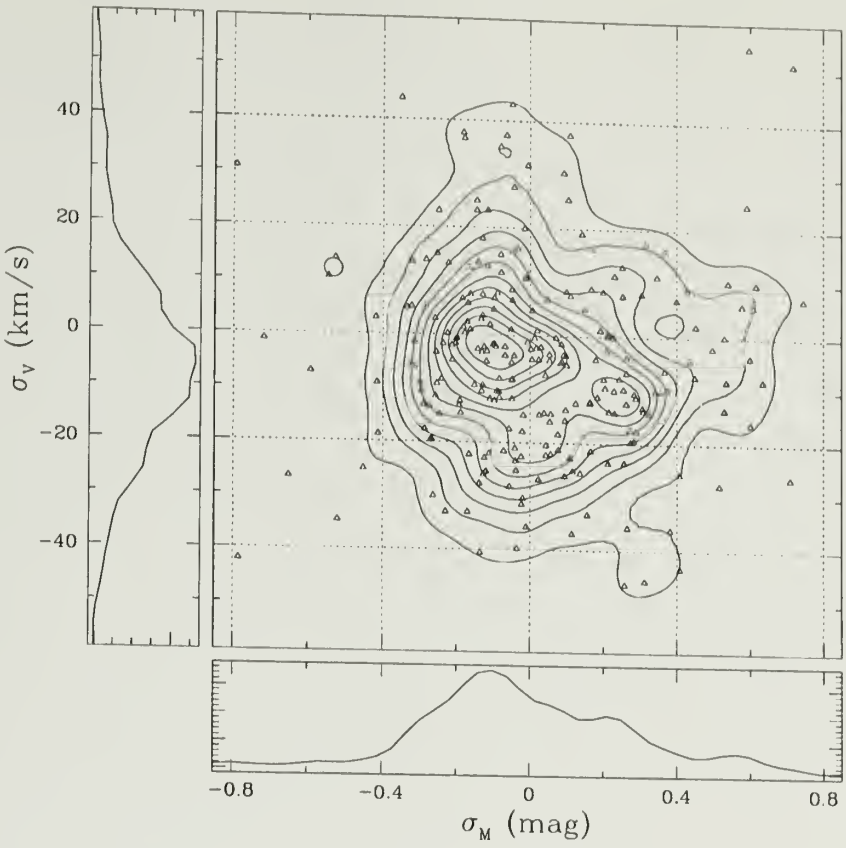

Figure 4.5 Residuals plane (σ_m, σ_v). Points represent sources with both photometric and kinematic data. contour levels show smoothed density distribution.

(-0.5, 0), (0, 0.5) and (0.5, 1). The overdensity is computed as the difference $\rho(\alpha, \delta) - \rho_0(\alpha, \delta)$, where ρ and ρ_0 are sky densities for sources in a particular bin and for the entire sample, respectively. As seen in Figure 4.6, the photometric residuals are concentrated in specific areas in the sky. The effect is particularly strong for highest and lowest bins. On average, brighter stars tend to occur in northwestern quadrant of the Cloud, while fainter sources mainly concentrated in the southeast region below 30 Dor. This can be interpreted as a structural component other than the main disk of the LMC.

In the absence of kinematic data for carbon star in the central regions of the LMC, we cannot directly verify whether the same pattern is observed in radial ve-

Table 4.3 Gaussian analysis of the residual plane.

Components	a_n	$x_{m,n}$	$s_{m,n}$	$x_{v,n}$	$s_{v,n}$	$\Delta\chi^2$
1	1.00	0.02 ± 0.03	0.28 ± 0.02	-1.1 ± 1.6	17.0 ± 1.1	...
2	0.67	0.08 ± 0.05	0.32 ± 0.03	-2.7 ± 2.6	17.4 ± 2.1	21.96
	0.33	-0.11 ± 0.04	0.11 ± 0.04	2.4 ± 4.7	15.6 ± 4.3	
2[a]	0.72	0.01 ± 0.03	0.22 ± 0.06	-1.2 ± 1.5	13.8 ± 2.8	14.62
	0.28	0.01	0.40 ± 0.12	-1.2	23.4 ± 7.7	
3	0.24	0.04 ± 0.12	0.41 ± 0.11	-1.0 ± 5.6	23.4 ± 8.5	36.52
	0.35	-0.13 ± 0.04	0.11 ± 0.03	2.1 ± 4.8	16.9 ± 3.7	
	0.41	0.12 ± 0.16	0.24 ± 0.14	-3.9 ± 4.1	10.9 ± 5.2	
3[a]	0.79	-0.02 ± 0.02	0.20 ± 0.03	-1.3 ± 1.6	14.7 ± 1.7	27.54
	0.16	-0.02	0.44 ± 0.13	-1.3	26.3 ± 7.4	
	0.05	0.56 ± 0.05	0.07 ± 0.04	3.5 ± 7.1	9.7 ± 6.3	

[a] Subject to constraints, $x_{m,1} = x_{m,2}$ and $x_{v,1} = x_{v,2}$.

locities. However, a comparison of our photometric residual maps with the map of low-velocity L-component seen in neutral hydrogen (Luks & Rohlfs 1992) reveals that *fainter sources from secondary peak at* $\sigma_m \sim 0.5$ *have the same distribution in the sky as the low-velocity L-component of neutral hydrogen maps.* This is a direct evidence that our 'photometrically distinct' sources have kinematic properties different from the conventional disk sources. Furthermore, our PDP is fainter than the main peak and hence is located behind the main LMC disk, which is also consistent with observed 21 cm absorption features from the main disk (Dickey et al. 1994). This evidence supports claims (e.g. Cowley & Hartwick 1991, Graff et al. 2000) of low-velocity component seen in stellar tracers. Assuming this is true and our fainter sources do have systemic velocity different from that of the disk, we have to conclude that these sources are *not* in the disk. This is the only reasonable conclusion, for one needs a very ingenious model to explain both different photometric and kinematic properties by stellar evolution or any other scenario.

To summarize, we have analyzed the residuals from a single-disk model fit to photometric and kinematic data. The search for KDP in kinematic residuals did not reveal a distinct population found by Graff et al., most likely because of different

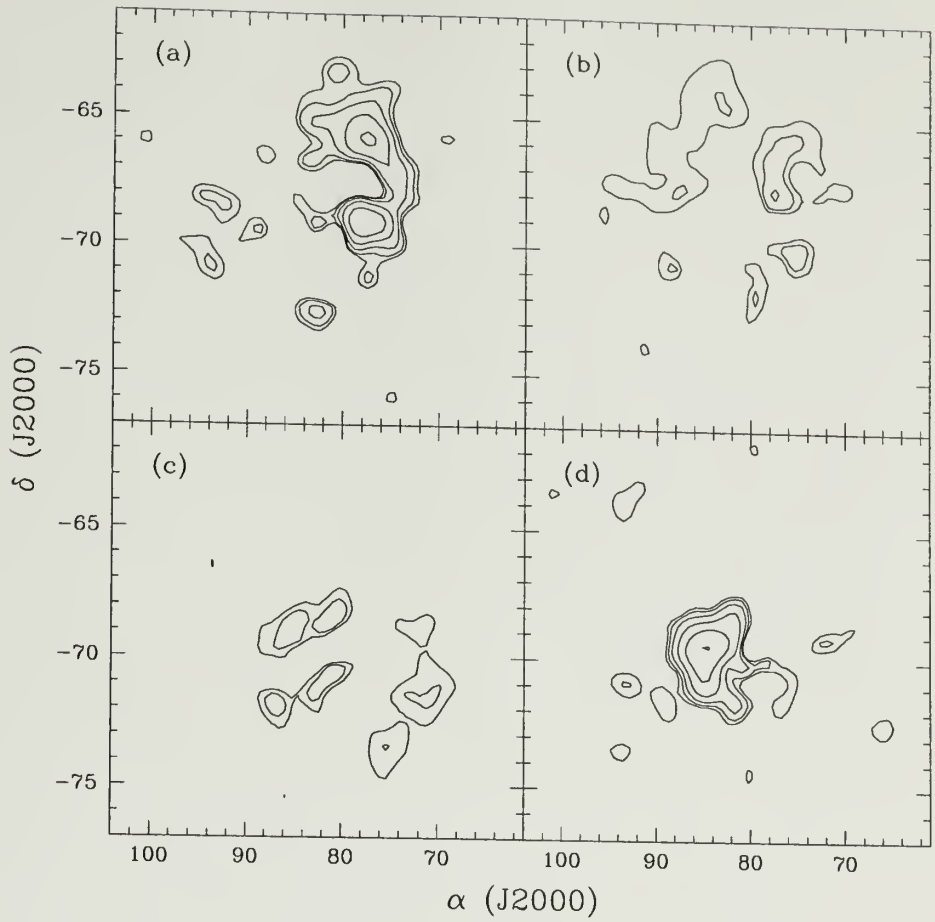

Figure 4.6 Sky distribution of sources in photometric bins: (a) [-1,-0.5], (b) [-0.5, 0], (c) [0, 0.5], and (d) [0.5, 1]. Contour levels indicate positive overdensity.

sky coverage of the two samples. However, we have associated the sources from the secondary photometric peak at $\sigma_m \sim 0.5$ with low-velocity component seen in neutral hydrogen maps. The two have nearly identical distribution in the sky which suggests that they have similar kinematics. We plan to test this possibility when kinematic data from inner LMC become available. Those additional $\sim$ 500 carbon stars are located in the central LMC and should provide a much better leverage for determining whether in fact the KDP is the same as PDP.

4.4.3 Two-Disk Model

The kinematics of the neutral hydrogen low-velocity component can be reasonably approximated by that of a second disk (Luks & Rohlfs 1992). Motivated by this fact, we can attempt to fit the photometry and kinematics of LMC by two-disk model. The distance to the second disk and the orientation parameters of its plane are free parameters.

Our results for two-disk model are summarized in Table 4.4. First, we run the ML analysis on photometric data only, with disk center either at the position of HI rotation center or a free parameter. In both cases, the distance to the second disk is assumed the same as the distance to the main disk, $R = 50$ kpc. Figure 4.7 shows the model fit for the solution with disk center fixed at HI rotation center. As expected, the main effect of the second plane is fitting the LMC bar, since the bar dominates the photometric distribution. We note that the scale lengths and the inclinations of the primary disk resulting from the two-disk model are greater than their respective values derived from single-disk fit, while the position angles remain similar. The scale length of the second disk is rather small, $H_s \lesssim 1.0$ kpc, and its derived inclination is made high to fit for the observed axis ratio of the bar, 3 : 1. Position angle of the second disk, $\theta = 107 - 114°$, is in agreement with the observed P.A. of the bar ($\sim 120°$).

Adding kinematic data to the sample has a profound effect on the disk orientation parameters. In most cases the second disk has position angle different by $30 - 35°$ from that of the main LMC disk. This shift is remarkably similar to what has been reported by Freeman et al. (1983) from the kinematics of globular clusters. In essence, they found that young clusters (SWB types I-III; Searle et al. 1980) rotated with H I gas, while the intermediate-age and old clusters (SWB V-VII) formed a separate rotating system with small velocity dispersion along the line of sight σ_z. The line of nodes of this second system was found to differ by some 50° relative to the young

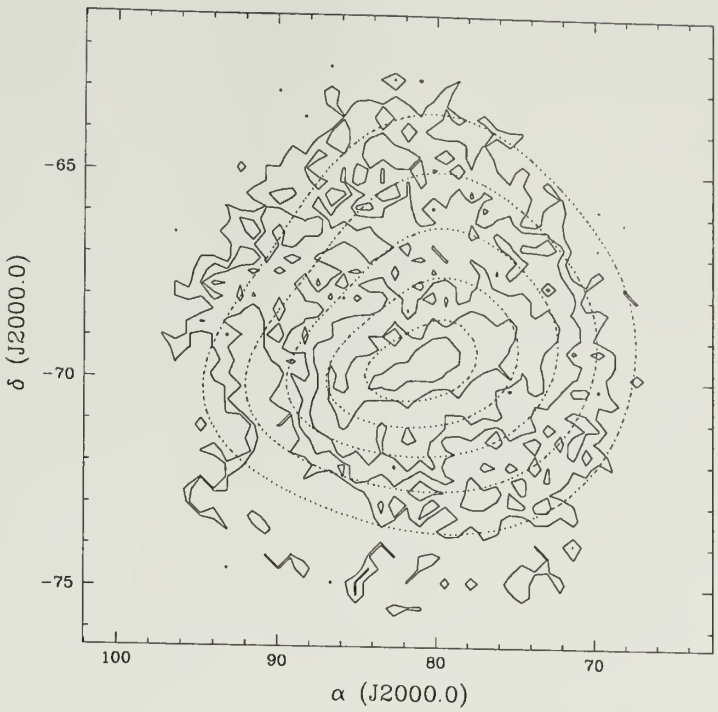

Figure 4.7 Two-disk LMC model based on photometric data only. The center of the main LMC disk is fixed at H I rotation center. Solid contours show the observed distribution, dotted lines represent the model.

disk, while the systemic velocity was lower by 18 km/s. This result has later been disputed based on a larger sample of LMC clusters (Schommer et al. 1992) which revealed some systematic effect in cluster velocities in Freeman et al. The fact that we find the same orientation for the second disk from kinematics of *stellar* tracers suggests that further study of this possibility is needed.

Figure 4.8 shows the best fit two-disk model with both photometric and kinematic data. Note the effect of adding a second disk on the velocity field: the contour levels are now visibly shifted toward greater position angles. The scale length of the main disk is now in better agreement with what was derived in single-disk model, while the inclinations are somewhat larger. The two-disk models consistently put the center of the second disk at the distance $R_2 \sim 53$ kpc, i.e. 3 kpc behind the main disk. This is due to PDP being fainter than the main disk. The magnitude of

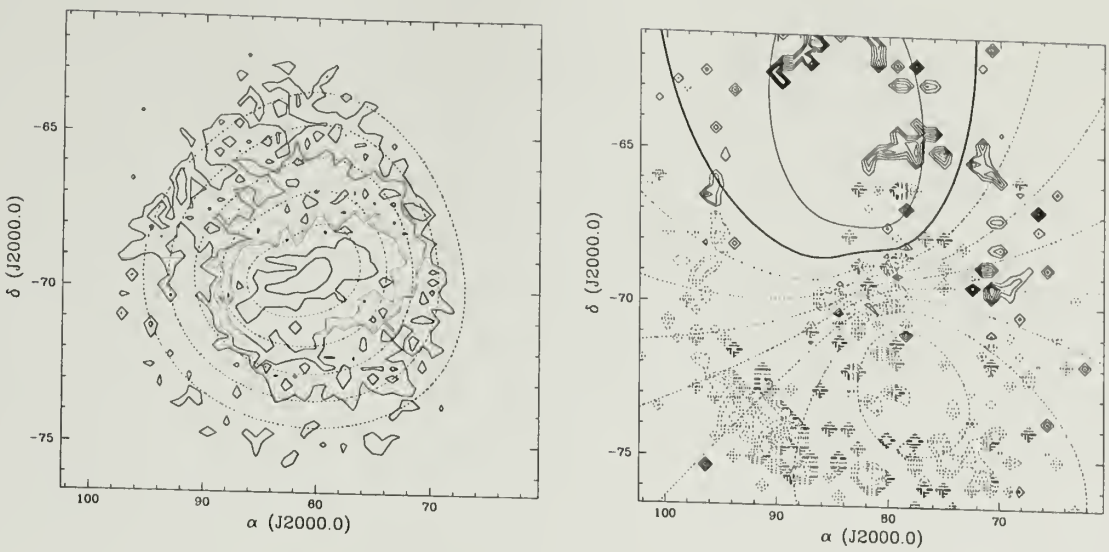

Figure 4.8 Model density and velocity field for two-disk LMC model. *Left panel*: Observed projected density for the LMC (solid contour levels) and best fit two-disk model (dotted lines). *Right panel*: Magellanocentric velocity field $v_{rad}(\alpha, \delta)$ for best-fit solution # 4 (see Table 4.4). Solid lines denote positive velocity, dotted lines – negative velocity. Contour levels are spaced by 10 km/s.

the displacement corresponds to the magnitude shift of approximately 0.13 mag (for the LMC distance of 50 kpc), which is in agreement with two-disk interpretation of photometric residuals in Chapter 3 (see Table 3.2). The second disk in our two-disk models has lower systemic velocity, although the magnitude of the velocity difference ($\sim$ 50 km/s) is likely to carry a large systematic error due to poor coverage of the central regions in our kinematic sample.

To summarize, the results from two-disk model suggest a presence of second disk plane at $\sim$ 3 kpc behind the main LMC disk. The line of nodes for the second disk is in agreement with value for intermediate-age and old LMC clusters (Freeman et al. 1983) and the systemic velocity of the second component is $\sim$ 50 km/s smaller. The results, however, are still inconclusive, mainly because of a poor coverage of central regions of the LMC by our kinematic data, and relatively few matches between kinematic and photometric samples.

4.5 Discussion

In our two-disk scenario, the material responsible for PDP and KDP is located behind the main disk. Due to its lower systemic velocity, the material will collide with the main body of the LMC. Assuming the velocity difference of 30 km/s, the collision will occur in approximately 3.0 kpc/30 km/s $\sim 10^8$ years. Contrary to the claim by Freeman et al., we cannot reliably establish the age of the second disk. To derive the relation between age of a carbon star and its NIR color, we have identified carbon stars in clusters with known ages and plotted the positions of the carbon star in the CMD for each age group. The results (not shown) are inconclusive and do not allow an interpretation of second disk as made of intermediate-age and old stars.

In principle, the effect of the second disk could be explained by twist in the main LMC disk, as both will produce the same characteristic twisting of the line of nodes at different radii. In fact, the evidence for the twisted main LMC disk has been found e.g., by Kim et al. (1998), and most recently, by Alves & Nelson (2000). However, the twisted disk is unlikely to produce a peculiar distribution of photometric residuals which has a relatively strong PDP component, because it is still quite thin. So even though the LMC disk may be twisted, the other possibility appears more likely. On the other hand, a strong asymmetric warp in the main disk could produce the observed photometric distribution, but has problems explaining the kinematic signature of the second disk. Indeed, from our results in Table 4.4 it follows that in projection to the sky plane, the two disks are *counterrotating*. A flared LMC disk (Alves & Nelson 2000) is another possible explanation for the observed distributions. Note, however, that in case of the flared disk one would tend to observe the closer parts relative to the disk midplane, and thus the distribution of photometric residuals would appear skewed to brighter stars, not fainter sources. Besides, ignoring the low-velocity component in the rotation solution can lead to a systematic error in the kinematic residuals which can be mistakenly interpreted as a flare in the LMC disk.

The two-disk scenario will enhance the microlensing optical depth because of the separation between sources and lenses. A single virialized disk can only account for the optical depth $\tau \lesssim 10^{-8}$ (Gould 1995), while the observed value from MACHO survey is $\tau = 1.2^{+0.4}_{-0.3} \times 10^{-7}$ (Alcock et al. 2000b). For two infinitely thin disks, one calculates the average optical depth due to microlensing,

$$\tau = \frac{4\pi G}{c^2} \frac{1}{26} \sum_{i=1}^{26} D_i \frac{\Sigma_{1i}\Sigma_{2i}}{\Sigma_{1i} + \Sigma_{2i}},$$

where D_i is the separation between disks, Σ_{ji} is the surface mass density at the center of ith MACHO field and the summation runs over 26 MACHO fields. For a crude estimate of the microlensing optical depth,

$$\tau \sim 6 \times 10^{-10} \left(\frac{D}{1\mathrm{kpc}}\right) \frac{\Sigma_1\Sigma_2}{\Sigma_1 + \Sigma_2}.$$

Assuming the separation $D \sim 5$ kpc we can estimate the surface density of the second disk given the surface density of the main disk and the observed value of τ. The observed surface brightness of the LMC is $R \sim 21$ mag arcsec^{-2} (de Vaucouleurs 1957) near the center. Assuming mass-to-light ratio of 3, this corresponds to surface mass density of the main disk of $300\,M_\odot$ pc^2. The observed optical depth τ is obtained for the second disk with surface density of only $\Sigma_2 = 45.8\,M_\odot$ pc^2. Therefore, only 15% extra surface density can explain the observed result from MACHO experiment, which is certainly within the error on the surface density estimate for the main disk.

4.6 Summary

We have presented a ML algorithm for analyzing spatial, photometric and kinematic distribution of LMC carbon stars. The method is quite general and can be applied to any standard candles obeying a luminosity-color relation (e.g., Cepheids). In this application, we presented the results for carbon-rich LPVs. The method is based on fitting astrometric, kinematic and photometric data for carbon stars with a

theoretical model, including mass distribution and rotation model. The spatial density of the LMC is modeled with one or two thin disks, as a way of searching for the material out of the plane of the main disk. The method allows using kinematic data from a variety of tracers, not necessarily carbon LPVs. In case if the photometric and kinematic samples do not overlap, the procedure results in simple averaging, weighted by the sample size. The kinematic data for this analysis are taken from a variety of sources, mostly from kinematic sample of Kunkel et al. for the periphery of the LMC.

We find that single disk models produce results consistent with previous estimations of disk parameters found in the literature. We find inclinations in range $i \approx 26°$ and position angles of the disk line of nodes at $\theta \sim 140° - 170°$. The scale length of the exponential disk is also derived, but our estimate could be biased due to presence of the SE loop, seen in the sky distribution of carbon stars.

Adding a second disk to the model primarily attempts to fit the bar of the LMC. While it has been suggested that the LMC bar is another exponential disk seen in projection (Zhao & Evans 2000), we do not find conclusive evidence to support this claim, mainly because of lack of data in central LMC regions. Additional kinematics sample of 551 LMC carbon stars from inner ~ 70 sq. deg. (Hardy et al. 2000) would prove useful in discriminating between the models, but unfortunately they were not available at the time. We will incorporate them in the analysis in future.

As possible modifications of the method, we mention adding other photometric bands and a weighting scheme to account for relative importance of data from various sources. Additional photometric bands will provide a leverage for determining the extinction, because of the additional color-color relations. This could improve the inferential power of the algorithm through additional constraints on the distribution of matter along the line of sight.

Table 4.4 Parameters of two-disk LMC models.

Number	α_0	δ_0	i	θ_0	H	V_0	Υ_m	S_m	R_2^a
					Photometry only				
1	(79.4)	(-69.03)	41 ± 6	187 ± 4	1.75 ± 0.11				
	81.7	-69.8	51 ± 8	107 ± 5	1.00 ± 0.09				(50.0)
2	(80.8)	(-69.5)	28 ± 3	172 ± 4	1.47 ± 0.04				
	80.6	-69.7	73 ± 2	114 ± 2	0.87 ± 0.05				(50.0)
					Photometry and Kinematics				
3	(79.4)	(-69.03)	(33)	(170)	(1.6)	6.5 ± 0.5	25.0 ± 0.4	(0.28)	
	81.0	-69.8	38 ± 2	108 ± 2	0.94 ± 0.03	(-23.5)	42.3 ± 1.9	(0.49)	53.1 ± 0.3
4[b]	78.9	-69.1	37 ± 2	182 ± 2	1.28 ± 0.03	12.0 ± 1.1	18.3 ± 1.3	(0.35)	
	83.8	-69.9	-28 ± 3	218 ± 3	1.13 ± 0.03	-36.8 ± 1.3	17.5 ± 1.2	(0.40)	52.5 ± 0.3
5	79.4	-69.2	31 ± 2	173 ± 1	1.24 ± 0.03	11.9 ± 0.7	25.7 ± 1.8	(0.37)	
	84.2	-70.0	-40 ± 2	213 ± 2	1.21 ± 0.04	-41.3 ± 1.4	18.6 ± 1.3	(0.38)	52.8 ± 0.4

[a]The distance to the second disk.
[b]Based on kinematic data from Kunkel et al. (1997) and Hughes et al. (1991).

APPENDIX A

PARAMETRIC MAXIMUM LIKELIHOOD FOR PROJECTED DENSITY DISTRIBUTION

The expected source density for a bin in the direction $(\alpha_i,\ \delta_j)$ is determined by integrating the LMC density model along the line of sight across the bin. This is given by the following integral:

$$\begin{aligned} \rho_{ij}^{exp} &\propto \int_0^\infty dt\, t^2 \int_{\delta_j-\Delta\delta/2}^{\delta_j+\Delta\delta/2} d\delta \cos\delta \int_{\alpha_i-\Delta\alpha/2}^{\alpha_i+\Delta\alpha/2} d\alpha\, \rho(t,\alpha,\delta) \\ &\approx \int_0^\infty dt\, t^2 \rho(t,\alpha_i,\delta_j) \cos\delta_j\, \Delta\alpha\, \Delta\delta, \end{aligned} \tag{A.1}$$

where the last equality assumes that the bin size $\Delta\alpha$, $\Delta\delta$ is sufficiently small. We perform the integral in (A.1) using 256-point Gaussian quadrature formula, with 20 kpc and 80 kpc as the integration limits. The underlying source density $\rho(t,\alpha,\delta)$ is given either by equation (3.1) or by equation (3.2). The coordinate transformations for both models follow.

A.1 Exponential Disk

To quantify $\rho(\cdot)$, we introduce the coordinate system $\{x_0, y_0, z_0\}$ which has the origin at the center of the LMC at $\{t,\alpha,\delta\} = \{R_{LMC}, \alpha_0, \delta_0\}$ and has z_0-axis toward the observer, x_0-axis antiparallel to the right ascension axis, and y_0-axis parallel to the declination axis. The coordinate transformations are given by

$$\begin{aligned} x_0 &= -t\cos\delta\sin(\alpha-\alpha_0) \\ y_0 &= t\sin\delta\cos\delta_0 - t\cos\delta\sin\delta_0\cos(\alpha-\alpha_0) \end{aligned} \tag{A.2}$$

$$z_0 = R_{LMC} - t\cos\delta\cos\delta_0\cos(\alpha-\alpha_0) - t\sin\delta\sin\delta_0.$$

The coordinate system of the exponential disk, $\{x', y', z'\}$, is the same rectangular system as $\{x_0, y_0, z_0\}$, except rotated about z_0-axis by the position angle θ counter-clockwise and about the new x'-axis by inclination angle i clockwise. The coordinate transformations are given by

$$\begin{aligned} x' &= x_0\cos\theta + y_0\sin\theta \\ y' &= -x_0\sin\theta\cos i + y_0\cos\theta\cos i - z_0\sin i \\ z' &= -x_0\sin\theta\sin i + y_0\cos\theta\sin i + z_0\cos i. \end{aligned} \tag{A.3}$$

Because our resolution in photometric distance is larger than the disk thickness, the integral in equation (A.1) may be simplified by assuming that the exponential disk is infinitely thin, i.e. $z' = 0$ for all points of the disk. The contribution to the integral is zero everywhere, then, except the point where line of sight intercepts the plane of the disk. The value of t at the intercept, $\bar{t}$, is

$$\begin{aligned} \bar{t} = & -R_{LMC}\cos i \times [\cos\delta\sin(\alpha-\alpha_0)\sin\theta\sin i \\ & + (\sin\delta\cos\delta_0 - \cos\delta\sin\delta_0\cos(\alpha-\alpha_0))\cos\theta\sin i \qquad \text{(A.4)} \\ & - (\cos\delta\cos\delta_0\cos(\alpha-\alpha_0) + \sin\delta\sin\delta_0)\cos i]^{-1}. \qquad \text{(A.5)} \end{aligned}$$

The values of x_0, y_0 and z_0 coordinates at the intercept point follow from equation (A.2). The radius and the position angle of the intercept point in the plane of the exponential disk are given by

$$r = \sqrt{x'^2 + y'^2}, \qquad \theta = \tan^{-1}(y'/x'), \tag{A.6}$$

where x' and y' are calculated from equation (A.3). Finally, the expected source density (A.1) may be written as

$$\rho_{ij}^{exp} \propto \bar{t}^2\exp(-r/R)\cos\delta_j, \tag{A.7}$$

where $\bar{t}$ and r are given by equations (A.4) and (A.6), respectively.

A.2 Power Law Model

Treatment of the spherical power law model is much simpler. Unlike the disk, there is no unique axis of symmetry and one may write the density (3.2) in the coordinates t, α and δ directly. It is straightforward to verify that

$$r = \sqrt{t^2 + R_{LMC}^2 - 2R_{LMC}t\left[\cos\delta\cos\delta_0\cos(\alpha - \alpha_0) + \sin\delta\sin\delta_0\right]}. \tag{A.8}$$

APPENDIX B

RADIAL VELOCITY

We adopt the rotation curve representation from Hughes & Wood (1990):

$$V(R) = V_0 + \frac{(a+1)\,\Upsilon_m\,R}{(S_m\,R)^{a+1} + a}\,, \tag{B.1}$$

where $\Upsilon_m = V_m/R_m$ and $S_m = 1/R_m$. Here, V_m is the maximum projected velocity, and R_m is the radius at which this velocity is attained. There are four free parameters in the rotation model: V_0, a, Υ_m and S_m. Parameter a describes the shape of the rotation curve and varies between 0 (flat rotation curve) and 1 (solid body rotation).

In the coordinate system $\{x', y', z'\}$, radial velocity is written as

$$\begin{pmatrix} v_{x'} \\ v_{y'} \\ v_{z'} \end{pmatrix} = V(R) \begin{pmatrix} -\sin\theta \\ \cos\theta \\ 0 \end{pmatrix}, \tag{B.2}$$

where $V(R)$ is given by equation (B.1) and R and θ are given by equation (A.6). Converting the coordinates to the system $\{x_0, y_0, z_0\}$, we obtain:

$$\begin{pmatrix} v_{x_0} \\ v_{y_0} \\ v_{z_0} \end{pmatrix} = V(R) \begin{pmatrix} -\cos\theta_0 \sin\theta - \sin\theta_0 \cos\theta \cos i \\ -\sin\theta_0 \sin\theta + \cos\theta_0 \cos\theta \cos i \\ -\cos\theta \sin i \end{pmatrix}. \tag{B.3}$$

The radial velocity is given by the dot product

$$v_r = v_{x_0} e_{x0} + v_{y_0} e_{y0} + v_{z_0} e_{z0}, \tag{B.4}$$

where components of velocity are given by (B.3) and position unit vector is

$$\begin{aligned} e_{x0} &= -\cos\delta \sin(\alpha - \alpha_0) \\ e_{y0} &= \sin\delta \cos\delta_0 - \cos\delta \sin\delta_0 \cos(\alpha - \alpha_0) \end{aligned} \tag{B.5}$$

$$e_{z0} = -\sin\delta\sin\delta_0 - \cos\delta\cos\delta_0\cos(\alpha - \alpha_0).$$

B.1 Correction for Space Motions of the Sun and the LMC

To derive radial velocity corrections due to Solar motion and LMC bulk motion, we adopt the Galactocentric coordinate system used by Gardiner et al. (1994). In this coordinate system, the velocity vector of the LMC is (Kroupa & Bastian 1997):

$$\mathbf{V}_t = (+41 \pm 44, -200 \pm 31, +169 \pm 37) \text{ km/s}.$$

Given the observed heliocentric radial velocity V_h, the corrected magellanocentric velocity V_{LMC} is given by

$$V_{LMC} = V_h + (\mathbf{V}_\odot - \mathbf{V}_t) \cdot \mathbf{X}(l, b),$$

where $\mathbf{X}(l, b) = (\cos b \cos l, \cos b \sin l, \sin b)$ is the position vector for a star at coordinates (l, b). The circular velocity of the Sun is taken $\mathbf{V}_\odot = (0, 220, 0)$ km/s.

BIBLIOGRAPHY

Albrow, M. D., et al. 1999, ApJ, **512**, 672

Alcock, C., et al. 1999, astro-ph/9807163

Alcock, C. et al. 2000, AJ, **119**, 2194

Alcock, C., et al. 2000, astro-ph/0001272

Allen, C. W. 1976, *Astrophysical Quantities* (London: Athlone)

Alves, D. et al. 1998, astro-ph/9804003

Alves, D., Alcock, C., Cook, K., Marshall, S., Minniti, D., Allsman, R., Axelrod, T., Freeman, K., Peterson, B., Rodgers, A., Griest, K., Vandehei, T., Becker, A., Stubbs, C., Tomaney, A., Bennett, D., Lehner, M., Quinn, P., Pratt, M., Sutherland, W., Welch, D. 1998, in *Pulsating Stars: Recent Developments in Theory and Observation*, Proceedings of IAU Joint Discussion 24, eds. M. Takeuti & D. Sasselov (Tokyo:Universal Academy Press)

Alves, D. R. & Nelson, C. A. 2000, astro-ph/0006018

Beaulieu, J.-P. & Sackett, P. D. 1998, AJ, **116**, 209

Bennett, D. P., et al. 1996, astro-ph/9606012

Bennett, D. P. 1998, ApJ, **493**, L79

Bertelli, G, Bressan, A. G., Chiosi, C. 1985, A&A, **150**, 33

Bertelli, G., Bressan, A., Chiosi, C., Fagotto, F., Nasi, E. 1994, AAS, **106**, 275

Bessell, M. S. 1979, PASP, **91**, 589

Bessell, M. S. 1991, ApJ, **101**, 662

Bessell, M. S. 1991, A&A, **242**, L17

Bessell, M. S. & Brett, J. M. 1988, PASP, **100**, 1134

Bica, E., Geisler, D., Dottori, H., Clariá, J. J., Piatti, A. E., Santos, J. F. C., Jr., 1998, AJ, **116**, 723

Bothun, G. D., & Thompson, I. B. 1988, AJ, **96**, 877

Breysacher, J., Azzopardi, M., Testor, G. 1999, AAS, **137**, 117

Caldwell, J. A. R. & Coulson, I. M. 1986, MNRAS, **218**, 223

Castellani, V., Chieffi, A., Pulone, L. 1991, ApJS, **76**, 911

Cole, A. A., Wood, K., Nordsieck, K. H. 1999, AJ, **118**, 2292

Cole, A. A. 1999, Ph.D. thesis, University of Wisconsin-Madison

Cole, A. A. 2000, private communications

Cowley, A. P. & Hartwick, F. D. A. 1982, ApJ, **259**, 89

Cowley, A. P. & Hartwick, F. D. A. 1991, ApJ, **373**, 80

Cutri, R. M, Skrutskie, M. F., Van Dyk, S., Chester, T., Evans, T., Fowler, J., Gizis, J., Howard, E., Huchra, J., Jarrett, T., Kopan, E. L., Kirkpatrick, J. D., Light, R. M, Marsh, K. A., McCallon, H., Schneider, S., Stiening, R., Sykes, M., Weinberg, M., Wheaton, W. A., Wheelock, S. 1999, `http://www.ipac.caltech.edu/2mass/releases/first/doc/explsup.html`

Dickey, J. M, Mebold, U., Marx, M., Amy, S., Haynes, R. F., Wilson, W. 1994, A&A, **289**, 357

Di Stefano, R. 1999, astro-ph/9901035

Elias, J. H., Frogel, J. A., Matthews, K, Neugebauer, G. 1982, AJ, **87**, 1029

Elias, J. H., Frogel, J. A., Humphreys, R. M. 1985, ApJS, **57**, 91

Epchtein, N., de Batz, B., Capoani, L., Chevallier, L., Copet, E., Fouqué, P., Lacombe, F., Le Bertre, T., Pau, S., Rouan, D., Ruphy, S., Simon, G., Tiphène, D., Burton, W. B., Bertin, E., Deul, E., Habing, H., Borsenberger, J., Dennefeld, M., Guglielmo, F., Loup, C., Mamon, G., Ng, Y., Omont, A., Provost, L., Renault, J.-C., Tanguy, F., Kimeswenger, S., Kienel, C., Garzón, F., Persi, P., Ferrari-Toniolo, M., Robin, A., Paturel, G., Vauglin, I., Forveille, T., Delfosse, X., Hron, J., Schultheis, M., Appenzeller, I., Wagner, S., Balazs, L., Holl, A., Lepine, J., Boscolo, P., Picazzio, E., Duc, P.-A., Mennessier, M.-O. 1997, The Messenger, **87**, 27

Feast, M. W., Glass, I. S., Whitelock, P. A., Catchpole, R. M. 1989, MNRAS, **241**, 375

Feitzinger, J. V., Isserstedt, J., Schmidt-Kaler, Th. 1977, A&A, **57**, 265

Fields, B. D., Freese, K., and Graff, D. S. 1998, NewA, **3**, 347

Freeman, K. C., 1970, ApJ, 160, 811

Freeman, K. C., Illingworth, G., Oemler, A. 1983, ApJ, **272**, 488

Frogel, J. A. & Blanco, V. M. 1990, ApJ, **365**, 168

Frogel, J., Mould, J., Blanco, V. M. 1990, ApJ, **352**, 96

Gallart, C. 1998, ApJ, **495**, L43

Gardiner, L. T., Sawa, T., and Fujimoto, M. 1994, MNRAS, **266**, 567

Gardiner, L. T., Turfus, C., and Putman, M. E. 1998, ApJL, **507**, L35

Gascoigne, S. C. B., & Shobbrook, R. R. 1978, PASAu, **3**, 285

Girardi, L., Bressan, A., Bertelli, G., Chiosi, C. 2000, AAS, **141**, 371

Glass, I. S., Whitelock, P. A., Catchpole, R. M., Feast, M. W., Laney, C. D., 1990. S. Afr. Astron. Obs. Circ., **14**, 63

Gould, A. 1995, ApJ, **441**, 77

Gould, A. 1998, ApJ, **499**, 728

Graff, D. S., Gould, A. P., Suntzeff, N. B., Schommer, R. A., Hardy, E. 2000, ApJ, **540**, 211

Grebel, E. K. & Brandner, W. 1998, in *The Magellanic Clouds and Other Dwarf Galaxies*, Proceedings of the Bonn/Bochum-Graduiertenkolleg Workshop, Germany, January 19-22, eds. T. Richtler and J. M. Braun, p.151

Greve, A., van Genderen, A. M., Laval, A. 1990, AAS, **85**, 895

Grillmair, C. J., Freeman, K. C. Irwin, M. & Quinn, P. J., 1995, AJ, **109**, 2553

Gummersbach, C. A., Zickgraf, F.-J., Wolf, B. 1995, A&A, **302**, 409

Gyuk, G., Dalal, N., and Griest, K. 2000, ApJ, **535**, 90

Hardy, E., Buonanno, R., Corsi, C. E., Janes, K. A., Schommer, R. A. 1984, ApJ, **278**, 592

Hardy, E., Schommer, B., and Suntzeff, N. 2000, in preparation

Harris, H. C. 1983, AJ, **88**, 507

Harris, J., Zaritsky, D., Thompson, I. 1997, AJ, **114**, 1933

Hughes, S. M. G. 1989, AJ, **97**, 1634

Hughes, S. M. G. & Wood, P. R. 1990, AJ, **99**, 784

Hughes, S. M. G., Wood, P. R., Reid, N. 1991, AJ, **101**, 1304

Iben, I., Jr. & Renzini, A. 1983, ARA&A, **21**, 271

Iglesias, C. A., Rogers, F. J., Wilson, B. G. 1992, ApJ, **397**, 717

Irwin, M. J. 1991, in Proc. IAU Symp. 148, The Magellanic Clouds; eds. R. Haynes, D. Milne (Kluwer, Dordrecht), 453

Jarrett, T. H., Chester, T., Cutri, R., Schneider, S., Skrutskie, M., Huchra, J. P. 2000, AJ, **119**, 2498

Johnston, K. V., Sigurdsson, S. and Hernquist, L. 1999, MNRAS, **302**, 771

Jones, T. J., Hyland, A. R., Straw, S., Harvey, P. M., Wilking, B. A., Joy, M., Gatley, I., Thomas, J. A. 1986, MNRAS, **219**, 603

Kerins, E. J. & Evans, N. W. 1999, ApJ, **517**, 734

Kerschbaum, F., & Hron, J. 1994, AAS, **106**, 397

Kim, S., et al. 1998, ApJ, **503**, 674

Koornneef, J. 1982, A&A, **107**, 247

Kroupa, P. & Bastian, U. 1997, New Astr., **2**, 77

Kuchinski, L. E., Frogel, J. A., Terndrup, D. M., Persson, S. E. 1995, AJ, **109**, 1131

Kunkel, W. E., Irwin, M. J., and Demers, S. 1997, AAS, **122**, 463

Kunkel, W. E., Demers, S., Irwin, M. J., Albert, L. 1997, ApJL, **488**, L129

Laney, C.D. & Stobie, R. S. 1986, MNRAS, **222**, 449

Lee, T. A. 1970, ApJ, **162**, 217

Luks, Th. & Rohlfs, K. 1992, A&A, **263**, 41

Madore, B. F & Freedman, W. L. 1991, PASP, **103**, 933

Maeder, A. & Meynet, G. 1989, A&A, **210**, 155

Marigo, P., Bressan, A., Chiosi, C. 1996, A&A, **313**, 545

Martin, N., Prévot, L., Rebeirot, E., Rousseau, J. 1976, A&A, **51**, 31

Mateo, M. & Hodge, P. 1987, ApJ, **320**, 626

McGee, R. X. & Milton, J. A. 1966, Aust. J. Phys., **19**, 343

Meatheringham, S. J., Dopita, M. A., Ford, H. C., and Webster, B. L. 1988, ApJ, **327**, 651

Mould, J. R., Huchra, J. P., Freedman, W. L., Kennicutt, R. C., Jr, Ferrarese, L., Ford, H. C., Gibson, B. K., Graham, J. A., Hughes, S., Illingworth, G. D., Kelson, D. D., Macri, L. M, Madore, B. F., Sakai, S., Sebo, K., Silbermann, N. A., Stetson, P. B. 1999, astro-ph/9909260

Oestreicher, M. O. & Schmidt-Kaler, Th. 1996, A&AS, **117**, 303

Olszewski, E. W., Schommer, R. A., Suntzeff, N. B., Harris, H. C. 1991, AJ, **101**, 515

Persson, S. E., Murphy, D. C., Krzeminski, W., Roth, M., Rieke, M. J. 1998, AJ, **116**, 2475

Prévot, L. et al. 1985, AAS, **62**, 23

Reid, N., Glass, I. S., and Catchpole, R. M. 1988, MNRAS, **232**, 53

Reid, N. 1991, ApJ, **382**, 143

Renzini, A. & Fusi-Pecci, F. 1988, ARA&A, **26**, 199

Rieke, G. H. & Lebofsky, M. J. 1985, ApJ, **288**, 618

Rohlfs, K., Kreitschmann, J., Feitzinger, J. V., and Siegman, B. C. 1984, A&A, **137**, 343

Sakai, S., Zaritski, D., Kennicutt, R., 1999, astro-ph/9911528

Schmidt-Kaler, Th. 1977, A&A, **54**, 771

Schmidt-Kaler, Th. & Gochermann, J. 1992, in *Variable Stars and Galaxies*, ASP Conference Series, Vol. 30, edited by B. Warner, p. 203

Schommer, R. A., Olszewski, E. W., Suntzeff, N. B., Harris, H. C. 1992, AJ, **103**, 447

Searle, L., Wilkinson, A., Bagnuolo, W. G. 1980, ApJ, **239**, 803

Skrutskie, M. F., Schneider, S. E., Stiening, R., Strom, S. E., Weinberg, M. D., Beichman, C., Chester, T., Cutri, R., Lonsdale, C., Elias, J., Elston, R., Capps, R., Carpenter, J., Huchra, J., Liebert, J., Monet, D., Price, S., Seitzer, P., in *The Impact of Large Scale Near-IR Sky Surveys*, p.187, F. Garzon et al. (eds.), Kluwer (Netherlands).

Tiede, G. P, Martini, P., Frogel, J. A. 1997, AJ, **114**, 694

de Vaucouleurs, G. 1955, AJ, **60**, 126

de Vaucouleurs, G. 1957, AJ, **62**, 69

de Vaucouleurs, G. 1980, PASP, **92**, 576

de Vaucouleurs, G. & Freeman, K. C. 1973, Vis. Astron., **14**, 163

van den Bergh, S. 1981, AAS, **46**, 79

van Dyk, S. D., Cutri, R., Skrutskie, M. F. 1999, BAAS, 195.0403

van Loon,J. Th., Zijlstra, A. A., Whitelock, P. A., Te Lintel Hekkert, P., Chapman, J. M., Loup, C., Groenewegen, M. A. T., Waters, L. B. F. M., Trams, N. R. 1998, A&A, **329**, 169.

Wainscoat, R. J., Cohen, M., Volk, K., Walker, H. J., Schwartz, D. E. 1992, ApJS, **83**, 111

Walker, A. R. 1990, AJ, **100**, 1532

Walker, A. R. 1992, AJ, **103**, 1166

Weinberg, M. D. 2000, ApJ, **532**, 922

Welch, D. L., McLaren, R. A., Madore, B. F., McAlary, C. W. 1987, ApJ, **321**, 162

Westerlund, B. E. 1964, in *The Galaxy and the Magellanic Clouds*, Proceedings of the IAU Symp. 20, edited by F. J. Kerr, Canberra: Australian Acad. Sci., p. 239

Westerlund, B. E. 1997, *The Magellanic Clouds*, Cambridge University Press

Wood, P. R. & Bessell, M. S. 1983, ApJ, **265**, 748

Wood, P. R., Whiteoak, J. B., Hughes, S. M. G., Bessell, M. S., Gardner, F. F., Hyland, A. R. 1992, ApJ, **397**, 552

Wood, P. R. 1994, Ap&SS, **217**, 121

Wood, P. R. & Sebo, K. M. 1996, MNRAS, **282**, 958

Wood, P. R. et al. 1998, IAU Symp. 191

Wood, P. R. 1999, private communications

Wood, P. R. 2000, PASA, **17**, 18

Zaritsky, D., Lin, D. N. C. 1997, AJ, **114**, 2545

Zaritsky, D. 1999, AJ, **118**, 2824

Zijlstra, A. A., Loup, C., Waters, L. B. F. M., Whitelock, P. A., van Loon, J. Th., Guglielmo, F. 1996, MNRAS, **279**, 32

Zhao, H.-S. & Evans, N. W. 2000, astro-ph/0009155